

Development of boron-doped diamond
heater in the Kawai-type multi-anvil
apparatus and its application to determine
silicate melt viscosity at conditions of deep
magma ocean

2018, August

Longjian Xie

谢龙剑

Graduate School of Natural Science and Technology

(Doctor's course)

OKAYAMA UNIVERSITY

Contents

Summary	1
Part 1. Boron-doped diamond heater in Kawai-type multi-anvil apparatus	2
1.1 Abstract	3
1.2 Introduction	3
1.3 Experimental procedure.....	6
1.4 Results and discussion.....	8
1.5 Conclusions and perspectives.....	14
References in Part I	16
Table.....	20
Figures.....	22
Part 2. Viscosity measurement of silicate melts up to ~30 GPa.....	38
2.1 Abstract	39
2.2 Introduction	40
2.3 Experimental procedure.....	44
2.4 Results and discussions	47
2.5 Conclusions	53
References in Part II.....	54
Tables	59
Figures.....	64
Part 3. Chemical evolution of magma ocean inferred from silicate melt viscosity	76
3.1 Abstract	77
3.2 Introduction	78
3.3 Method.....	85

3.4 Results and discussions	86
3.5 Conclusions	90
References in Part III.....	91
Tables	98
Figures	103
Appendix 1. Liquidus of related mantle materials	108
Acknowledgements	109

Summary

In this PhD thesis, I summarize my achievements in the recent three years after the interim evaluation September 2015. It consists of three parts: (1) boron-doped diamond (BDD) heater developed in the multi-anvil apparatus, (2) viscosity measurement of silicate melts up to ~30 GPa using *in-situ* falling sphere method, and (3) implications for the evolution of the magma ocean based on the silicate melt viscosity newly measured in the present study.

Breakthroughs both in experimental techniques and in geoscientific modelling for the early Earth are achieved in this study. Highlights of my study are (1) generation of ~4000 K temperature (world highest) in the Kawai multi-anvil apparatus by using BDD heater, (2) world first measurements of silicate melt viscosity under the lower mantle condition by applying BDD heater in the *in-situ* falling sphere viscometry; the viscosity data experimentally reproducing all the four pressure induced densification mechanisms predicted in molecular dynamic simulation, and (3) the estimated viscosity of magma ocean suggests a fractional solidification of magma ocean.

Combined with our fractional solidification model and geochemical data of primary upper mantle, we estimated the depth of fractionated magma ocean is ~880 km and the thickness of cumulate layer in the lower mantle is ~220 km. After fully solidification, the cumulate layer is bridgmanite-enriched, neutral (or slightly denser ~2 ‰) and stronger (viscosity contrast ~30), compared with pyrolite mantle. Because of its high viscosity, the solidified accumulate layer may be transferred to the depth of ~1000 km by later mantle convection and still persists there at present day. It may contribute to the viscosity peak at 800-1400 km of present solid Earth.

**Part 1. Boron-doped diamond heater in the
Kawai-type multi-anvil apparatus**

1.1 Abstract

Methods to use synthesized boron-doped diamond (BDD) as a heater were developed in a multi-anvil high-pressure apparatus. The synthesized BDD heater could stably generate an ultra-high temperature without the issues (anomalous melt, pressure drop and instability of heating) arising from oxidation of boron into boron oxide and graphite-diamond conversion. BDD blocks and tubes with boron contents of 0.5–3.0 wt.% from a mixture of graphite and amorphous boron, were synthesized at 15 GPa and 2000 °C. The electrical conductivity of BDD increased with increasing boron content. The stability of the heater and heating reproducibility were confirmed through repeated cycles of heating and cooling. Temperatures as high as ~3700 °C were successfully generated at higher than 10 GPa using the BDD heater. The effect of the BDD heater on the pressure-generation efficiency was evaluated using MgO pressure scale by *in situ* X-ray diffraction study at the SPring-8 synchrotron. The pressure-generation efficiency was lower than that using a graphite-boron composite heater up to 1500 tons. The achievement of stable temperature generation above 3000 °C enables melting experiments of silicates and determination of some physical properties (such as viscosity) of silicate melts under the Earth's lower mantle conditions.

1.2 Introduction

Generation of high-pressure (>20 GPa) and high-temperature (>2000 °C) are essential to improve our understanding of the Earth's interior¹ and create novel materials such as nano-polycrystalline diamond (NPD)². An appropriate sample volume is essential to measure some physical properties such as melt viscosity and to utilize or characterize the properties of resultant products³. Some physical or chemical properties

measurement such as diffusion, also requires a large volume (larger than several hundred micrometers) with a stable and homogeneous temperature field. Development or improvement of apparatus for stable, homogeneous high-pressure and high-temperature in a large volume is important.

There are only two kinds of high pressure apparatus can generate pressure over 20 GPa and temperature over 2000 °C, that is, laser heated diamond anvil cell (LH-DAC) ^{eg. 4-7} and multi-anvil apparatus (MAA) ^{eg.1,8} . However, LH-DAC can only generate high pressure at a small sample volume, with a steep T-gradient, large T-fluctuation and uncontrolled chemical environment. The MAA is the only apparatus, which can produce quasi-hydrostatic pressures over 20 GPa in a large volume ^{eg.1,8} with a stable and homogeneous temperature field. Technological advancement to extend the limits of pressure and temperature generation in MAA is thus, an important issue in high-pressure materials and earth science.

Recently, pressures over 100 GPa in MAA were succeeded to generate by employing sintered diamond anvils⁹. However, the temperature generation over 3000 °C in MAA is still difficult by using traditional heating material (such as TiB₂, rhenium, LaCrO₃). Since temperatures higher than 3000 °C are needed for melting experiments on mantle materials under lower-mantle conditions ^{eg. 4-7}, a refractory heating material is essential to melt materials in the deep Earth such as bridgmanite and ferropericlase.

Moreover, *in-situ* X-ray observation using synchrotron radiation has become a powerful tool for high pressure research. The combination of synchrotron radiation with MAA not only enables researcher to directly observe the sample under high pressure and high temperature but also measure the structure and properties of materials under high pressure and high temperature ^{1, 3} . The traditional heater material such Re and

LaCrO₃, are not X-ray transparent.

Thus, developing a heater material, which is both refractory to melt the lower mantle and X-ray transparent, are important for Earth science. Boron-doped diamond (BDD) is the best candidate to satisfy both requirements with its high melting point and low X-ray absorption properties^{3,10-12}. In previous works, BDD has been synthesized from a graphite–boron composite (GBC) *in situ* during heating to avoid directly manufacturing the hardest material, diamond. I also systematically studied this GBC heater, which has been documented in my intern evaluation thesis and published in high pressure research journal¹². From the previous researches and my research, several problems of GBC are documented. The graphite–diamond conversion is accompanied by a large volume reduction and drastic change of electrical resistivity leading to a significant pressure drop and unstable heating, respectively. Furthermore, the boron in the graphite–boron mixture is easily oxidized into boron oxide, B₂O₃, which acts as a fatal melting flux¹². Thus, the direct use of BDD is strongly preferable for stable ultra-high temperature generation.

There are two possible routes to overcome the difficulty of manufacturing BDD tube heaters: direct synthesis of a BDD tube or molding of a BDD tube from BDD powders. BDD is usually synthesized via chemical vapor deposition (CVD) or the HPHT method. The CVD method is usually applied to synthesize BDD films (<1 μm thickness) e.g.,¹³⁻¹⁵. In the HPHT method, however, BDD of millimeter size can be synthesized in the B–C e.g.,¹⁶⁻¹⁷ or B–H–C system¹⁸.

In this study, I successfully synthesized BDD tubes and blocks with various boron contents using the HPHT method. The BDD tubes were directly used as heaters, whereas the BDD blocks were ground into powders and then molded into tube heaters. The synthesized BDD heaters exhibited good performance for stable ultra-high

temperature generation. The X-ray transparency and pressure generation of a Kawai cell assembly using the BDD heater were also evaluated using *in situ* X-ray observation with synchrotron radiation at SPring-8.

1.3 Experimental procedure

1.3.1 Synthesis of BDD tubes and blocks

BDD tubes and blocks were synthesized at ~15 GPa and ~2000 °C for 10-30 minutes in Kawai-type multi-anvil apparatuses (USSA-1000 and USSA-5000) using cubic tungsten carbide (WC) blocks as second anvil with 8-mm truncation edge length. Figure 1.1 shows some examples of cell assembly. A Cr-doped MgO octahedron (OMCR, Mino Ceramic Co., LTD) with a 14-mm edge length was used as the pressure medium, and zirconia (OZ8C, Mino Ceramic Co., LTD) was used as a thermal insulator. Rhenium/LaCrO₃ was used as a heater. The starting material was a mixture of graphite and amorphous boron enclosed in a MgO capsule. The graphite had a purity of 99.999% with a grain size of < 1 μm. The amorphous boron with a grain size of 0.8–1.4 μm contained major impurities of H₃BO₃ < 0.75 wt.%, H₂O < 0.5 wt.%, and Mg < 1.0 wt.%. We prepared powder mixtures with various boron content (0.5, 1.0, 2.0, or 3.0 wt%). For synthesis of the BDD tube, an MgO rod was placed at the center of the mixture.

For the BDD synthesis runs, temperature was estimated from the power–temperature relationship for each assembly to avoid reaction and obtain a larger amount of BDD. The temperatures in the calibration runs were measured using a W₉₇Re₃–W₇₅Re₂₅ thermocouple without corrections for the pressure effect on *emf*. The thermocouple was insulated from the rhenium heater by an alumina tube, and the junction was shifted to 2 mm away from the center position of heater.

The load was increased to 663 tons, which is corresponded to ~15 GPa, in 6 h; then,

the temperature was increased to ~ 2000 °C and maintained for 10–30 min. Next, the load was reduced to 204 tons at 1000 °C in more than 5 h and continuously decompressed to 4 tons at 500 °C in more than 5 h to minimize the formation of cracks inside the BDD tubes or blocks. The recovered assembly was rinsed in 10 wt.% HCl solution for ~ 12 h to remove any MgO around the BDD blocks and tubes. Then, the BDD blocks and tubes were washed with pure water to remove residual HCl and dried at 80 °C in a vacuum oven. The recovered BDD blocks and tubes were checked by an optical microscope and a scanning electron microscope (JSM-7001F, JEOL Co. Jap.) to observe the microstructure. The phases were identified by a micro-focused X-ray diffractometer (RINT RAPID II, RIGAKU Co. Jap.) with 100 μm X-ray beam size.

1.3.2 Heating tests without and with synchrotron X-ray

We tested heating performance of the synthesized BDD heater. The BDD tubes were directly used as heaters, whereas the BDD blocks were first ground into powders using a nano-polycrystalline diamond mortar and then molded into tube shape to be used as heaters. The sintered tube BDD heaters with different boron contents (0.5, 1.0, 2.0, and 3.0 wt.%) and powder BDD heater with that of 3.0 wt.% were examined.

Table 1.1 summarizes runs at 10 or 15 GPa with or without synchrotron X-ray. Runs without synchrotron X-ray were conducted at Institute for Planetary Materials (IPM), Okayama Univ. to investigate the heating performance of BDD heaters with different boron content and to improve the cell design to generate ultrahigh temperature. Runs with synchrotron X-ray were conducted at beam line BL04B1 at SPring-8 to understand the pressure generation efficiency and X-ray transparency of cell assembly with a BDD heater. All the runs were used WC cubes as second anvils with 8-mm truncation edge length and a Cr-doped MgO octahedron as the pressure medium. The

length of the edge of the octahedral pressure medium was 14 mm. The temperature was monitored by $W_{97}Re_3$ – $W_{75}Re_{25}$ thermocouple. Detailed cell assemblies were shown in Figure 1.2, 2.3 and 2.4.

For runs with synchrotron X-ray, a mixture of MgO and diamond (15 wt.%) was used as the pressure marker. The pressure was calculated using the equation of state of MgO¹⁹. Amorphous boron was adopted as a thermal insulator and X-ray window. A forsterite/enstatite sample was placed inside the graphite capsule, and two rhenium spheres were placed at the middle and top of the sample to detect melting of forsterite using *in situ* X-ray imaging. The images were projected on the fluorescence screen and then magnified and detected by a high-speed CCD camera (C9300, Hamamatsu Co. Jap.). Energy dispersive X-ray diffraction was adopted at a diffraction angle of $\sim 6^\circ$ in conjunction with a germanium solid-state detector.

The pressure was first increased to 10 or 15 GPa. Then, one or several cycles of heating were conducted for each experiment to confirm the heating performance of the BDD heater. The resistivity of a diamond heater was determined during the heating from the applied voltage and current and its dimensions. The recovered samples were polished by a diamond wheel and checked by an optical microscope and a scanning electron microscope (SEM).

1.4 Results and discussion

1.4.1 BDD blocks and tubes

Figure 1.5 shows the synthesized BDD blocks with diameters of ~ 2.5 mm and BDD tubes with various dimensions (such as 2.6/1.5/3.35 and 1.5/1.1/3.0 mm for the outer diameter/inner diameter/length, respectively). The BDD blocks and BDD tubes contained some small cracks. The grain sizes of the granular BDD were measured to be ~ 1 – 5 μm (Figure 1.6). X-ray diffraction patterns of the BDD with various boron

contents show no obvious graphite peaks except for the sample with 0.5 wt% boron (Figure 1.7), which indicates that the graphite may have completely transformed into diamond for the samples with larger boron contents. This observation suggests that boron works both as the dopant and catalyst during the graphite–diamond conversion. Compared with pure diamond, the peaks of BDD shifted to lower angles, suggesting that the involvement of boron expands the diamond lattice.

1.4.2 Sintered BDD tube heater with different boron contents

Figure 1.8 displays the power–temperature relationships of the runs for BDD contents of 0.5, 1.0, 2.0 and 3.0 wt.%. First, several heating-cooling cycles were performed at relatively low temperatures (~1500–2000 °C) to prevent failure of the thermocouple. In the last heating, we tried to generate temperature as high as possible. All the heating cycles showed good reproducibility of the power–temperature relationship except for the first heating cycle. Their relationships can be fitted by a cubic polynomial function. All the BDD heaters with boron contents of 0.5–3.0 wt% were stable during heating.

Figure 1.9 shows the Arrhenius plots of electrical conductivity, which was calculated from the measured total resistance involving heater and electrode during heating by ignoring its dimensional change during compression. No abrupt conductivity changes were observed in all the heating cycles. The conductivities in the first cooling and successive heating cycles showed good reproducibility, whereas the conductivity in the first heating was always lower than the first cooling and successive heating cycles except for 5k2959-01 (1.0 wt.% boron content). As the cracks in BDD tube were probably not perfectly closed due to the diamond support before heating, the lower electrical conductivity obtained from the first heating is attributed to the poorer contact.

For the first cooling and successive heating–cooling cycles, the electrical conductivity of BDD increased with increasing boron content. The electrical conductivity also increased with increasing temperature (semiconductive) for BDD with boron contents < 2.0 wt.%, whereas it showed opposite trend (metallic) for BDD with 3.0 wt.% boron.

For the 5k2959 (1.0 wt.% boron content) experiment, the conductivity in the first heating is higher than that in the first cooling. This is caused by a presence of residual graphite in the BDD tube, which is not well sintered because the heater in the synthesize experiment failed at around 1700 °C. The continuous decrease of conductivity at approximately 1400 °C in the first heating may have been caused by the graphite–diamond conversion from the residual graphite.

1.4.3 BDD powder heater with 3.0 wt.% boron

Figure 1.10a displays the power–temperature relationship of BDD powder tube heater at 15 GPa. Two heating–cooling cycles were conducted. The temperature was increased to 1300 °C in the first cycle. In the second cycle, the thermocouple was broken at around 1600 °C. We continued to increase the power to ~870 W (~3000 °C based on the power–temperature relationship determined up to 1600 °C). A sudden increase of heater resistance occurred at this power. Finally, we increased the power to 1150 W and quenched. The sudden increase of heater resistance indicates something unknown (probably caused by melting of ZrO₂ showed in Figure 1.11a) happened at ~870 W. The power-temperature relationship maybe unreliable at power higher than 870 W. The highest temperature in this run should be >~3000 °C based on power-temperature relationship.

Figure 1.10b shows that the conductivity of BDD powder gradually increased with temperature. With the porosity reduction during the first heating, the conductivity

change was one order of magnitude larger than that of the sintered BDD. Thus, a larger dynamic range of applied voltage was required for heating of the BDD powder tube compared to the sintered BDD tube. The conductivities of the heater in the first cooling and second cycle were similar to those of the sintered BDD tube heater in the corresponding stages.

1.4.4 Pressure generation and X-ray transparency of assembly with BDD heater

Figure 1.12a shows the pressure generation efficiency of cell assembly equipped with sintered BDD or BDG heater at room temperature. Compared with the BDG heater, the BDD heater exhibited lower efficiency for pressure generation at load up to 1500 tons. The pressure was measured to be 8.2 GPa for the assembly with the BDD heater and 10.4 GPa for that with the BDG heater at 1500 tons. Figure 1.12b shows the temperature effect on pressure at 1500 tons for the assembly with the BDD heater. Below 1000 °C pressure increased with increasing temperature and then remained nearly constant in a temperature range between 1000 and 1500 °C. At 1500 tons, the pressure at 1000 °C was ~2.5 GPa higher than that at room temperature.

We also checked the performance of BDD heater by *in situ* X-ray imaging combined with falling sphere method. Two Re spheres are set at top and middle of the forsterite powder. During compression, the top sphere moved and disappeared out of the anvil gap. Only the middle sphere was observed at 1700 °C (Figure 1.4b). The Re sphere (67.57 μm before compression) is clearly visible. Falling of the rhenium sphere was observed at approximately 2300 °C, as estimated from the input power. The falling of the sphere indicates the melting of forsterite. Based on the phase diagram of forsterite²⁰, the melting point of forsterite at 10 GPa was approximately 2300 °C,

confirming that the BDD heater was highly X-ray transparent and could generate temperatures higher than 2300 °C.

1.4.5 Useful remarks for better use of BDD heater

Choice of electrode is an important issue for stable heating of BDD to very high temperatures. We first tested refractory metals such as Mo and Re and their combination (see Table 1.1). The Mo electrode was usually oxidized and melted or reacted with the BDD heater at temperatures higher than 2500 °C at the central part of assembly. Re foil electrode was always melted at ~2500 °C, possibly because of a hot spot in the Re foil. The combination Re and Mo electrode was also tried and not useful for temperatures above 3000 °C because the eutectic melting point between them is approximately 2500 °C^{e.g., 21-22}. It is found that TiC is as a good electrode material because it has a high electrical conductivity and a high eutectic point (~2800 °C at ambient pressure) between TiC and carbon²³. TiC worked well even though the surrounding ZrO₂ was melted (Figure 1.11a). No reaction between TiC and BDD was observed.

There are two common thermal insulators used in the Kawai cell: LaCrO₃ and ZrO₂. LaCrO₃ provides a highly oxidized state, which may lead to instability of BDD. Melting of ZrO₂ always occurred at >2000 °C (depends on cell assembly) because of the relatively low eutectic point (~2000 °C at ambient pressure) between ZrO₂ and MgO²⁴. Figure 1.11a shows the melted ZrO₂ penetrating into the heater and failure of heater prevents ultrahigh temperature generation. Figure 1.11b shows the dendritic texture of ZrO₂ surrounding the TiC electrode. In the case without thermal insulator, the heating efficiency obviously becomes worse (such as 5k2576 in Figure 1.13). Therefore, reducing and refractory thermal insulator should be developed in future for ultrahigh temperature (>3000 °C) generation with a BDD heater. In the current state, the only solution to overcome the low heating efficiency problem is downsize of heater.

Furthermore, melting of the truncated surface of WC anvils bounded by cobalt was frequently observed (Figure 1.11c) because its eutectic point (1300 °C at ambient pressure) is relative low compared with the target temperature and melting point of TiC electrode. We can protect the truncation surface by using a longer electrode (shorter heater) or enhancing the thermal gradient along the electrode. To enhance the thermal gradient between the heater and WC anvils (along the TiC electrode), a thermal insulator should not be used around the TiC electrode.

1.4.6 Ultrahigh temperature generation by BDD heater

We tried different assemblies using BDD heater to generate ultra-high temperature. Figure 1.13 summarizes the power–temperature relationships of the ultrahigh temperature generation experiments. The highest temperature (~3700 °C) was generated in run 1k2455. The cell design of run 1k2455 is shown in Figure 1.3b in the supplemental materials. Figure 1.14b shows the heating log. One heating–cooling cycle was conducted. The power was increased to 400 W (corresponding to 2000 °C) smoothly in 1h. Then, the power–temperature relationship became abnormal, which might have been caused by the compaction of the BDD powder. Therefore, we maintained the power at 433 W for 35 min to complete the compaction process. Then, the power was increased again. The thermocouple was failed when the power reached 576 W (~2600 °C); we maintained the power for 5 min. Finally, we performed the challenge of ultrahigh temperature generation, and reached the highest power (690 W) until the heater was broke down. Figure 1.14a shows the power–temperature diagram of 1k2455. The highest temperature was estimated to be 3700 °C.

Figure 1.15 shows SEM images of the recovered sample. The BDD heater was broken in the middle part of the assembly. The MgO in the middle of the assembly had a fine grain size (~1 μm), whereas the MgO near the electrode had a larger grain size

(~20 μm). This finding may provide evidence of MgO melting around the center. The melting point of MgO from 10 to 15 GPa obtained from DAC experiments and theoretical calculation is 3200-4200°C²⁵⁻²⁹. Our estimated temperature is around the center of temperature range. Melting of the thermocouple and Re chip placed in sample position also occurred, as patchy W-Re alloy was distributed in the quenched MgO melt. These observations suggest that the sample has experienced ultrahigh temperature. We conclude that BDD heater can generate ultrahigh temperature (>3000 °C) at high pressure (>10 GPa).

1.5 Conclusions and perspectives

We succeeded to synthesize BDD tubes and blocks with different boron contents at 15 GPa and 2000 °C. The conductivity of BDD increased with increasing boron concentration, and BDD with boron contents of 0.5–3.0 wt% exhibited good heating performance.

BDD with lower boron content was more likely to be semiconductor having an advantage for decreasing the thermal gradient inside the heater. In contrast, BDD with a high boron content showed metallic behavior, which was an advantage for achieving more stable heating even for fast heating experiments. BDD with lower boron content exhibited higher resistance and is therefore more suitable for a heating system with higher voltage and low current, and vice versa. Depending on the objective, researchers can select different boron contents to obtain BDD with the desired conductivity and heating performance.

BDD with a higher boron content (3 wt.%) is recommended for a BDD powder heater. The resistance of BDD heater is controlled by the boron content, heater porosity and heater geometry. It is obvious that heater with higher porosity has higher resistance.

The powder heater during the initial stage of heating has much larger porosity than that of the sintered ones, thus higher electrical resistance. To compensate the porosity effect, BDD with higher boron content is recommended.

The BDD heater can generate temperatures as high as 3700 °C, as estimated from the input power based on the power–temperature relationship. We confirmed melting Re, a W/Re thermocouple, MgO, ZrO₂ and forsterite at pressures higher than 10 GPa.

It is found that not only the heater material but also related materials (such as the electrode, thermal insulator, and pressure medium) are important for achieving ultrahigh temperature generation. TiC is the best electrode material for a BDD heater. Zirconia and LaCrO₃ are not good thermal insulators for ultrahigh temperature generation using a BDD heater. Thus, the development of these related materials is needed in the future.

Figure 1.16 summarized the advantages of BDD heater compared with heaters using other heating materials. BDD is stable, refractory and highly X-ray transparent (Re sphere <70 μm is clearly visible) at lower mantle conditions. Thus, it shows great potential for melting the deep Earth and enables the structure and physical properties measurement of melts under lower mantle conditions. It can be applied to experiments on measuring melting points of lower mantle or core materials. It also can be applied to measure the partition coefficients of elements between silicate and iron melts, and viscosity of silicate melts under lower mantle conditions.

References in Part I

1. Ito, E., Schubert, G., Romanowicz, B., & Dziewonski, A. (2007). Theory and practice—multianvil cells and high-pressure experimental methods. *Treatise on geophysics*, 2, 197-230.
2. Irifune, T., Kurio, A., Sakamoto, S., Inoue, T., & Sumiya, H. (2003). Ultrahard polycrystalline diamond from graphite. *Nature*, 421, 599-600.
3. Shatskiy, A., Yamazaki, D., Morard, G., Cooray, T., Matsuzaki, T., Higo, Y., ... & Katsura, T. (2009). Boron-doped diamond heater and its application to large-volume, high-pressure, and high-temperature experiments. *Review of Scientific Instruments*, 80(2), 023907.
4. Zerr, A., Diegeler, A., & Boehler, R. (1998). Solidus of Earth's deep mantle. *Science*, 281(5374), 243-246.
5. Fiquet, G., Auzende, A. L., Siebert, J., Corgne, A., Bureau, H., Ozawa, H., & Garbarino, G. (2010). Melting of peridotite to 140 gigapascals. *Science*, 329(5998), 1516-1518.
6. Andrault, D., Bolfan-Casanova, N., Nigro, G. L., Bouhifd, M. A., Garbarino, G., & Mezouar, M. (2011). Solidus and liquidus profiles of chondritic mantle: Implication for melting of the Earth across its history. *Earth and planetary science letters*, 304(1-2), 251-259.
7. Nomura, R., Hirose, K., Uesugi, K., Ohishi, Y., Tsuchiyama, A., Miyake, A., & Ueno, Y. (2014). Low core-mantle boundary temperature inferred from the solidus of pyrolite. *Science*, 1248186.

8. Frost, D. J., Poe, B. T., Trønnes, R. G., Liebske, C., Duba, A., & Rubie, D. C. (2004). A new large-volume multianvil system. *Physics of the Earth and Planetary Interiors*, 143, 507-514.
9. Yamazaki, D., Ito, E., Yoshino, T., Tsujino, N., Yoneda, A., Guo, X., ... & Funakoshi, K. (2014). Over 1 Mbar generation in the Kawai-type multianvil apparatus and its application to compression of $(\text{Mg}_{0.92}\text{Fe}_{0.08})\text{SiO}_3$ perovskite and stishovite. *Physics of the Earth and Planetary Interiors*, 228, 262-267.
10. Yamada, A., Irifune, T., Sumiya, H., Higo, Y., Inoue, T., & Funakoshi, K. I. (2008). Exploratory study of the new B-doped diamond heater at high pressure and temperature and its application to in situ XRD experiments on hydrous Mg-silicate melt. *High Pressure Research*, 28(3), 255-264.
11. Yoneda, A., Xie, L., Tsujino, N., & Ito, E. (2014). Semiconductor diamond heater in the Kawai multianvil apparatus: an innovation to generate the lower mantle geotherm. *High Pressure Research*, 34(4), 392-403.
12. Xie, L., Yoneda, A., Yoshino, T., Fei, H., & Ito, E. (2016). Graphite–boron composite heater in a Kawai-type apparatus: the inhibitory effect of boron oxide and countermeasures. *High Pressure Research*, 36(2), 105-120.
13. Fujimori, N., Imai, T., & Doi, A. (1986). Characterization of conducting diamond films. *Vacuum*, 36(1-3), 99-102.
14. Ushizawa, K., Watanabe, K., Ando, T., Sakaguchi, I., Nishitani-Gamo, M., Sato, Y., & Kanda, H. (1998). Boron concentration dependence of Raman spectra on {100} and {111} facets of B-doped CVD diamond. *Diamond and related materials*, 7(11-12), 1719-1722.

15. Takano, Y., Nagao, M., Sakaguchi, I., Tachiki, M., Hatano, T., Kobayashi, K., ... & Kawarada, H. (2004). Superconductivity in diamond thin films well above liquid helium temperature. *Applied physics letters*, 85(14), 2851-2853.
16. Ekimov, E. A. (2004). EA Ekimov, VA Sidorov, ED Bauer, NN Mel'nik, NJ Curro, JD Thompson, and SM Stishov, *Nature (London)* 428, 542 (2004). *Nature (London)*, 428, 542.
17. Ekimov, E. A., Sirotinkin, V. P., Shatalova, T. B., & Lyapin, S. G. (2015). Thermally stable, electrically conductive diamond material prepared by high-pressure, high-temperature processing of a graphite+ boron carbide mixture. *Inorganic Materials*, 51(3), 225-229.
18. Ekimov, E. A., Sidorov, V. A., Rakhmanina, A. V., Mel'nik, N. N., Sadykov, R. A., & Thompson, J. D. (2006). High-pressure synthesis and characterization of superconducting boron-doped diamond. *Science and Technology of Advanced Materials*, 7(S1), S2.
19. Jamieson, J. C., Fritz, J. N., & Manghnani, M. H. (1982). *High Pressure Research in Geophysics*. Center for Academic Publishing, Tokyo, 27-48.
20. Ohtani, E., & Kumazawa, M. (1981). Melting of forsterite Mg_2SiO_4 up to 15 GPa. *Physics of the Earth and Planetary Interiors*, 27(1), 32-38.
21. Knapton, A. G. (1958). The molybdenum-rhenium system. *J. Inst. Metals*, 87.
22. Savitskii, E. M., Tylkina, M. A., & Povarova, K. B. (1959). Phase diagram of the rhenium–molybdenum system. *Zh Neorg Khim*, 4, 424-34.
23. Seifert, H. J., Lukas, H. L., & Petzow, G. (1996). Thermodynamic optimization of the Ti-C system. *Journal of phase equilibria*, 17(1), 24-35.
24. Yin, Y., & Argent, B. B. (1993). Phase diagrams and thermodynamics of the systems ZrO_2 -CaO and ZrO_2 -MgO. *Journal of phase equilibria*, 14(4), 439-450.

25. Zerr, A., & Boehler, R. (1994). Constraints on the melting temperature of the lower mantle from high-pressure experiments on MgO and magnesioüstite. *Nature*, 371(6497), 506.
26. Cohen, R. E., & Gong, Z. (1994). Melting and melt structure of MgO at high pressures. *Physical Review B*, 50(17), 12301.
27. Du, Z., & Lee, K. K. (2014). High-pressure melting of MgO from (Mg, Fe) O solid solutions. *Geophysical Research Letters*, 41(22), 8061-8066.
28. Liu, Z. J., Sun, X. W., Chen, Q. F., Cai, L. C., Tan, X. M., & Yang, X. D. (2006). High pressure melting of MgO. *Physics Letters A*, 353(2-3), 221-225.
29. Kimura, T., Ohfuji, H., Nishi, M., & Irifune, T. (2017). Melting temperatures of MgO under high pressure by micro-texture analysis. *Nature communications*, 8, 15735.

Table

Table 1.1. Summary of temperature generation using BDD heater. The prefixes “1k” and “5k” in the run numbers correspond to the 1000-ton and 5000-ton presses installed at the Institute for Planetary Materials (Okayama University), respectively, and that of “S” corresponds to the SPEED 1500 press at the SPring-8 synchrotron facility. The heater size is defined in the order of outer diameter, inner diameter, and length. Temperatures lower than 2300 °C were the values indicated by a W–Re thermocouple, whereas those higher than 2300 °C were estimated from the temperature–power relationship below 2300 °C. For the thermal insulator, “no insulator” indicates that a thermal insulator was not used in the cell assembly.

Run No.	Heater		Electrode	Sample	Thermal insulator	P Highest T	
	size / mm	Boron concentration				insulator	GPa / °C
Sintered BDD tube heater							
1k2128	1.0/0.7/2.0	3.0 wt%	Re foil	MgO	ZrO ₂	15	2000
1k2156	2.7/1.7/3.7	3.0 wt%	Mo	MgO	ZrO ₂	15	2630
1k2161	2.8/1.6/3.4	3.0 wt%	Re tube+Mo	MgO	ZrO ₂	15	2400
1k2188	2.6/1.5/6.0	3.0 wt%	Re disk+Mo	MgO	ZrO ₂	15	2500
5k2576	2.6/1.5/9.0	3.0 wt%	Mo	MgO	no insulator	15	2650
S3023	2.8/1.7/9.0	3.0 wt%	Mo	Fosterite	amorphous boron	10	2300
1k2601	1.5/1.0/3.0	2.0 wt%	Mo	pyrope	no insulator	15	2800
5k2959	1.5/1.0/3.0	1.0 wt%	Mo	pyrope	no insulator	15	2850
5k2800	1.5/1.0/3.0	1.0 wt%	TiC +Mo	Al ₂ O ₃	no insulator	15	1600
1k2475	1.5/1.0/3.0	0.5 wt%	TiC +Mo	Al ₂ O ₃	no insulator	15	2000

BDD powder tube heater							
S3038	2.8/2.0/9.0	3.0 wt%	Mo	diopside	amorphous boron	10	2000
5k2743	1.5/1.0/6.0	3.0 wt%	TiC surrounded by ZrO ₂	MgO +Re wire	no insulator	15	>3000
1k2455	1.1/0.7/4.0	3.0 wt%	TiC	MgO +Re wire	no insulator	15	3700

Figures

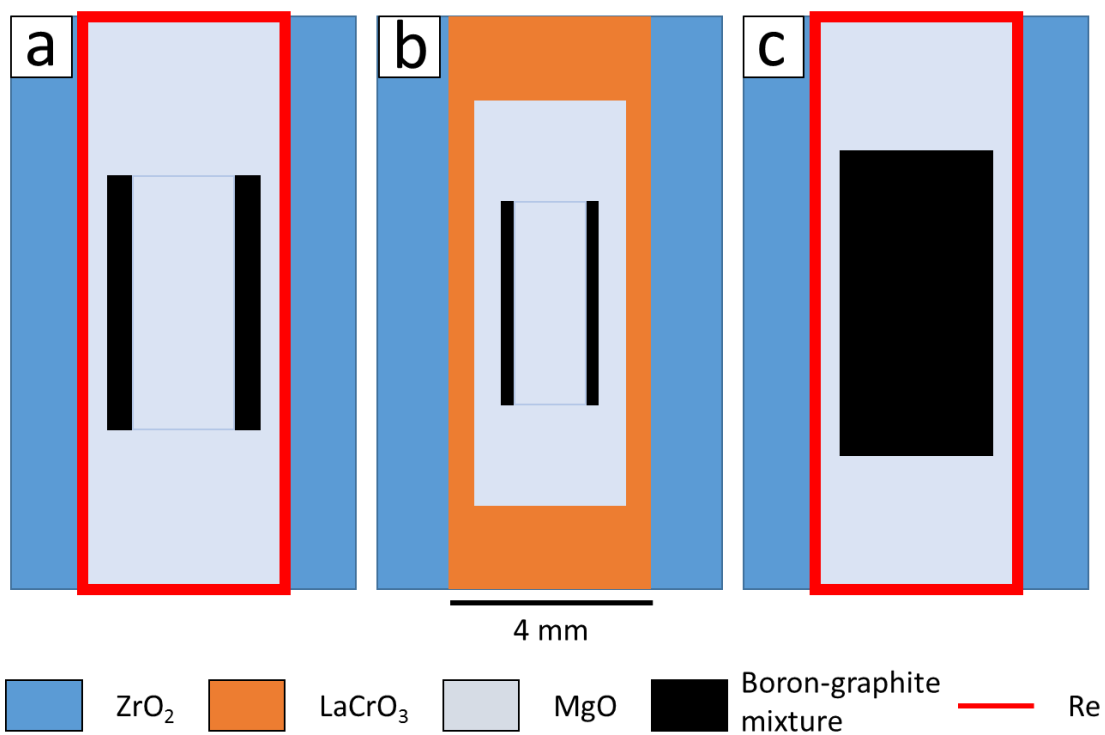


Figure 1.1. Example assemblies for synthesizing BDD tubes and blocks. a, 2.8/1.5 mm BDD tube, where the numbers before and after the slash correspond to the outer and inner diameters, respectively. **b,** 1.5/1.1 mm BDD tube. **c,** 2.8-mm-diameter BDD block.

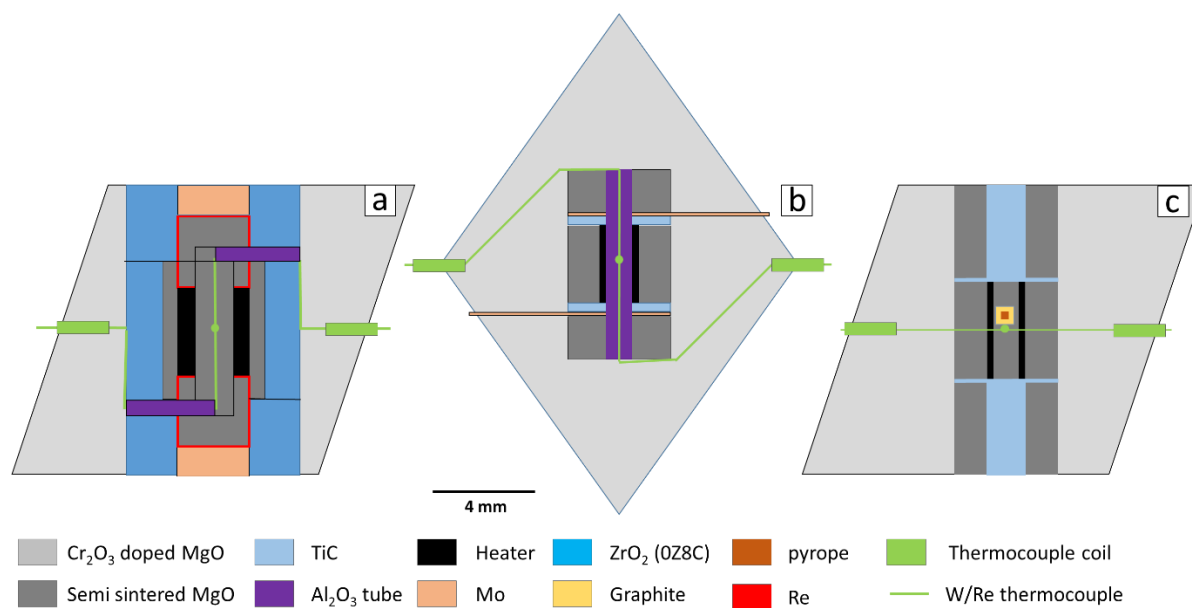


Figure 1.2. Schematic illustration of the cross section of assemblies for heating

experiments using sintered BDD tube as a heater in the Kawai cell. a, Assembly for

run 1k2161: Cr-doped MgO was used as the pressure medium, Ca-stabilized ZrO₂ was

used as the thermal insulator, and a BDD tube (2.8/1.6/3.4 mm) with 3 wt.% boron was

used as the heater. The heater was separated from zirconia by a MgO tube to prevent

the reaction between BDD and zirconia. The heater was filled with MgO. Mo was used

as electrodes, which were separated from the heater by MgO rods wrapped with

rhenium foil. The W/Re thermocouple vertically penetrating the BDD heater was

insulated from rhenium by Al₂O₃ tubes. **b,** Assembly for runs 1k2475 and 5k2800: no

thermal insulator was used around the heater and a BDD tube (1.5/1.0/3.0 mm) with

0.5 or 1.0 wt.% boron was used as the heater. The heater was filled with the Al₂O₃ tube

used for insulating the W/Re thermocouple. **c,** Assembly for runs 5k2959 and 1k2601:

a BDD tube (1.5/1.0/3.0 mm) with 1.0 or 2.0 wt.% boron was tested as a heater, and no

thermal insulator was used around the heater. Pyrope enclosed in a graphite capsule was

used as the test sample. Two thermocouple holes were made using a Nd:YAG laser

operated at 1.06- μ m wavelength (ECOMARKER, ML-7063A).

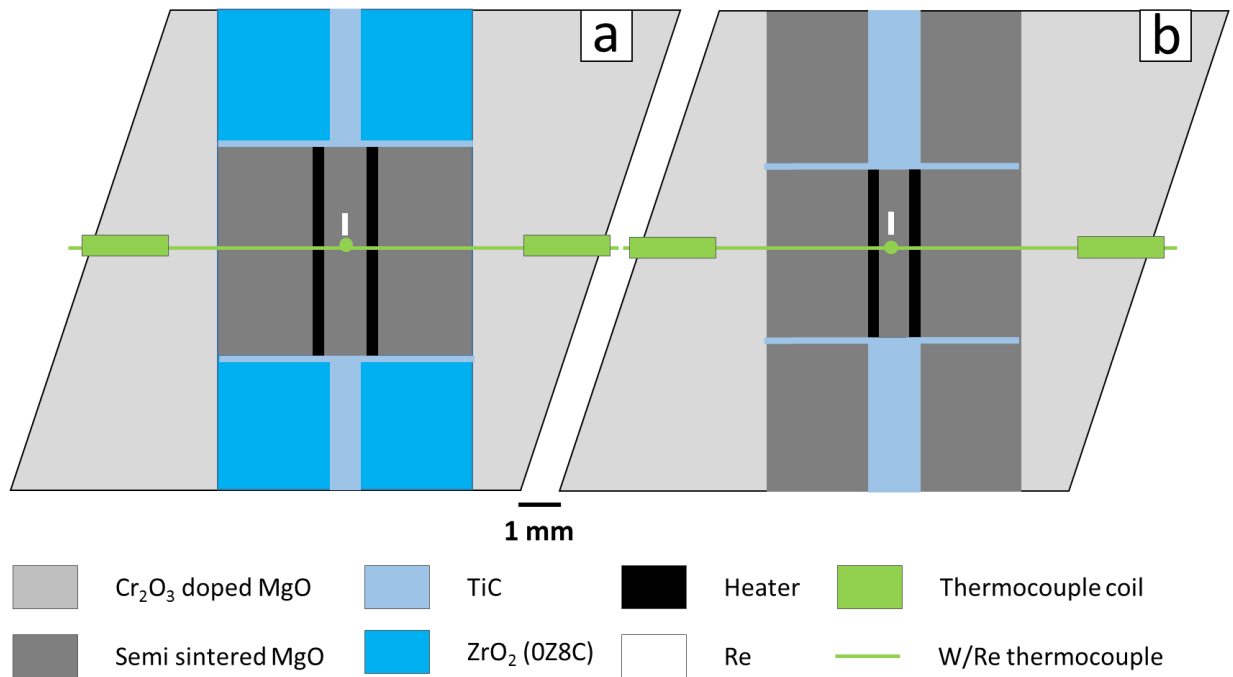


Figure 1.3. Example assemblies for testing BDD powder tube heater. a, 5k2743 and b, 1k2455. A 0.05-mm-diameter thermocouple was used. MgO powder was used near the thermocouple junction to insulate the thermocouple from the heater.

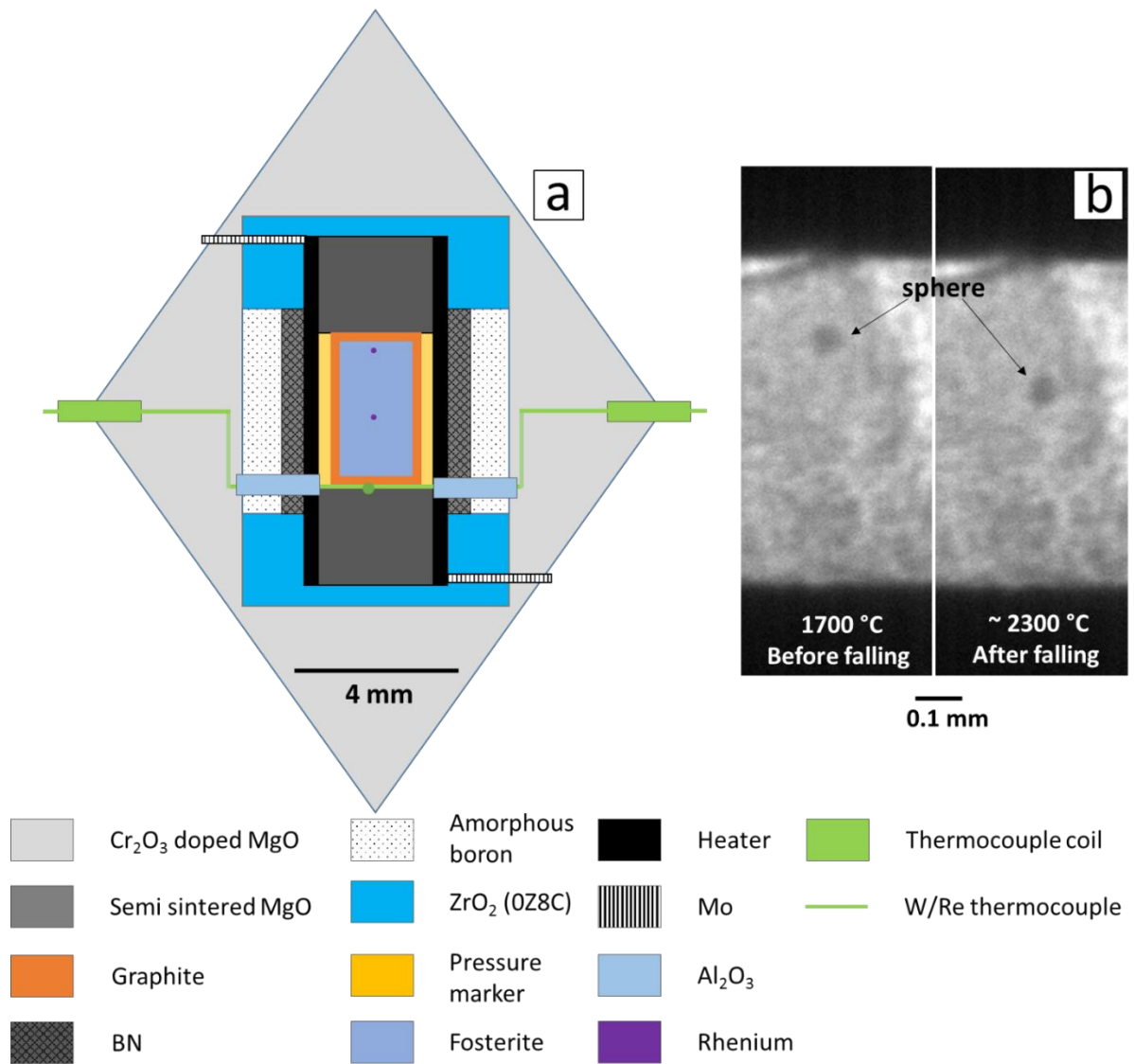


Figure 1.4. Assembly and radiography images for experiments conducted at SPring-8 synchrotron facility. a, Assembly; MgO+15 wt.% diamond was used as the pressure marker. **b**, X-ray shadow images of rhenium sphere in run S3023 using BDD heater.

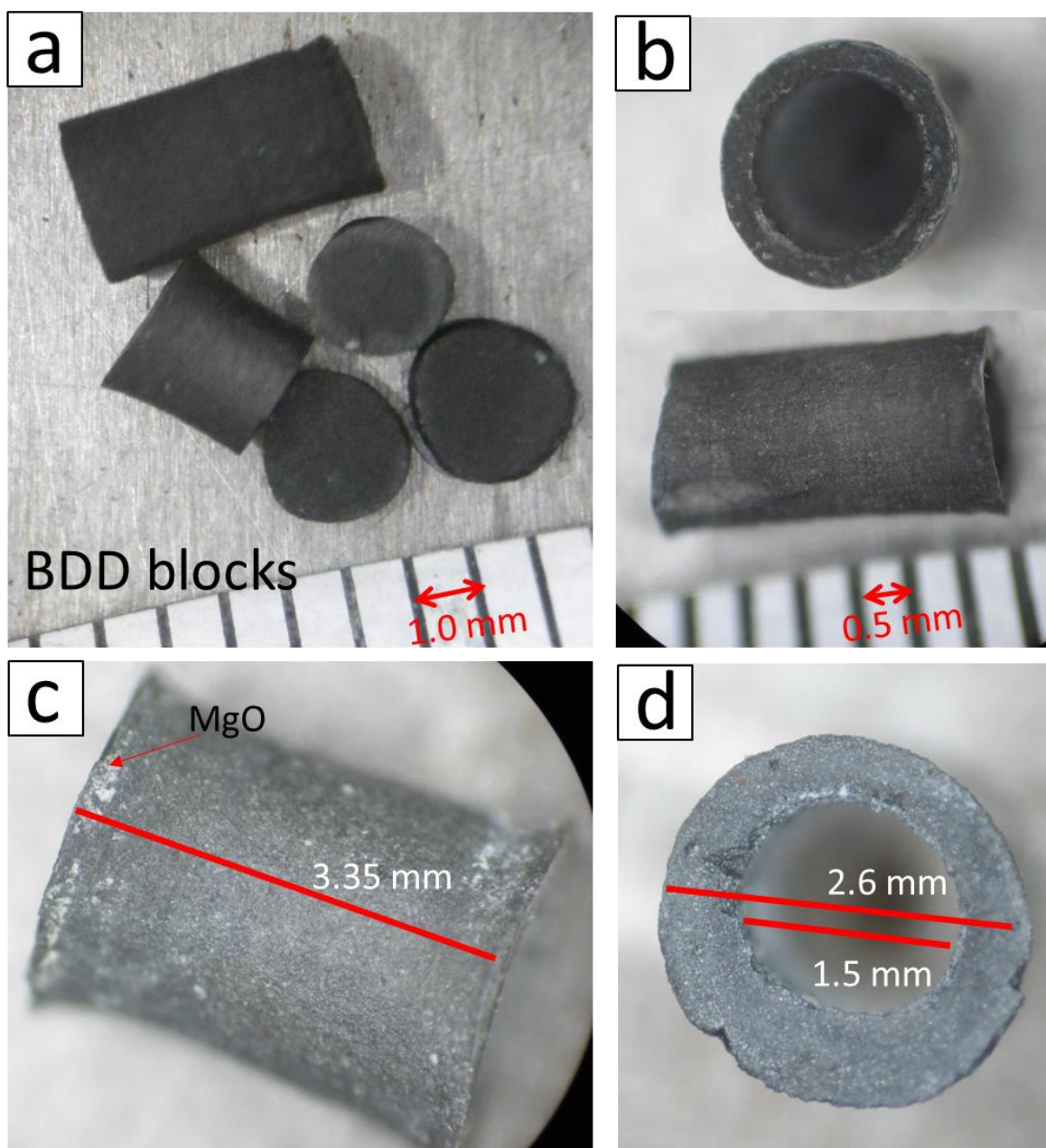


Figure 1.5. Microscopic images of synthesized BDD blocks and tubes. a, Microscopic image of BDD blocks. **b,** Top and side views of 1.5/1.1/3.0 mm BDD tube, which exhibited sufficient strength for assembly as a heater in a Kawai cell. **c,** Side view of 2.6/1.5/3.35 mm BDD tube. The small white patches in the optical microscopy image are residual MgO attached to the BDD tubes. **d,** Top view of 2.6/1.5/3.35 mm BDD tube. The wall thickness of the tubes appears fairly homogeneous.

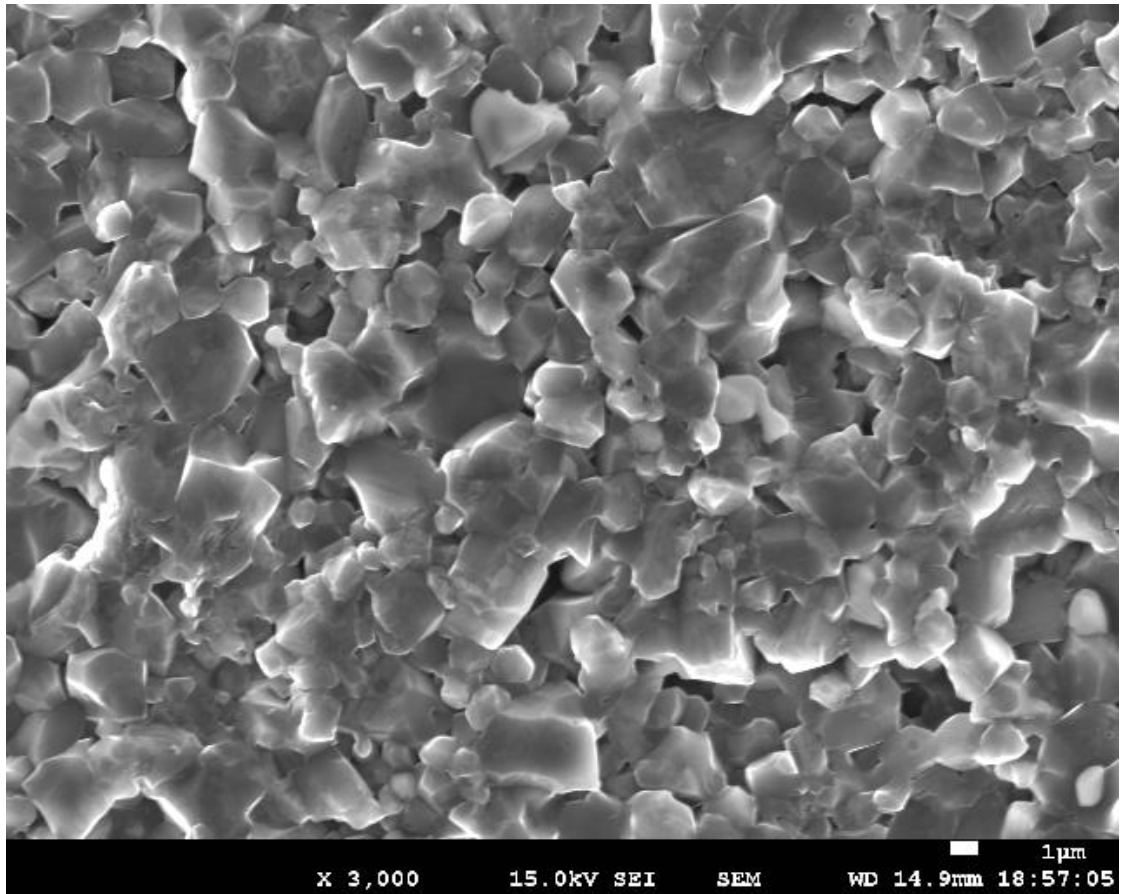


Figure 1.6. Secondary electron image of synthesized BDD. The grain size of granular BDD is $\sim 1\text{--}5\ \mu\text{m}$.

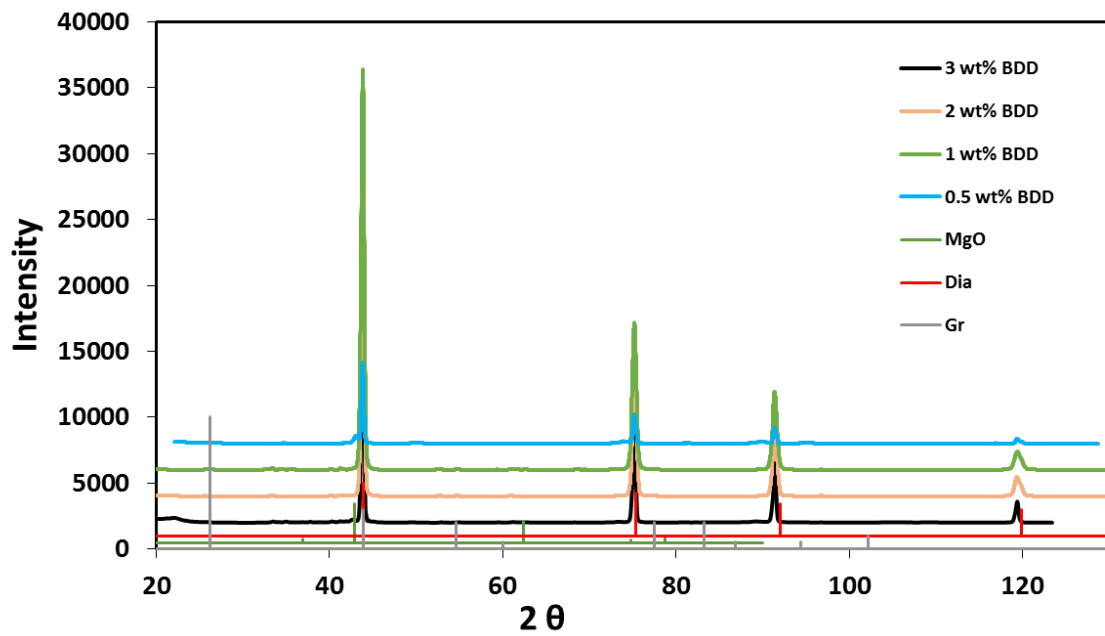


Figure 1.7. X-ray diffraction patterns of the synthesized BDD with various boron contents. Dia: diamond without doping, Gr: graphite, BDD: boron-doped diamond.

The X-ray beam size was 100 μm .

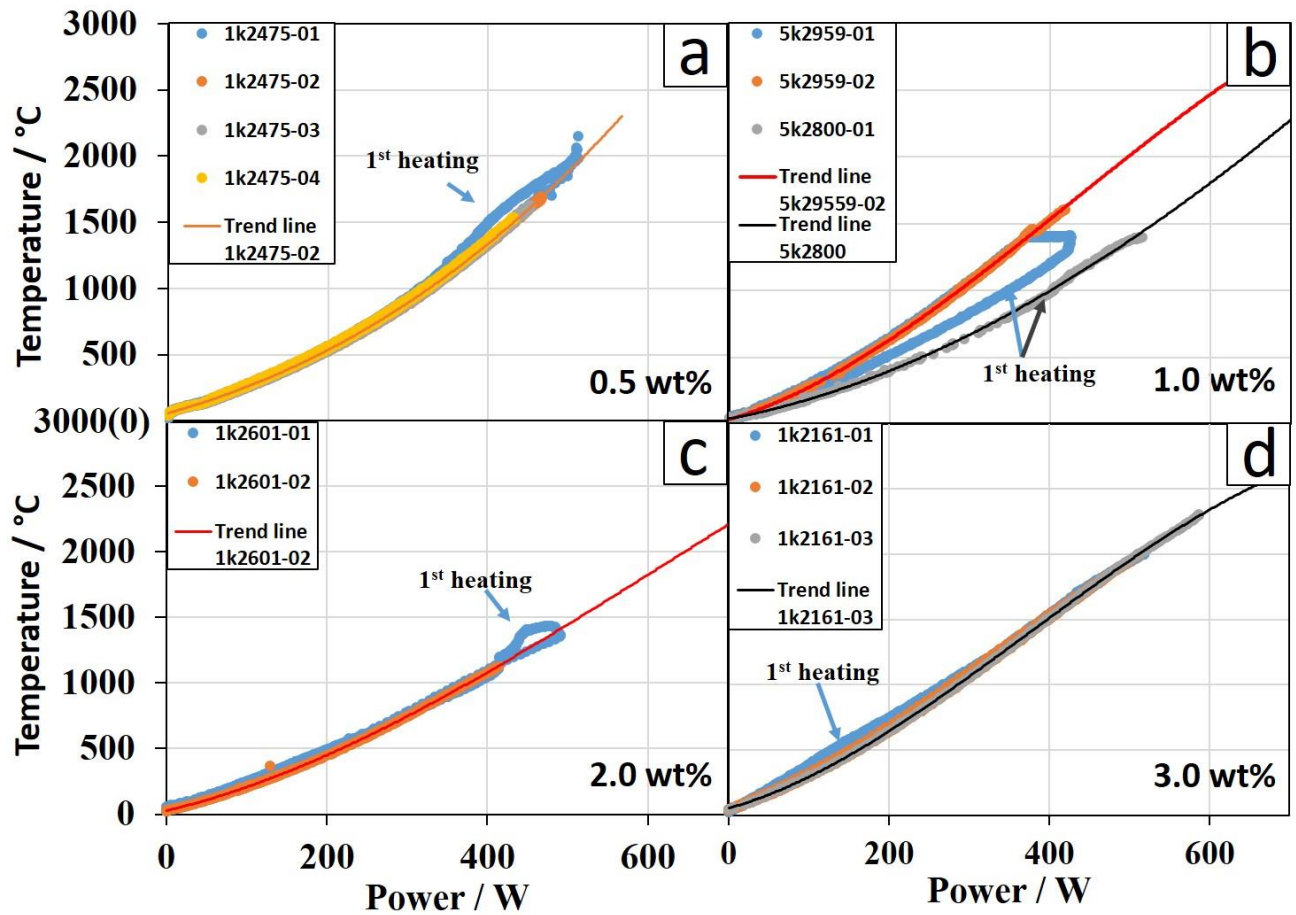


Figure 1.8. The power–temperature diagrams of sintered BDD tube heaters. (a, b, c, d) 0.5, 1.0, 2.0 and 3.0 wt.% BDD, respectively. Assemblies are shown in figure 1.2.

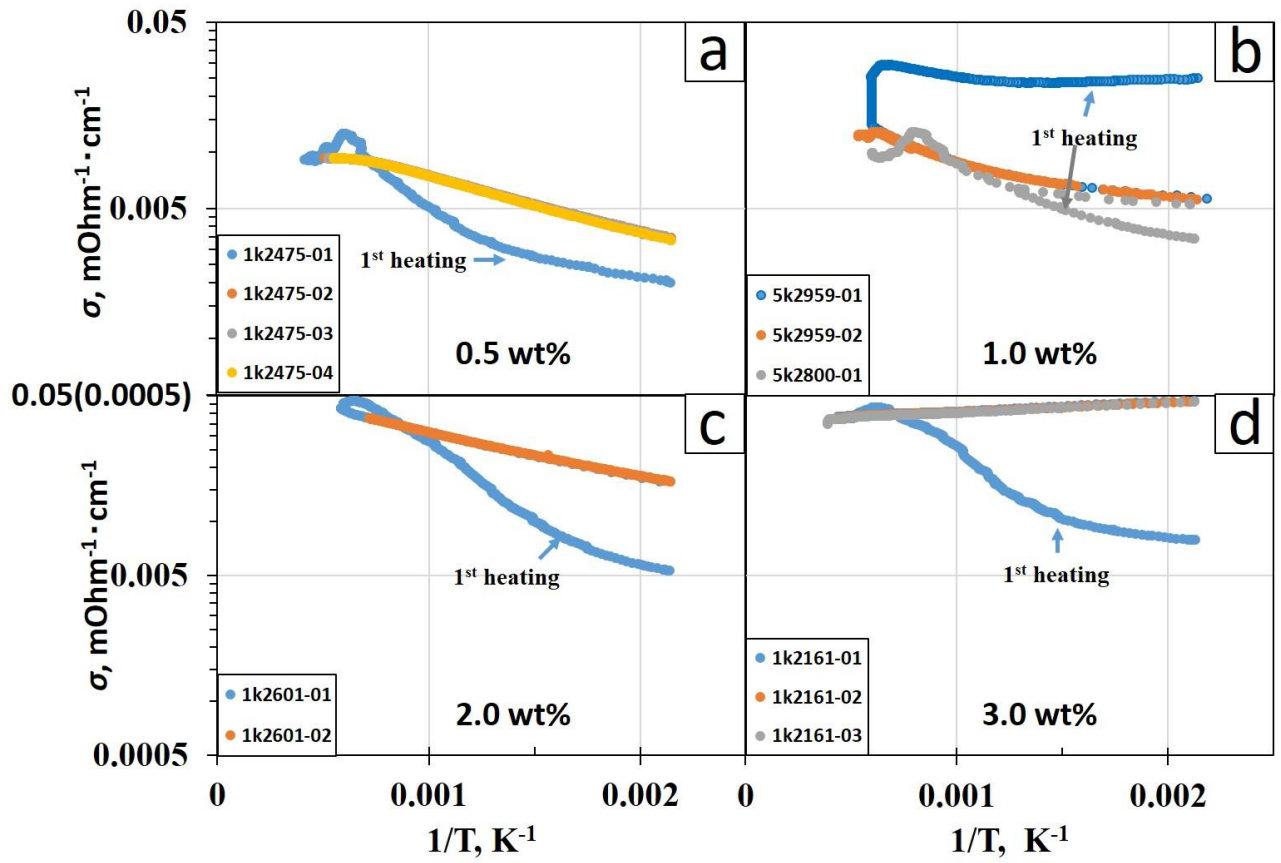


Figure 1.9. Arrhenius plots of sintered BDD tube heaters. (a, b, c, d) 0.5, 1.0, 2.0 and 3.0 wt.% BDD, respectively. Assemblies are shown in figure 1.2.

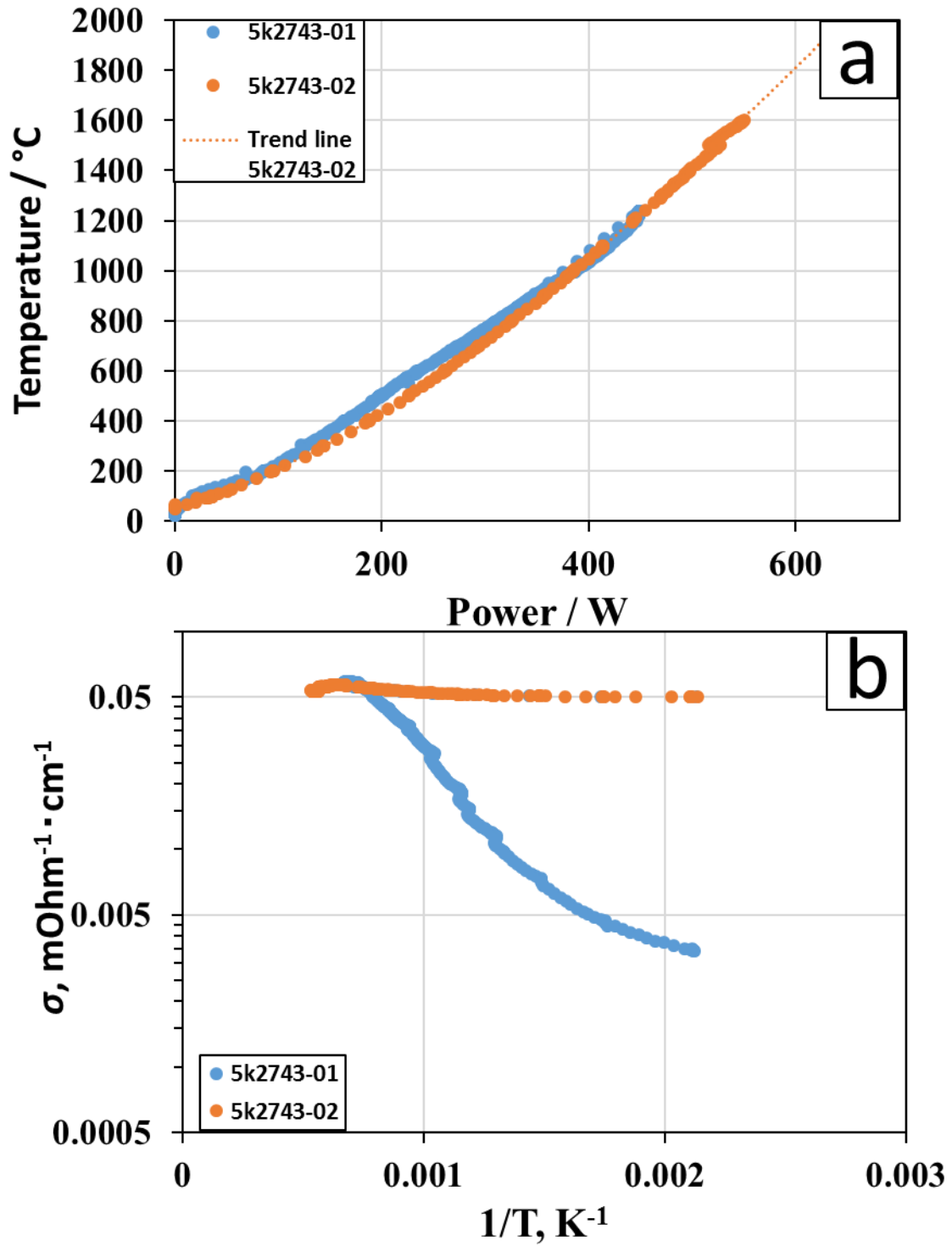


Figure 1.10. Power–temperature relation (a) and Arrhenius plot (b) for BDD powder tube heater (5k2743). Assembly is shown in Figure 1.3a.

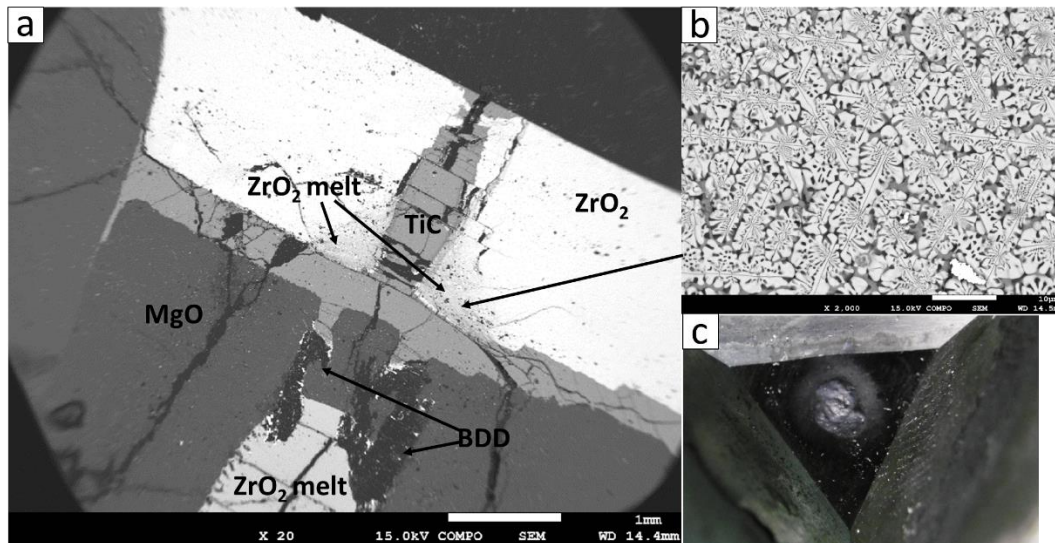


Figure 1.11. (a,b) SEM images of recovered sample of run 5k2743 and (c) optical microscopy image of recovered truncation area of WC cube. b, Dendritic texture indicating melting of ZrO_2 . c, Melting of the truncated surface of WC anvil after the heating generation.

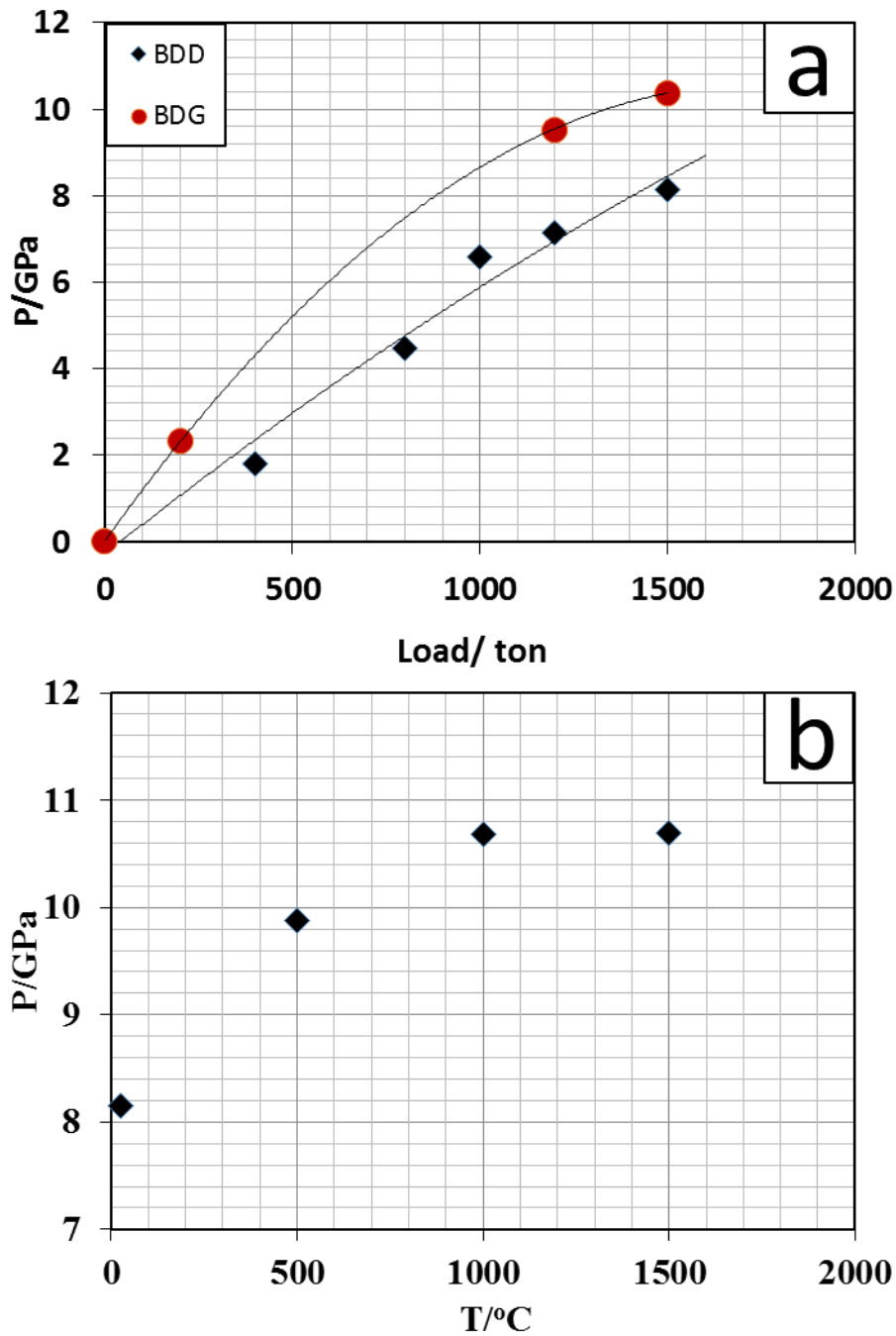


Figure 1.12. Pressure generation efficiency and temperature effect on pressure for an assembly with BDD heater (S3023). a, Load–pressure relation at room temperature; the data were fitted by quadratic functions. **b,** Temperature–pressure relation during the heating at 1500 tons. Assembly is shown in figure 1.4a.

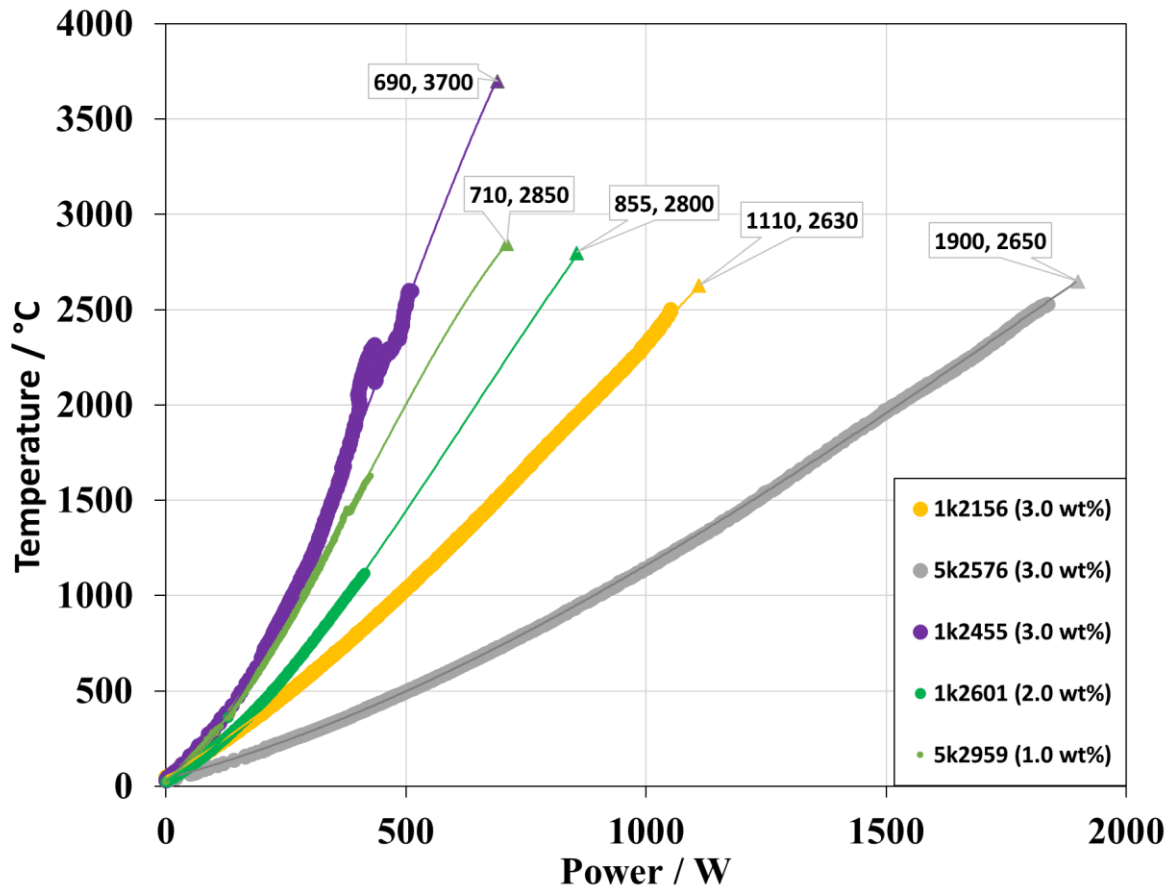


Figure 1.13. Summary of power–temperature relationships in the experiments for ultrahigh temperature generation. ZrO₂ thermal insulator and no thermal insulator was used in run 1k2156 and 5k2576, respectively. A small heater (1.1/0.7/4.0 mm) and no thermal insulator was adopted in run 1k2455. Only the final heating cycle was plotted in each experiment. The triangle symbols mark the highest applied powers and corresponding temperatures estimated by the power–temperature relationship. The numbers in brackets indicate the boron content. The trend lines were fitted by cubic polynomial functions.

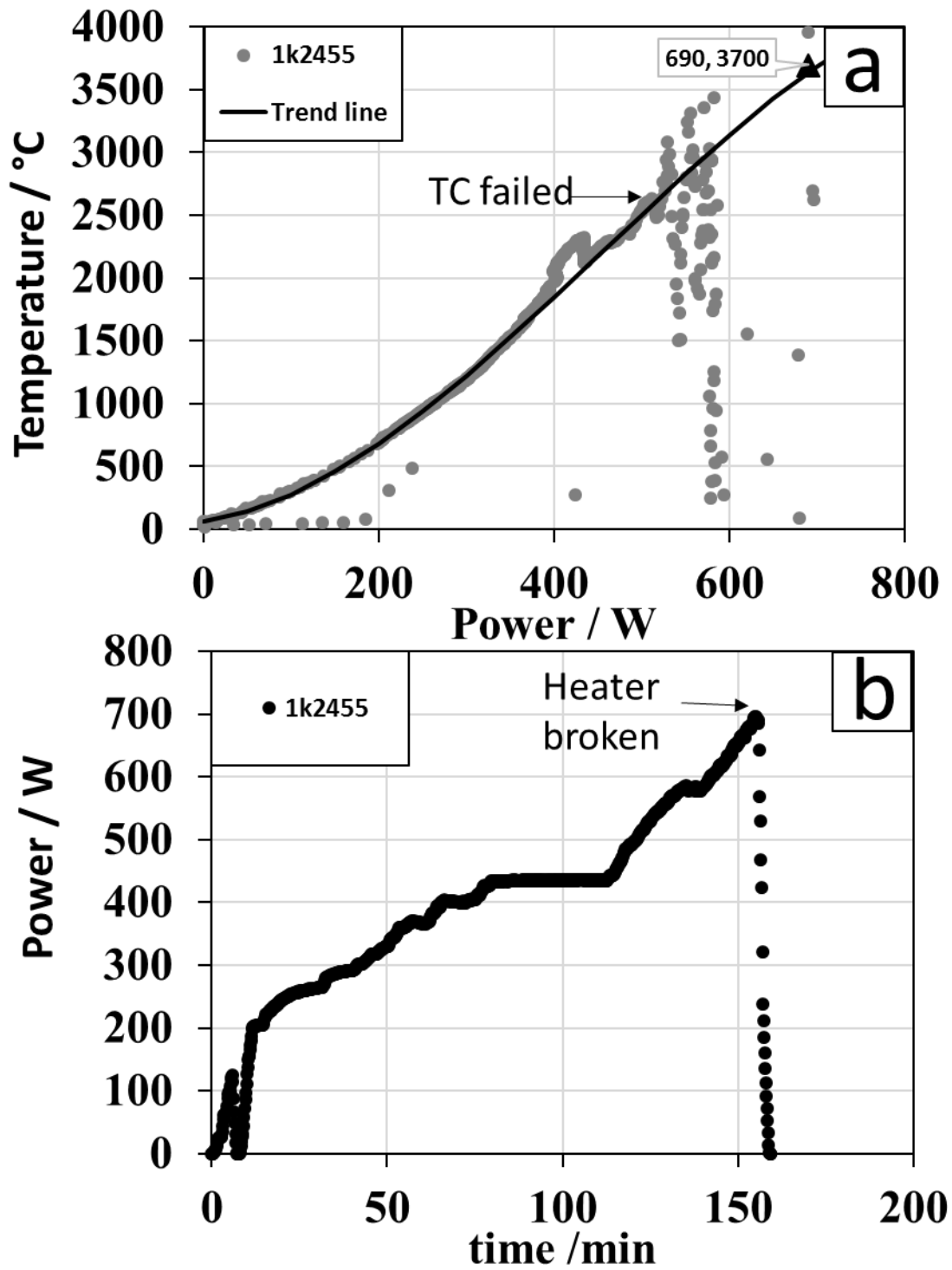


Figure 1.14. Heating log of run 1k2455. a, Power–temperature relation. The trend line was fitted without the data between 400–433 W, where an abnormal power–temperature relationship was caused by the sintering process of the BDD powder heater. TC: thermocouple. **b,** Log between time and power.

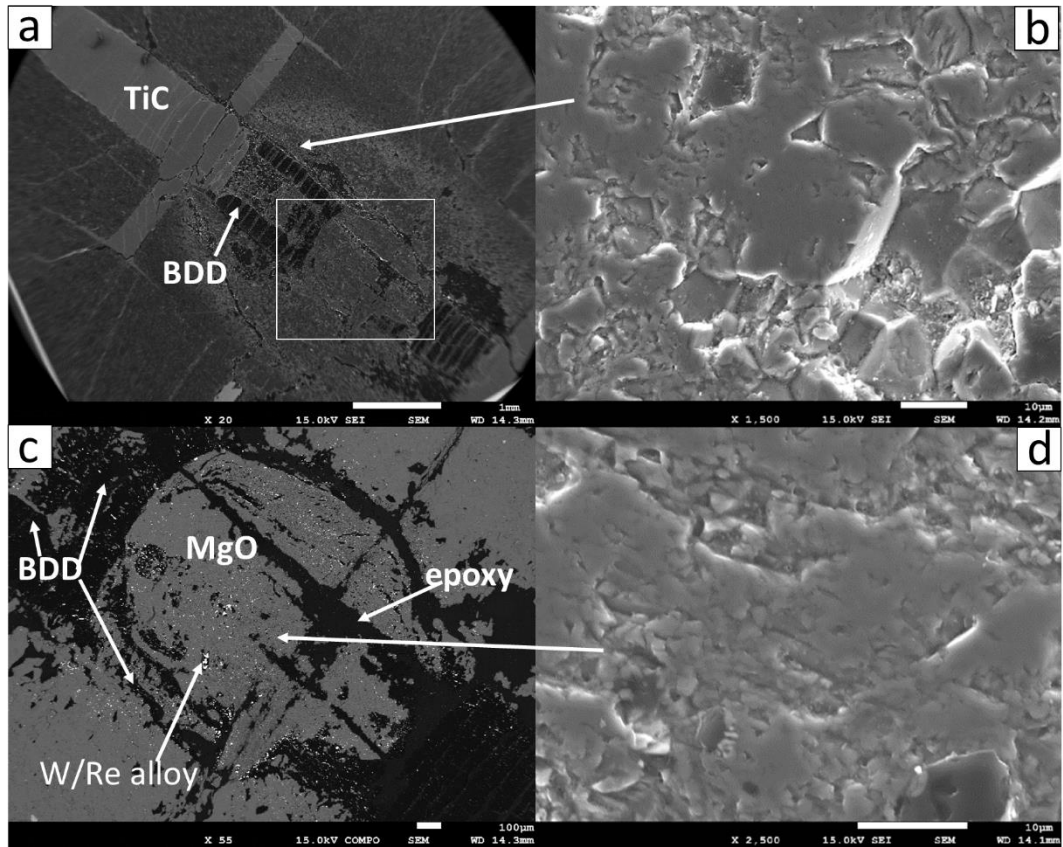


Figure 1.15. (a–d) SEM images of recovered sample of run 1k2455. a, Secondary electron image (SEI) showing wide view of the cell. **c,** Back-scattered electron (BSE) image of the rectangular area in (a). Zoom up SEI images show that the MgO near the electrode exhibited a larger grain size of $\sim 20\ \mu\text{m}$ (b), whereas the grain size of MgO at the center of heater was approximately $1\ \mu\text{m}$ (d).

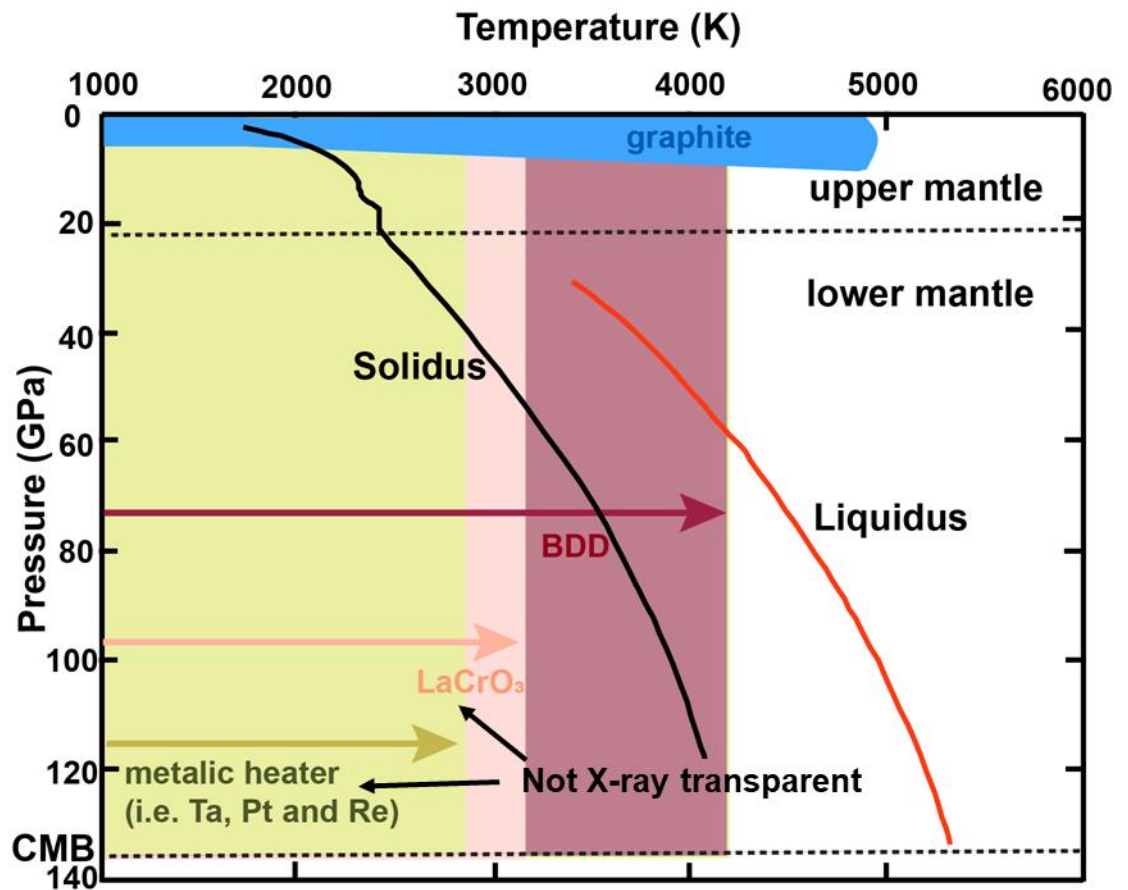


Figure 1.16. Comparison between traditional heating material and BDD in multi-anvil apparatus. Solidus and liquidus of peridotite refers to Ref. 5 . BDD is X-ray transparent and can melt lower mantle materials.

Part 2. Viscosity measurement of silicate melts

up to ~30 GPa

2.1 Abstract

Silicate melts exist in the deep interior of both present and early Earth. Silicate melts have played an important role in the differentiation of our planet's interior at all times. Thus, transport properties, in particular melt viscosity, is a key to understand the chemical evolution of Earth. In this study, we succeeded to extend the experimental measurements of silicate-melt viscosity up to about 30 GPa and more than 3200 K, by devising an *in-situ* falling sphere method coupled with boron-doped diamond heater and ultra-fast camera (1000 f/s) in the multi-anvil apparatus. We determined viscosities of molten forsterite, enstatite and diopside composition from ~5 to 30 GPa and at temperatures near their liquidus. We obtained the viscosity as a function of pressure and temperature for each composition through fitting the experimental data assuming a thermal activation process against the dimensionless temperature normalized by melting temperature at each pressure. The viscosity of silicate melt shows a complex pressure dependence due to the pressure induced densification mechanism change. Through our viscosity data, we firstly verify the four densification mechanisms proposed by molecular dynamic simulations. Our results also show some clues on the composition effect on silicate melt viscosity. Si is a network former at low temperature and low pressure. Its role is similar with 'modifier' at high pressure and high temperature. The modifier with higher density will cause a lower viscosity of silicate melt. The size of modifier has small effect on the viscosity value, but relatively large effect on the pressure dependence of viscosity.

2.2 Introduction

2.2.1 Silicate melts in the Earth

Silicate melts exist in both the early and present Earth. The Earth experienced several episodes of magma-ocean in the early stage of its accretion, due to radiogenic heating from within and gravitational heating by the bombardment of planetesimals from space, especially the giant Moon-forming impact¹. Amount of magma is also expected in the present upper mantle. Seismology detects pronounced low seismic velocity regions in the transition zone and the D'' layer, which have been attributed to partial molten processes^{e.g. 2,3}.

Throughout most of its ~4.5 Gy history, silicate melts have played an important role in the differentiation of our planet's interior^{4,5,6}. Detailed knowledge about major magma forming silicate melts is essential to understand the thermal and chemical evolution of our planet.

2.2.2 Viscosity of magma

Transport properties, in particular melt viscosity, which depend on pressure, temperature and composition, are key parameters to understand various magmatic processes in the Earth^{e.g. 7,8}. In magma ocean, the viscosity is a critical parameter that controls the convection dynamics; then it in turn controls the cooling rate of the early Earth⁸ and the life time of magma ocean⁹. Viscosity of magma ocean is also important for chemical equilibration between silicates and core-forming metallic liquids¹⁰ and the physics of crystal settling in a convecting magma ocean^{7,8}. As for partial melt, viscosity is an important parameter which controls its migration^{eg.11}. The silicate melt viscosity as a function of pressure is critical to understand the differentiation of Earth throughout

its ~4.5 Gy history.

In literatures, there are usually two definitions on viscosity: the dynamic viscosity and kinematic viscosity. Dynamic viscosity is expressed as:

$$\tau = \eta \frac{\partial u}{\partial y} \dots\dots\dots 3.1$$

where η is the dynamic viscosity, τ is stress and $\partial u / \partial y$ is the partial derivative of shear velocity. Kinematic viscosity is expressed as:

$$\nu = \frac{\eta}{\rho} \dots\dots\dots 3.2$$

where ν is the kinematic viscosity and ρ is density. In this study, it refers dynamic viscosity when mentioning viscosity.

2.2.3 Methods to determine viscosity of silicate melt at high pressure

Table 2.1 compares different methods to estimate viscosity of silicate melts at high pressures. Simulation method and high pressure high temperature experimental method, which are complementary, are the two main methods. Compared with experimental method, simulation method is less expensive. There are usually two simulation methods: classical molecular dynamic (C-MD) simulation and first-principle molecular dynamic (FP-MD) simulation. Based on atomistic models, the C-MD simulation permit fast computation, thus can calculate with a relative large cell (more than 2000 atoms) for long time¹²⁻¹⁵. These advantages in practice make it possible to calculate melt viscosity at temperatures more relevant to Earth's mantle¹³. However, the accuracy of C-MD simulation depends on the selection of empirical force field, the uncertainty of which may cause a large uncertainty of the final results.

On the contrary, the FP-MD simulation, instead, make no assumptions about the type of bonding or the shape of the charge density at the cost of calculating the

electronic structure at each time step¹⁶. Thus, maximum atoms used to calculate the viscosity is less than 200 atoms¹⁷, which may cause a large uncertainty owing to a finite size effect. Due to the nature of two different simulation methods, a large discrepancy exists between their results. For example, MD simulation shows that a viscosity increases by a factor of 75 along the 3000 K isotherm from the top of the mantle to the core-mantle boundary for MgSiO₃ melt¹⁴. While, FP-MD reports that a factor over 200 along the 3000 K isotherm from the top of mantle to the core-mantle boundary for MgSiO₃ mel¹⁷.

As for the experimental methods, there are also two methods: viscosity estimation from self-diffusivity of network forming ions and falling sphere method (FSM). The viscosity is related with the self-diffusivity of network ions through Eyring relation:

$$D = \frac{k_B T}{\eta \lambda} \dots \dots \dots 3.3$$

Where D is the diffusivity of Si or O, k_B is the Boltzmann constant, T is temperature (K), λ is translation distance of the diffusion ion (usually taken to be 2.8 Å for silicate melts). Since diffusion experiments have less experimental difficulty than falling sphere method, self-diffusivity of Si and O have been successfully measured up to 15 GPa¹⁸. However, this method is an indirect method and the accuracy of results depends on the validity of Eyring equation and translation distance.

Based on the stoke's law, (in-situ) falling sphere method (FSM) is a direct and most accurate method to measure viscosity. However, the pressure range of this method only reach 13 GPa until now. Extending the pressure range of this method is required.

2.2.4 Previous researches on viscosity measurement by FSM

Kushiro,1976¹⁹ first introduce the FSM to measure viscosity of silicate melt at pressures up to 3 GPa using piston cylinder apparatus. For pressures higher than 3 GPa,

a multianvil apparatus is required for pressure and temperature generation in a large volume. Because of the sample volume reduction, in-situ X-ray observation is critical to determine viscosity precisely. In 1987, Kanzaki et al.²⁰ first developed the method to measure viscosity of silicate melt in a cubic multi-anvil press combined with synchrotron X-ray, and extend the pressure range to ~10 GPa. Reid et al. 2003²¹ implant the in-situ FSM in a Kawai-type multi-anvil and extended the pressure range to 13 GPa.

However, since then, the pressure range has not yet extended due to the technical difficulties caused by ultrahigh melting temperature of silicate and extremely low viscosity of silicate melts at high pressure^{eg.21-24}. More refractory heater material is needed to melt the silicate sample at higher pressure. In order to ensure the laminar flow during sphere falling process, the sphere size must be limited small (<100 μm) for measuring low viscosity, which requires highly X-ray transparent heater material.

The BDD heater is the best candidate to extend FSM to higher pressure because it can generate temperature as high as 4000 K with highly X-ray transparency reported in part 1²⁵. Furthermore, accurate determination of rapid terminal velocity is required in low viscosity measurement, which, in turn, requires ultra-fast camera (~1000 fps) for synchrotron X-ray radiography.

Thus, the combination of BDD heater and ultra-fast camera (>1000 fps) for synchrotron X-ray radiography enables us to conduct the IFSV in the Kawai multi-anvil apparatus to the pressure range of ~30 GPa, which corresponds to the pressure near the bottom depth of MO estimated from the energy balance associating with GP.

2.2.5 Aim of this study

As discussed in part 1, BDD, which is highly X-ray transparent and refractory, is the best candidate for extending the pressure range of in-situ FSM. The purpose of this

study is to apply BDD as a heater for viscosity measurement until the lower mantle conditions and understand the pressure dependence of silicate melt viscosity.

2.3 Experimental procedure

Viscosities were measured by *in-situ* falling sphere method (FSM) in multi-anvil apparatuses (MAA) installed at beamline BL04B1, SPring-8 and beamline Physch e, SOLEIL synchrotron facilities. Cubic WC anvils with 26 mm edge and 4 mm truncation edge length were used as second stage anvils. Rhenium (Re) spheres for falling sphere viscometry were fabricated from stripes of 25 μm thick Re foil through applying flash current generated by a slidac set at 100 V. The Re stripes were immersed in liquid nitrogen to prevent the oxidization and quench the resulting sphere. Diameters in vacuum were measured in a field emission scanning electron microscope with largest uncertainty of $\pm 2 \mu\text{m}$. Spheres of $\sim 70 \mu\text{m}$ diameter were used for the viscosity measurements. Single crystals of forsterite/diopside were first crashed and grinded into powder, then those powders were molded into a cylinder shape (0.7 mm diameter) and semi-sintered at 1273 K for 1h. Enstatite glass was first made from a mixture of MgO and SiO₂ (with molar ration: 1) and grinded into powder, then was molded into a cylinder shape and semi-sintered at 1273 K for 1h.

Figure 2.1a shows the schematic set-up of experiments. The incident and diffracted X-rays will go through horizontal cuttings of first-stage anvils, and vertical gaps between second-stage anvils. The energy dispersive powder X-ray diffraction with white X-rays was conducted using a Ge solid-state detector to identify phases present in a sample and determine pressure. The two-theta angle is ~ 6 degrees. Fast camera (C9300, C11440 at SPring-8 or Photron FASTCAM SA3 at SOLEIL) was adopted to capture the falling path of Re sphere.

The schematic cell assembly is shown in Figure 2.1b. A Cr-doped MgO octahedron with a 10-mm edge length was used as the pressure medium. The edge and vertex of MgO octahedron were truncated. Graphite and BDD were used as heater at pressures lower and higher than 8 GPa, respectively. The preparation of BDD heater were according to Part 1. Mo and TiC were adopted as electrode for graphite and BDD heater, respectively. MgO with 10 wt% diamond (grain size: 1 μm) was used as pressure marker. Polycrystalline sample was placed in graphite capsule. A Re sphere was set near the top of the sample as a probe. A thin sample layer was set between the sphere and graphite cap to prevent contact with the graphite cap. Thermocouple ($\text{W}_{97}\text{Re}_3\text{-W}_{75}\text{Re}_{25}$) was placed below the graphite capsule. No correction was applied for the effect of pressure on the thermocouple emf.

We first compressed the cell to the target load and heated to 1273 ~1773 K. While keeping the temperature, we measured the pressure through X-ray diffractions from the pressure marker. Then we conducted fast-heating (within 4s) just after triggering the fast camera at a speed of 400-1000 fps. It is noted that thermocouple usually broke down during the fast heating. After observing the falling of sphere, we kept the power and measured the pressure again. Finally, samples were recovered and polished for further postmortem analyses after quench and decompression.

Temperatures below 1773 K were measured by $\text{W}_{97}\text{Re}_3\text{-W}_{75}\text{Re}_{25}$ thermocouple and were used to construct a power-temperature relationship in each run. Temperatures during the Re sphere falling were estimated from the input power based on the power-temperature relationship. The temperature gradient in the sample was examined based on the d value of the pressure marker under the assumption of homogeneous pressure inside heater. It means that we attributed the d value difference to the temperature difference; the pressure near thermocouple was determined by combining the EOS of

MgO and temperature measured by thermocouple. At the temperature of 1273K, the resulted temperature difference was estimated to be less than 60 K between thermocouple position and center of capsule, while it was less than 10 K between the center and the top of capsule.

To estimate the temperature overshoot during fast heating, we conducted FEM simulation using COMSOL™. The simulation geometry and material was shown in figure 2.2a. We used a cylindrical shape of pressure medium in order to simply the geometry without losing the essence of critical part inside the heater. In the simulation, fast heating was conducted in 2s. The melting temperature was set to be 2500 K; thermal conductivity of sample was assumed to be 50 and 2.5 W/(mK) before and after melting, respectively. Figure 2.2b shows the resulted temperature log. The latent heat effect turned out to be negligible for the present small sample. The temperatures of position 1 is lower and higher than that of position 3 before and after sample melted, respectively (Figure 2.2c). Thus, the center of sample has lowest temperature after sample melted, which should be caused by the low thermal conductivity of melt. The temperature difference among the four points was less than 40 K, which also support our estimated temperature gradient by EOS of MgO. Since the falling time in our experiments is less than 100 ms, the overshoot of temperature is estimated to be ~60 K (Figure 2.2d).

The pressure was calculated using the equation of state of MgO²⁶. We referred the pressure measured after sphere falling as the pressure during sphere falling, if heater survived after fast heating. If heater failed after fast heating, the pressure measured at same condition in another run or the pressure measured at 1273~1773 K was referred as pressure during sphere falling. The error of pressure was estimated to be 1 GPa for such runs.

2.4 Results and discussions

2.4.1 Falling path and terminal velocity of sphere

An example X-ray shadow images of Re sphere was shown in figure 2.3a. The small Re sphere (67.4 μm before compression) is clearly visible. Figure 2.3b shows the microscopic images of recovered sample. Samples were well sealed in the capsule. The shape of Re sphere was well kept.

The position of sphere in sequential images were fitted by Gaussian fitting. In order to determine the accuracy of sphere position, we took sequential images of sphere before heating. The error of sphere position is determined by statistically analysis of sphere position. One standard deviations of sphere position are 0.6 and 0.4 μm for experiments at SPring-8 and SOLEIL, respectively (figure 2.4). A distance-time diagram can be drawn using the fitted sphere position. Figure 2.5 shows an example of the distance-time diagram. The sphere obviously reached the terminal velocity. The terminal velocity (v_s) of sphere was calculated from the distance-time diagram.

2.4.2 Viscosity of silicate melts as a function of pressure and temperature

The viscosity η of melt was then calculated using Stokes' law:

$$\eta = \frac{2gr_s^2(\rho_s - \rho_m)W}{9v_s E} \dots\dots\dots 3.4$$

$$W = 1 - 2.104 \left(\frac{r_s}{r_c}\right) + 2.09 \left(\frac{r_s}{r_c}\right)^3 - 0.95 \left(\frac{r_s}{r_c}\right)^5 \dots\dots\dots 3.5$$

$$E = 1 + 3.3 \left(\frac{r_s}{h_c}\right) \dots\dots\dots 3.6$$

where r_s is the radius of the sphere, ρ_s and ρ_m are the densities of the sphere

and the melt respectively, and $g=9.803 \text{ m}\cdot\text{s}^{-2}$ is the acceleration due to gravity. W and E are correction factors that account for the wall and end-effects of a finite cylindrical container of radius r_c and height h_c ²⁷. The radius and density of sphere during sphere falling was calculated using the equation of state of Re in ref.28. The density of fosterite, enstatite and diopside melts were calculated from the equation of state of molten Mg_2SiO_4 ²⁹, MgSiO_3 ³⁰ (derived from glass density data) and $\text{CaMgSi}_2\text{O}_6$ ³¹ respectively. The radius r_c and h_c (~0.7 mm) was estimated through recovered sample. Because r_c and h_c is much larger than the sphere size, the resulted viscosity is not sensitive against the input value of r_c and h_c .

To understand the error propagation through the equation of state and stokes' law, we conducted Monte Carlo simulation. The error of pressure, temperature, terminal velocity and sphere size with Gaussian distribution were set as the source errors for propagation. The sampling number for each parameter was 10,000. Figure 2.6 shows the results of Monte-Carlo simulation. The main error source for viscosity was found to be the uncertainty of sphere size in the present set-up. The total viscosity error is less than 10%.

Table 2.2 shows the experimental conditions and results. Good reproducibility was confirmed by repeated experiments at same pressure and same temperature with similar or different sphere sizes. Figure 2.7 shows the viscosities measured in the present work. Owing to the nature of the present IFSM, the resulted viscosities were mainly measured along the liquidus of each sample. In order to describe the pressure and temperature dependence of the viscosity, we assumed a thermal activation process against the dimensionless temperature normalized by melting temperature at each pressure; the functional form is given as:

$$\eta(P, T) = \eta_0 \exp\left(-\frac{E_a(P)}{kT}\right) = \eta_0 \exp\left(-\frac{E_a^*(P)}{(T/T_m)}\right) = \eta_0 \exp\left(-\frac{E_a^*(P)}{T^*}\right) \dots 3.7$$

where η_0 a scale factor; k Boltzmann constant; T absolute temperature; P pressure, T_m melting temperature at pressure P ; E_a activation energy; T^* dimensionless temperature normalized by T_m ; E_a^* dimensionless form of the activation energy. Owing to the formalism of (1), we can easily obtain the pressure dependence of E_a^* through the logarithmic viscosity-pressure diagram along the liquidus (figure 2.7 a, c, e).

$$\ln(\eta) = \ln(\eta_0) + E_a^*(P) \dots \dots \dots 3.8$$

The melt viscosities of Fo, En and Di compositions can be fitted by cubic polynomials until 30 GPa (figure 2.7 a, c, e). Thus, η can be expressed by the following equation:

$$\eta(P, T) = \eta_0 \exp\left(-\frac{a_0 + a_1 P + a_2 P^2 + a_3 P^3}{T^*}\right), \quad P \leq 30 \text{ GPa} \dots \dots \dots 3.9$$

$\eta_0, a_0, a_1, a_2, a_3$ are obtained by fitting the viscosity data at ambient and high pressure using orthogonal distance regression. The melt viscosities of Fo, En and Di compositions is also fitted by two linear sections until 30 GPa (figure 2.12). The fitted parameters are shown in Table 2.3.

Figure 2.7 (b,d,f) shows the calculated viscosities of silicate melts along isothermals using the fitted equations. Viscosity of Fo melt first shows a weak pressure dependence up to ~10 GPa, then shows a gradual increase from ~10 to ~30 GPa. Viscosity of En melt decreases rapidly in the low pressure range up to ~10 GPa, then gradually increases up to 28 GPa, and decreases again above 28 GPa. As for Di melt, viscosity first increases up to ~10 GPa, then decreases up to ~21 GPa, and then increases at pressures higher than 21 GPa. The viscosities of silicate melts along isothermals were also calculated by using two linear sections fitted equations (figure 2.12 b,d,f). It also shows complex pressure dependence of viscosity, which suggests that the complex pressure dependence is irrelevant with the chosen form of fitting equations. In first principle studies, researchers claimed a monotonously increase of the melt viscosity with pressure because the error of calculated viscosity is too large to identify the

complex pressure dependent^{17,32,33}. The average value of calculated data along 3000 K for Fo³², En¹⁷ and Di melt³³ show similar complex pressure dependence of viscosity at pressures lower than 40 GPa. Thus, the first principle studies support our experimental data. The experimentally determined self-diffusion of oxygen and silicon in diopside melt (up to 15GPa)¹⁸ show a positive pressure dependence of viscosity below 10 GPa, and a negative pressure dependence at higher pressure, which also supports our results.

Figure 2.8 shows the activation enthalpy calculated from fitted functions. The activation enthalpy also shows complex pressure dependence. Fo melt (~100 kJ/mol) has the lowest activation enthalpy of viscosity, which is increasing with pressure. Di melt (~250 kJ/mol) has the highest activation enthalpy of viscosity. It increases with pressure until ~5 GPa, then decrease with pressure until ~22 GPa and increase with pressure again until 30 GPa. The activation enthalpy of En melt is ~150 kJ/mol, which first decreases with pressure and then increases with pressure. Those values are consistent with results of first-principle simulation and diffusion experimental data^{17-18,32-39}.

2.4.3 Densification mechanisms of silicate melt under high pressure

The complex pressure dependence of silicate melt viscosity is due to the densification mechanism change with increasing pressure¹⁵. According to the molecular dynamic simulation on sodium silicate melts under high pressure, three densification mechanisms (T1, T2 and T3) are proposed before the coordination number change of Si¹⁵. Here, we refer the densification by increasing coordination number of Si as T4. In T1 region, silicate melts behave like ionic liquids consisting of modifier ions (Mg or Ca) and SiO₄ groups; the main mechanism of densification is thought to be simple compacting; both the coordination number (CN) of modifier and viscosity of silicate

melt increase with pressure (compact effect). In T2 region, the collapse of the SiO₄ network is the main densification mechanism; the viscosity has a negative pressure dependence due to the bending of Si–O–Si; on the contrary, the modifier's CN has a positive pressure dependence for the same reason. In T3 region, the silicate liquids gradually evolve to a coesite-like network structure by increasing the number of four-membered rings and decreasing five to seven-membered rings; viscosity increases with increasing pressure; modifier's CN almost keep constant. In T4 region, silicate liquids densify through coordination number increase of Si; the viscosity may decrease with increasing pressure. The reported CN of Mg in Fo glass has a positive pressure dependence at 0–~10 GPa³⁴. The CNs of Mg, Ca in diopside melt show positive pressure dependence at 0–~20 GPa³⁵. The pressure induced Si CN change in silica glass starts at ~20 GPa³⁶⁻³⁷. We expect the Si CN change in Fo/En /Di melt starts at higher pressure. Because lower SiO₂ content in silicate melt, increases the changing pressure of Si CN. Figure 2.9 shows the pressure range of densification mechanisms for Fo, En and Di melts, based on the pressure dependence of viscosity and modifier's CN. All the four densification mechanisms are identified in our measured pressure range. The densification mechanisms of Fo melt are T2 (0 to ~10 GPa) and T3 (10 to 30 GPa); those of En melt are T2 (0 to ~10 GPa), T3 (~10 to ~28 GPa) and T4 (~28 to 30 GPa); those of Di melt are T1 (0 to ~5 GPa), T2(~5 to ~21 GPa), T3(~21 to ~30 GPa). The densification mechanisms are summarized in Table 2.4.

2.4.4 Composition effect on densification mechanisms and viscosity

Figure 2.10 compares the densification mechanism of En and Di melt as a function of modifier's ion radius. Large modifier ion requires higher pressure to induce the densification mechanism from T1 to T2, T2 to T3 and T3 to T4. The large modifier ion

seems support the SiO_4 group and impedes the bending of the Si-O-Si bond.

Figure 2.11a shows the effect of SiO_2 content on viscosity by comparing viscosity of Fo and En melt. At high temperature (>3000 K), melt is fully depolymerized; the Fo and En melt act like ionic liquids consisting of Mg ions and small SiO_4 groups (or even Mg, Si and O ions); the large silicate anions or O anion are the limiting species; their motions are impeded by Mg cation; thus, melt with higher Mg content has higher viscosity. With decreasing temperature and pressure, the SiO_4 group becomes larger and the degree of polymerization controls viscosity of silicate melts; melt with higher SiO_2 content (lower Mg content) is more polymerized and has higher viscosity. A crossing of viscosity-pressure curves along isotherms may occur for melts with different SiO_2 content (as shown in Figure 2.11a).

Figure 2.11b shows the effect of modifier's density by comparing viscosity of Fo and Fa melt. Fe^{2+} has similar diameter but higher atomic mass than Mg^{2+} . Thus, Fe^{2+} has lower diffusivity than Mg^{2+} , i.e., Fa melt has higher viscosity than Fo melt. Figure 2.11d shows the size effect of modifier by comparing viscosity of En and wollastonite (Wol; CaSiO_3) melt. En melt and Wol melt have similar viscosity, but different pressure dependence. En melt shows negative pressure dependence until ~ 10 GPa, Wol melt shows positive pressure dependence until ~ 6 GPa, which is roughly consistent with T1 region of Di melt. Figure 2.11c shows the effect of mixing configuration entropy by comparing viscosity of En and Di melt. In the T1 and T3 region, Di melt has lower viscosity than En melt because of the mixing configuration entropy. In the T2 region, viscosity is controlled by the bending of Si-O-Si angle. Owing to the Ca cation, Di melt has higher viscosity than En melt due to the less bending of Si-O-Si angle.

2.5 Conclusions

We succeeded in developing the method to extend the viscosity measurement of silicate melt down to the lower mantle. We determined viscosities of molten forsterite, enstatite and diopside from 5 to 30 GPa and at temperatures just above their liquidus. Through fitting the high-pressure data in this study and low-pressure data in literature by homologous temperature scaling, we obtained a viscosity function of pressure (up to 30 GPa) and temperature for each composition (Fo, En, and Di melt).

The viscosity of silicate melts shows complex pressure dependence up to 30 GPa, which is related to the pressure induced densification mechanism change. Combining our viscosity data and pressure induced CN change data in literature, we succeeded to verify all the four densification mechanisms of silicate melt. The size of modifier cation has an influence on the pressure range of densification mechanisms. The large modifier cation can support the SiO_4 group and impedes the bending of Si-O-Si bonding. At low temperature and low pressure, the viscosity of silicate melts is mainly controlled by polymerization of SiO_4 network. Thus, melts with higher SiO_2 content has higher viscosity. At high temperature and high pressure, SiO_4 network is depolymerized or changes to ionic-like SiO_6 network; viscosity is controlled by the content of 'modifier'; melts with lower SiO_2 content has higher viscosity. The modifier cation with higher density, usually has lower diffusivity and higher viscosity. The size of modifier cation has small effect on the viscosity value of melt, but it has a large effect on the pressure dependence of viscosity.

References in Part II

1. Abe, Y. (1993). Physical state of the very early Earth. *Lithos*, 30(3-4), 223-235.
2. Revenaugh, J., & Sipkin, S. A. (1994). Seismic evidence for silicate melt atop the 410-km mantle discontinuity. *Nature*, 369(6480), 474.
3. Helmberger, D., Ni, S., Wen, L., & Ritsema, J. (2000). Seismic evidence for ultralow-velocity zones beneath Africa and eastern Atlantic. *Journal of Geophysical Research: Solid Earth*, 105(B10), 23865-23878.
4. Coltice, N., Moreira, M., Hernlund, J., & Labrosse, S. (2011). Crystallization of a basal magma ocean recorded by helium and neon. *Earth and Planetary Science Letters*, 308(1-2), 193-199.
5. Labrosse, S., Hernlund, J. W., & Coltice, N. (2007). A crystallizing dense magma ocean at the base of the Earth's mantle. *Nature*, 450(7171), 866.
6. Abe, Y. (1997). Thermal and chemical evolution of the terrestrial magma ocean. *Physics of the Earth and Planetary Interiors*, 100(1-4), 27-39.
7. Solomatov V.S. and Stevenson D.J. (1993). Kinetics of crystal growth in a terrestrial magma ocean, *J. Geophys. Res.* 98 (E3), 5407– 5418.
8. Tonks, W. B., & Melosh, H. J. (1990). The physics of crystal settling and suspension in a turbulent magma ocean. *Origin of the Earth*, 151-174.
9. Monteux, J., Andrault, D., & Samuel, H. (2016). On the cooling of a deep terrestrial magma ocean. *Earth and Planetary Science Letters*, 448, 140-149.
10. Rubie, D. C., Melosh, H. J., Reid, J. E., Liebske, C., & Righter, K. E. V. I. N. (2003). Mechanisms of metal–silicate equilibration in the terrestrial magma ocean. *Earth and Planetary Science Letters*, 205(3-4), 239-255.

11. Sakamaki, T., Suzuki, A., Ohtani, E., Terasaki, H., Urakawa, S., Katayama, Y., ... & Ballmer, M. D. (2013). Ponded melt at the boundary between the lithosphere and asthenosphere. *Nature Geoscience*, 6(12), ngeo1982.
12. Wasserman, E. A., Yuen, D. A., & Rustad, J. R. (1993). Molecular dynamics study of the transport properties of perovskite melts under high temperature and pressure conditions. *Earth and planetary science letters*, 114(2-3), 373-384.
13. Lacks, D. J., Rear, D. B., & Van Orman, J. A. (2007). Molecular dynamics investigation of viscosity, chemical diffusivities and partial molar volumes of liquids along the MgO–SiO₂ join as functions of pressure. *Geochimica et Cosmochimica Acta*, 71(5), 1312-1323.
14. Nevins, D., Spera, F. J., & Ghiorso, M. S. (2009). Shear viscosity and diffusion in liquid MgSiO₃: Transport properties and implications for terrestrial planet magma oceans. *American Mineralogist*, 94(7), 975-980.
15. Noritake, F., & Kawamura, K. (2016). Structural transformations in sodium silicate liquids under pressure: A molecular dynamics study. *Journal of Non-Crystalline Solids*, 447, 141-149.
16. Stixrude, L., & Karki, B. (2005). Structure and freezing of MgSiO₃ liquid in Earth's lower mantle. *Science*, 310(5746), 297-299.
17. Karki, B. B., & Stixrude, L. P. (2010). Viscosity of MgSiO₃ liquid at Earth's mantle conditions: Implications for an early magma ocean. *Science*, 328(5979), 740-742.
18. Reid, J. E., Poe, B. T., Rubie, D. C., Zotov, N., & Wiedenbeck, M. (2001). The self-diffusion of silicon and oxygen in diopside (CaMgSi₂O₆) liquid up to 15 GPa. *Chemical Geology*, 174(1-3), 77-86.

19. Kushiro, I., Yoder Jr, H. S., & Mysen, B. O. (1976). Viscosities of basalt and andesite melts at high pressures. *Journal of geophysical research*, 81(35), 6351-6356.
20. Kanzaki, M., Kurita, K., Fujii, T., et al., (1987). A New Technique to Measure the Viscosity and Density of Silicate Melts at High Pressure, In: Manghnani, M. H., Syono, Y., eds., *High-Pressure Research in Mineral Physics*. Terrapub/AGU, Tokyo. 195–200.
21. Reid, J. E., Suzuki, A., Funakoshi, K. I., Terasaki, H., Poe, B. T., Rubie, D. C., & Ohtani, E. (2003). The viscosity of CaMgSi₂O₆ liquid at pressures up to 13 GPa. *Physics of the Earth and Planetary Interiors*, 139(1-2), 45-54.
22. Spice, H., Sanloup, C., Cochain, B., De Grouchy, C., & Kono, Y. (2015). Viscosity of liquid fayalite up to 9 GPa. *Geochimica et Cosmochimica Acta*, 148, 219-227.
23. Cochain, B., Sanloup, C., Leroy, C., & Kono, Y. (2017). Viscosity of mafic magmas at high pressures. *Geophysical Research Letters*, 44(2), 818-826.
24. Liebske, C., Schmickler, B., Terasaki, H., Poe, B. T., Suzuki, A., Funakoshi, K. I., ... & Rubie, D. C. (2005). Viscosity of peridotite liquid up to 13 GPa: Implications for magma ocean viscosities. *Earth and Planetary Science Letters*, 240(3-4), 589-604.
25. Xie, L., Yoneda, A., Yoshino, T., Yamazaki, D., Tsujino, N., Higo, Y., ... & Ito, E. (2017). Synthesis of boron-doped diamond and its application as a heating material in a multi-anvil high-pressure apparatus. *Review of Scientific Instruments*, 88(9), 093904.

26. Tange, Y., Nishihara, Y., & Tsuchiya, T. (2009). Unified analyses for P-V-T equation of state of MgO: A solution for pressure-scale problems in high P-T experiments. *Journal of Geophysical Research: Solid Earth*, 114(B3).
27. Faxén, H. (1922). Der Widerstand gegen die Bewegung einer starren Kugel in einer zähen Flüssigkeit, die zwischen zwei parallelen ebenen Wänden eingeschlossen ist. *Annalen der Physik*, 373(10), 89-119.
28. Zha, C. S., Bassett, W. A., & Shim, S. H. (2004). Rhenium, an in situ pressure calibrant for internally heated diamond anvil cells. *Review of scientific instruments*, 75(7), 2409-2418.
29. de Koker, N. P., Stixrude, L., & Karki, B. B. (2008). Thermodynamics, structure, dynamics, and freezing of Mg₂SiO₄ liquid at high pressure. *Geochimica et Cosmochimica Acta*, 72(5), 1427-1441.
30. Petitgirard, S., Malfait, W. J., Sinmyo, R., Kuppenko, I., Hennem, L., Harries, D., ... & Rubie, D. C. (2015). Fate of MgSiO₃ melts at core–mantle boundary conditions. *Proceedings of the National Academy of Sciences*, 112(46), 14186-14190.
31. Rigden, S. M., Ahrens, T. J., & Stolper, E. M. (1989). High-pressure equation of state of molten anorthite and diopside. *Journal of Geophysical Research: Solid Earth*, 94(B7), 9508-9522.
32. Ghosh, D. B., & Karki, B. B. (2011). Diffusion and viscosity of Mg₂SiO₄ liquid at high pressure from first-principles simulations. *Geochimica et Cosmochimica Acta*, 75(16), 4591-4600.
33. Verma, A. K., & Karki, B. B. (2012). First-principles study of self-diffusion and viscous flow in diopside (CaMgSi₂O₆) liquid. *American Mineralogist*, 97(11-12), 2049-2055.

34. Benmore, C. J., Soignard, E., Guthrie, M., Amin, S. A., Weber, J. K. R., McKiernan, K., ... & Yarger, J. L. (2011). High pressure X-ray diffraction measurements on Mg₂SiO₄ glass. *Journal of Non-Crystalline Solids*, 357(14), 2632-2636.
35. Sun, N., Stixrude, L., de Koker, N., & Karki, B. B. (2011). First principles molecular dynamics simulations of diopside (CaMgSi₂O₆) liquid to high pressure. *Geochimica et Cosmochimica Acta*, 75(13), 3792-3802.
36. Benmore, C. J., Soignard, E., Amin, S. A., Guthrie, M., Shastri, S. D., Lee, P. L., & Yarger, J. L. (2010). Structural and topological changes in silica glass at pressure. *Physical Review B*, 81(5), 054105.
37. Sanloup, C., Drewitt, J. W., Konôpková, Z., Dalladay-Simpson, P., Morton, D. M., Rai, N., ... & Morgenroth, W. (2013). Structural change in molten basalt at deep mantle conditions. *Nature*, 503(7474), 104.
38. Presnall, D. C. (1995). Phase diagrams of Earth-forming minerals. *Mineral physics and crystallography: A handbook of physical constants*, 2, 248-268.
39. Gasparik, T. (1996). Melting experiments on the enstatite-diopside join at 70–224 kbar, including the melting of diopside. *Contributions to Mineralogy and Petrology*, 124(2), 139-153.
40. Shen, G., & Lazor, P. (1995). Measurement of melting temperatures of some minerals under lower mantle pressures. *Journal of Geophysical Research: Solid Earth*, 100(B9), 17699-17713.

Tables

Table 2.1 comparison among methods to estimate viscosity of silicate melt at high pressure

Molecular dynamic simulation		
	Classical	First Principle
Advantages	Fast computation, large cell, long time process simulation	No assumption on bonding or the shape of charge density
Disadvantages	Accuracy depends on model of empirical force field	Slow computation, limited cell size and short time process
Experimental method		
	self-diffusivity method	Falling sphere method
Advantages	Less technical difficulty Indirect method, accuracy depends on	Direct method, accurate
Disadvantages	the validity of Eyring equation and translation distance	More technical difficult

Table 2.2. Summary of experimental conditions and results.

Run ^a	sample	P (GPa)	T (K) ^b	ds (μm) ^c	v_s (mm/s)	η (mPa.s)
Experiments along liquidus						
MA23	Fo	5.7±0.7	2420±100	76±2	1.641±0.006	27±1.4
MA19	Fo	9.6±0.7	2573±100	130±2	4.3±0.02	21±0.4
MA30	Fo	12.7±0.7	2700±100	60±2	1.05±0.02	25.8±1.6
MA28	Fo	20.07±0.04	2793±100	59±2	0.823±0.006	32±2
MA24	Fo	23.9±0.6	2873±100	67±2	0.747±0.003	44±3
MA26	Fo	29±1	3000±150	60±2	0.566±0.003	48±3
S3259	En	4.83±0.3	2203±50	67±2	0.901±0.004	40.2±2.1
S3170	En	8.8±1	2453±150	144±2	5.05±0.03	20.4±0.4
S3171	En	8.8±0.4	2473±50	83±2	2.2±0.02	21.6±1.7
S3172	En	14.7±0.5	2645±50	76±2	3.1±0.1	12.8±0.8
S3175	En	15.3±1	2623±100	68±2	2.58±0.05	12.9±0.7
S3219	En	24.1±0.5	2836±90	70±2	1.85±0.01	19.1±0.9
S3220	En	29.9±0.7	3250±100	67±2	2.69±0.02	12±0.6
S3173	Di	9.9±0.7	2400±150	143±2	1.75±0.04	58±2
MA34	Di	12.6±0.7	2500±100	73±2	1.198±0.005	31.9±2
MA32	Di	20.25±1	2550±100	65±2	1.89±0.007	16.3±1
S3267	Di	23±1	2903±100	67±2	3.44±0.02	9.4±0.5
S3269	Di	23±1	2793±100	77±2	3.21±0.04	12.7±0.5
S3291	Di	26±0.8	2903±100	69±2	3.5±0.1	9.7±0.5
Experiments beyond liquidus						
MA35	En	5.7±1	2450±100	70±2	1.44±0.01	26.9±1.4
S3256	Di	5±1	2453±100	73±2	1.67±0.01	23.9±1.1
S3257	Di	4.76±0.3	2303±50	72±2	0.915±0.006	42.8±2.1

S3260	Di	5±1	2313±50	70±2	0.91±0.006	40.4±2
MA31	Di	5.7±1	2400±100	67±2	1.57±0.01	23.1±1

a. The prefixes “S” and “MA” at the head of the run numbers specify the experiments at beamline BL04B1 (SPring 8, Japan) and beamline Physch , (SOLEIL, France), respectively.

b. Liquidus temperatures of Fo and En composition are referred to Ref. 38 and reference therein, while that of Di to Ref. 39 and Ref. 40 below and above 17 GPa, respectively.

c. *ds*: diameter of spheres at ambient pressure.

Table 2.3 | Summary of fitted parameters using modified homologous scaling.

Parameters in broken line fitting ^a						
Compositio n	η_0	a_0	a_1	b_0	b_1	P_0 /GPa
Mg₂SiO₄	2.3(12) x 10 ⁻⁴	5.12 (56)	-0.062 (1)	4.14((52)	0.043(5)	9.65
MgSiO₃	7.63(484) x 10 ⁻⁵	8.45 (70)	-0.33 (6)	5.23 (70)	0	9.65
CaMgSi₂O₆	3.17(685) x 10 ⁻⁸	17 (2)	-0.263 (8)	12.8(20)	0	18
Fe₂SiO₄^b	1.4(5) x 10 ⁻³	4.0 (4)	-0.097 (20)	0	0	10
CaSiO₃^c	2.6(13) x 10 ⁻⁵	9.2(5)	-0.15(1)	0	0	10
Parameters in cubic polynomial fitting ^d						
Compositio n	η_0	c_0	c_1	c_2	c_3	
Mg₂SiO₄	1.72 (160) x 10 ⁻⁴	5.43 (104)	-0.128 (24)	9.17 (179) x 10 ⁻³	-1.55 (37) x 10 ⁻⁴	
MgSiO₃	1.49 (45) x 10 ⁻⁵	10.35 (34)	-0.645 (23)	3.74 (27) x 10 ⁻²	-6.7 (7) x 10 ⁻⁴	
CaMgSi₂O₆	8.9 (150) x 10 ⁻⁸	16.4 (18)	- 0.346(55)	7.18 (536) x 10 ⁻³	-2.1 (139) x 10 ⁻⁵	

a. Linear fittings were conducted on the two sections independently, as $E_a^*(P) = \begin{cases} a_0 + a_1P, & P \leq P_0 \\ b_0 + b_1P, & P > P_0 \end{cases}$.

b, c. The data of Fe₂SiO₄ and CaSiO₃ refers to ref. 22 and ref. 23, respectively. The fitted parameters were used to calculate the viscosity of molten Fa and Wo in Extended Data Fig. 4 b, &d.

d. Cubic polynomial fitting was based on the equation as $E_a^*(P) = c_0 + c_1P + c_2P^2 + c_3P^3$.

Table 2.4 Pressure ranges of densification mechanisms for Fo, En and Di melt.

Pressure/GPa	T1	T2	T3	T4
Fo melt	≤ 0	0-10	10-30	>30
En melt	≤ 0	0-10	10-28	28-?
Di melt	0-10	10-22	22-30	>30

Figures

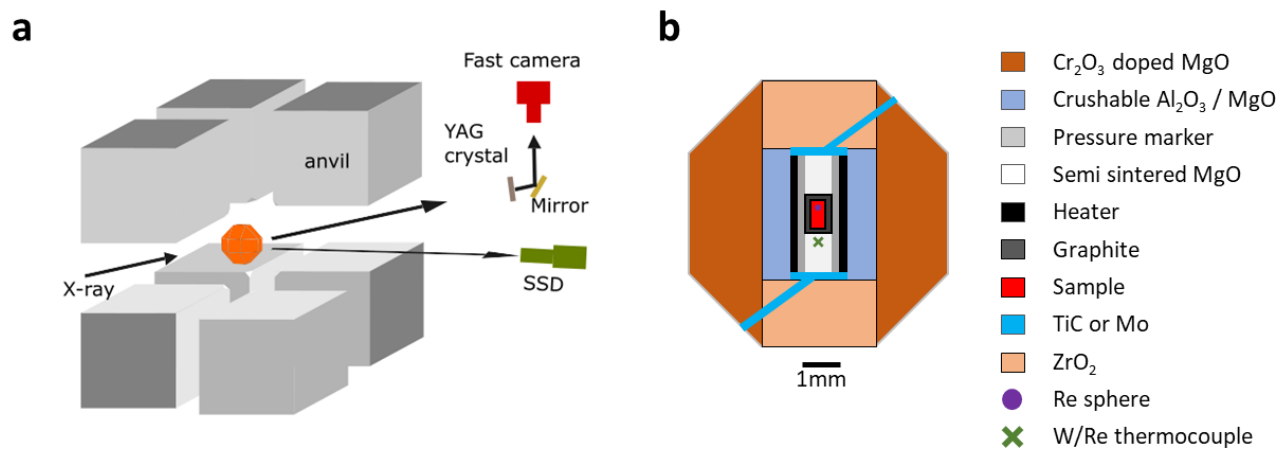


Figure 2.1 Experimental set-up and cell assembly. **a**, Experimental set-up at synchrotron facilities; SSD: Germanium solid-state detector; **b**, Schematic cross-sections of octahedron shown by orange color in (a).

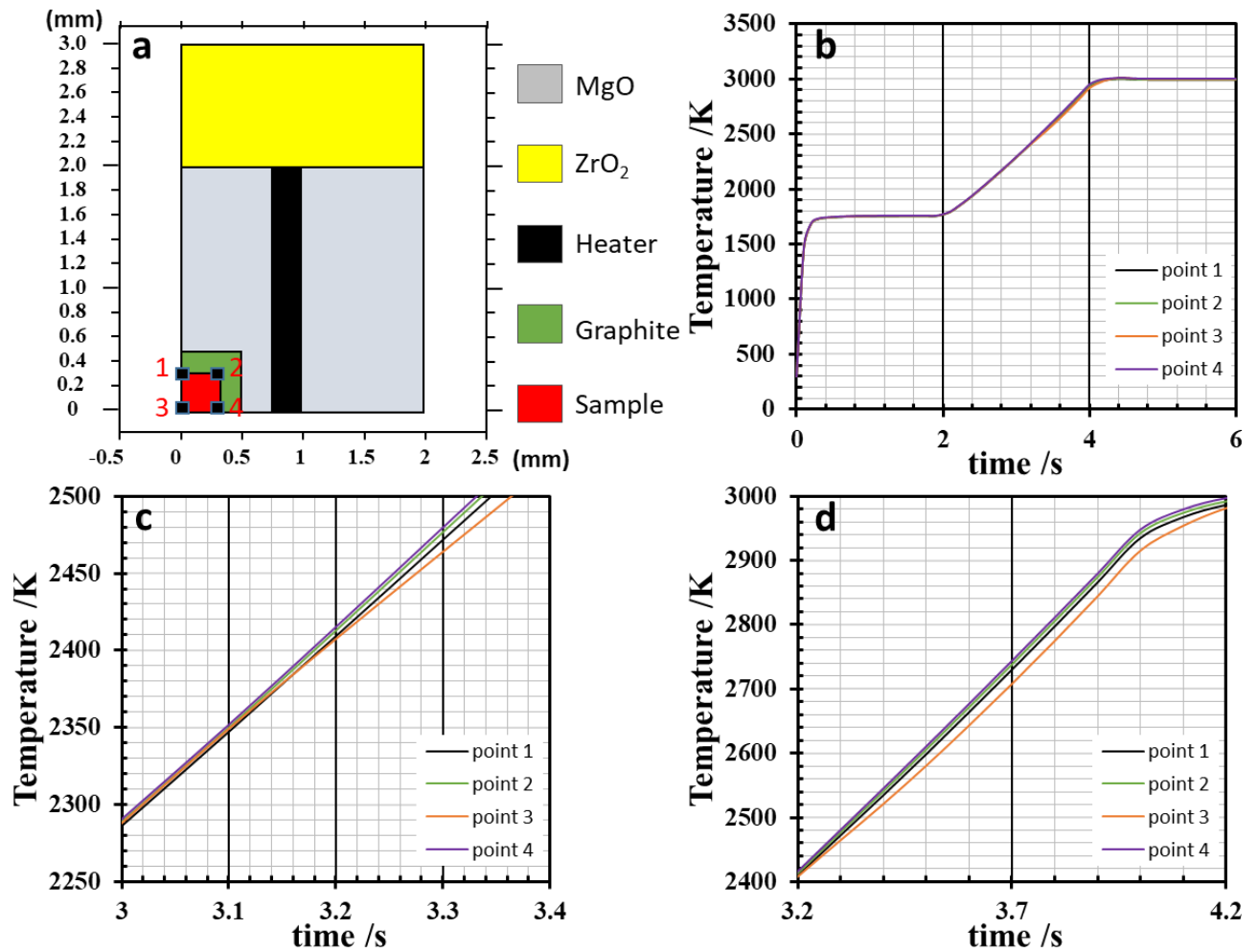


Figure 2.2 Fast heating simulation by means of FEM. a, Cross section of the present axisymmetric 2D model. Owing to the symmetries, a quarter part of cell assembly is used for the FEM analysis. The pupil squares show the observation points in the fast heating. **b**, The resulted temperature log simulated on COMSOL™. **c**, magnified plot around 2400 K. **d**, magnified plot after sample melted. Temperatures at position 1, 2 and 4 are ~20-40 K higher than that at position 3.

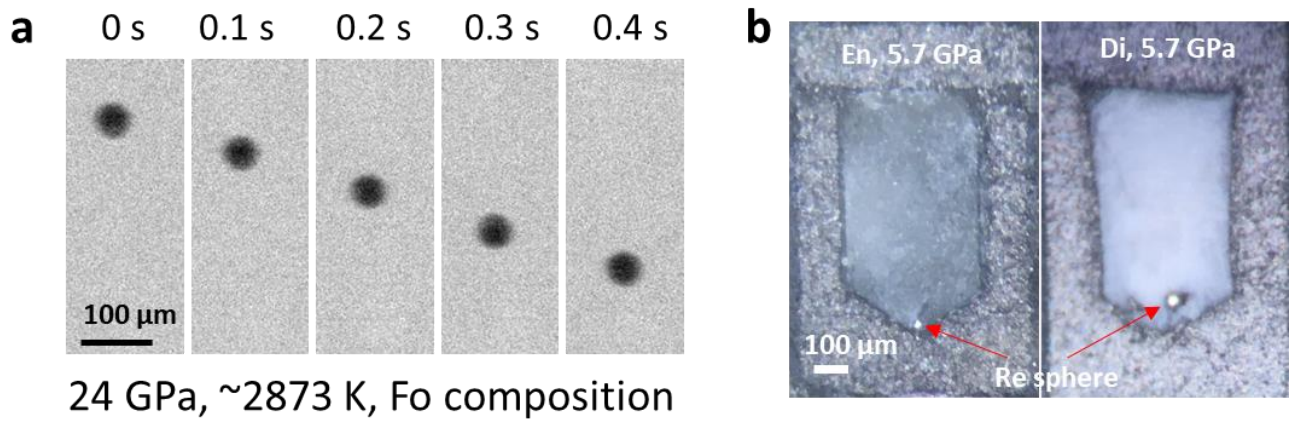


Figure 2.3 Example falling path of Re sphere (a) and recovered sample (b). **a,** Sequential radiographic images of sinking Re sphere in Run MA 24. The images of the Re sphere (67.4 μm diameter at vacuum condition) were clearly recognized. **b,** Microscope images of the recovered samples. It shows that samples were completely sealed in the capsule, and the Re spheres kept original round shape.

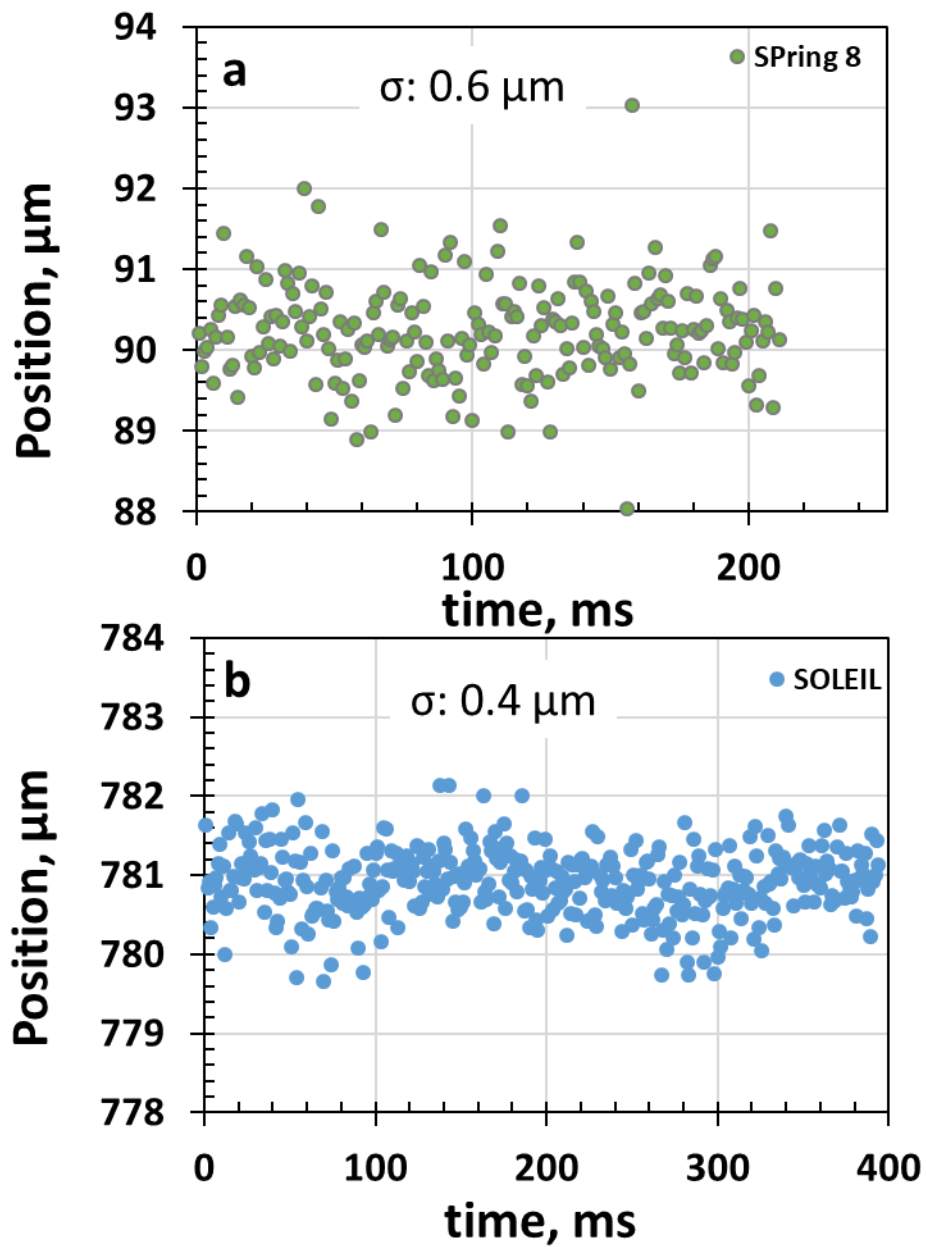


Figure 2.4 Error of sphere determination for experiments at SPring-8 (a) and SOLEIL (b). σ : 1 standard deviation.

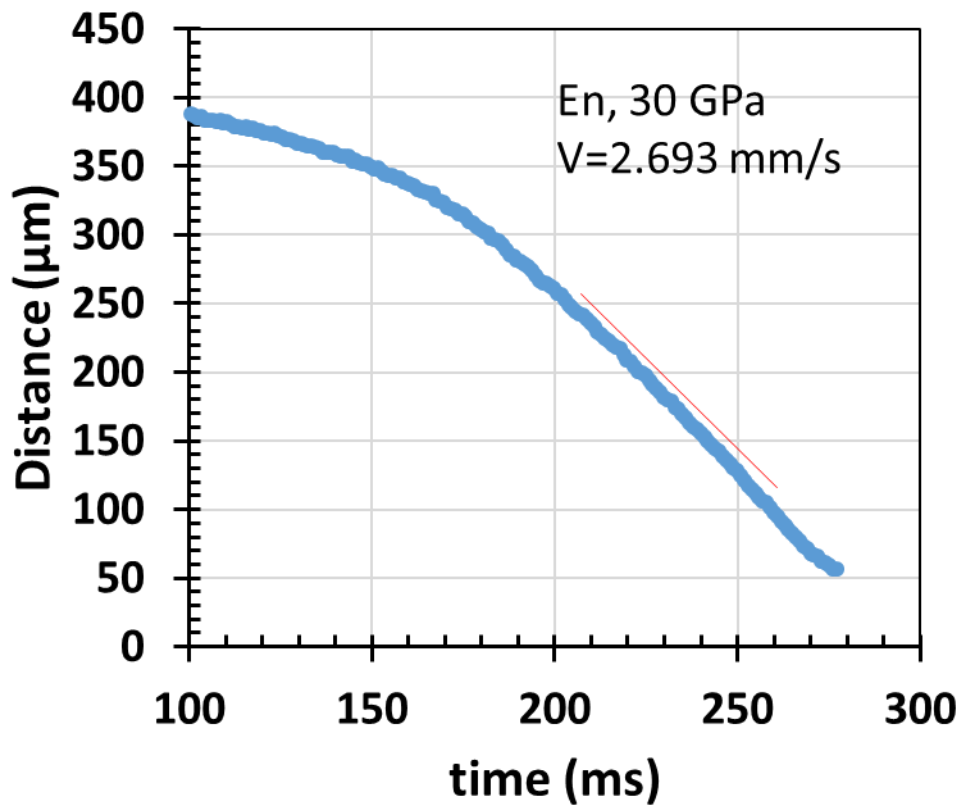


Figure 2.5 An example (run S3220) of distance-time diagram. Blue symbol indicates the sphere position from the top boundary of anvil gap in each image. Red line marks the slope (velocity) when sphere reaches terminal velocity. Sphere position were fitted by Gaussian fitting.

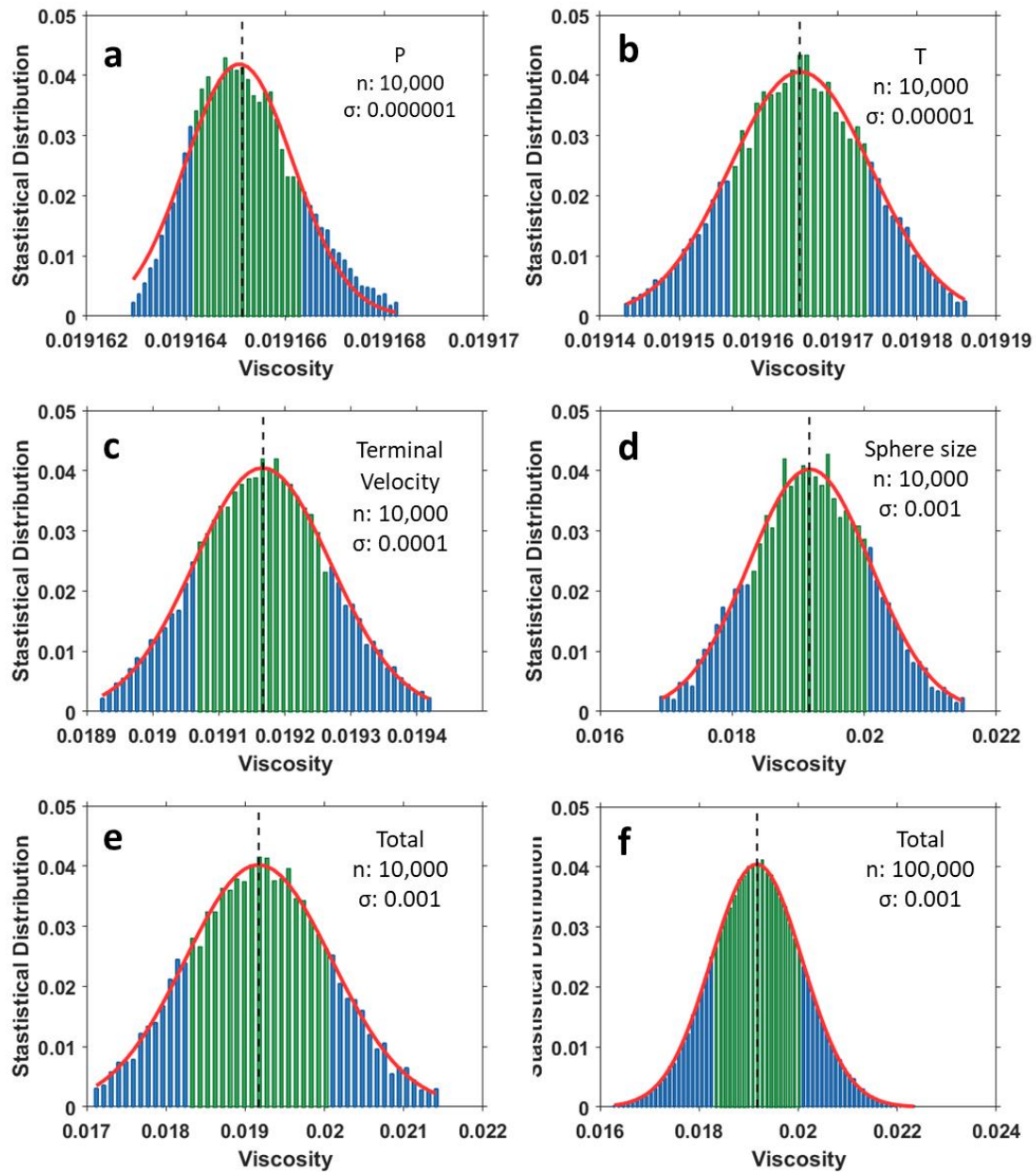


Figure 2.6 Results of Monte-Carlo simulation for error propagation. a, b, c, and d: viscosity error contributed from error of pressure, temperature, terminal velocity, and sphere size, respectively. **e and f:** total error from all the five factors calculated with 10,000 and 100,000 sampling number, respectively. **n:** sampling number; **σ :** 1 standard deviation. **Red curve:** Gaussian fitting curve.

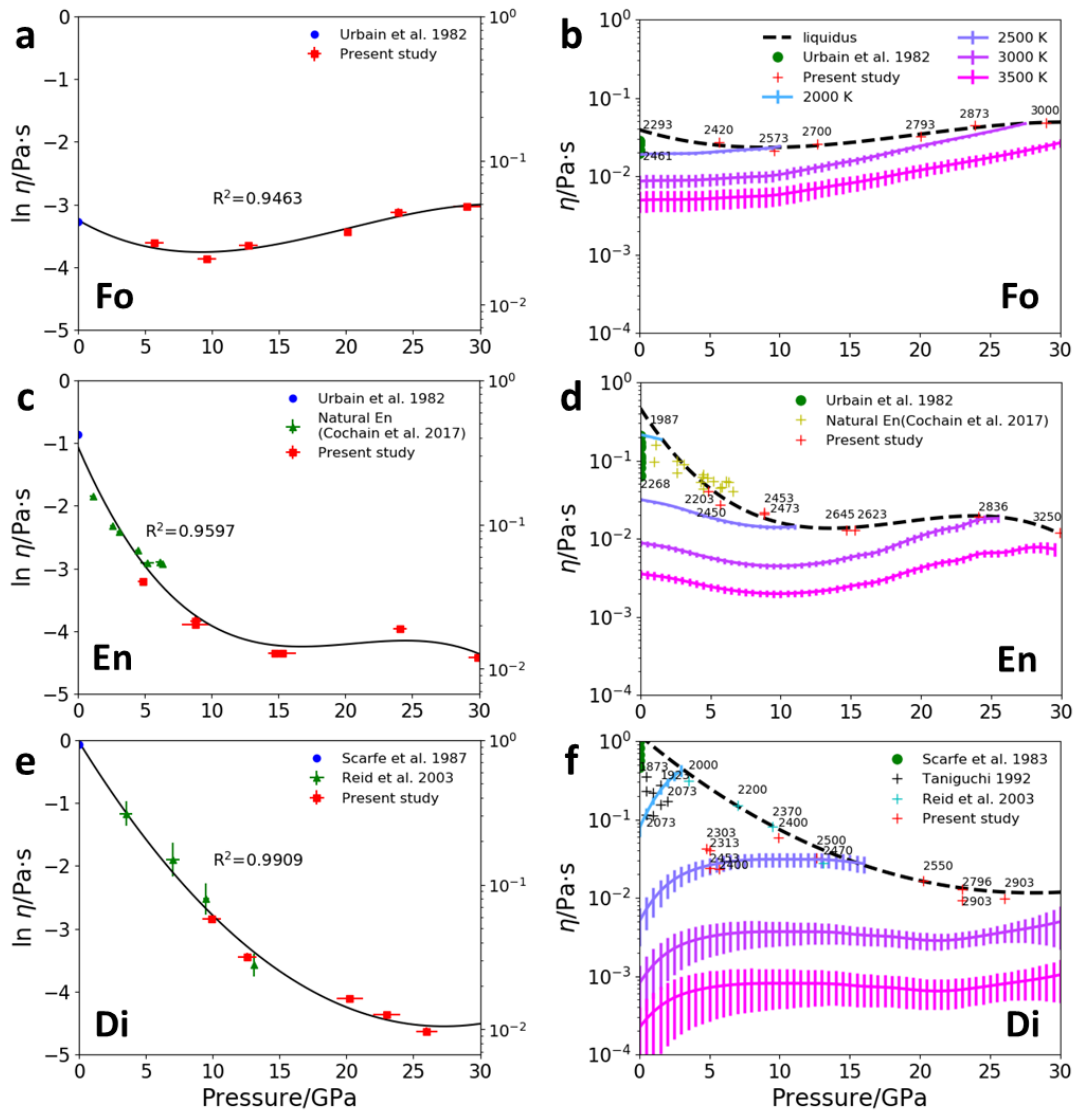


Figure 2.7 Viscosities of silicate melts along the liquidus as a function of pressure (left column) and extrapolation above liquidus (right column). **a,b**, Fo; **c, d**, En; **e,f**, Di. **Left column (a, c, e)**: viscosities along the liquidus. The symbols indicate experimental data. The error bar of viscosity measured in this study is within the symbols. Cubic polynomials were used to fit the data of Fo, En and Di until 30 GPa. **Right column (b, d, f)**: viscosities as a function of pressure and temperature. The symbols indicate the experimental data. Numbers annotated near symbols refer to corresponding temperature. Solid lines indicate viscosities along isotherms, calculated using equation (1). The error bar (1 standard deviation) shows the error propagated from the uncertainty of fitted parameters. Dashed line: viscosities along liquidus.

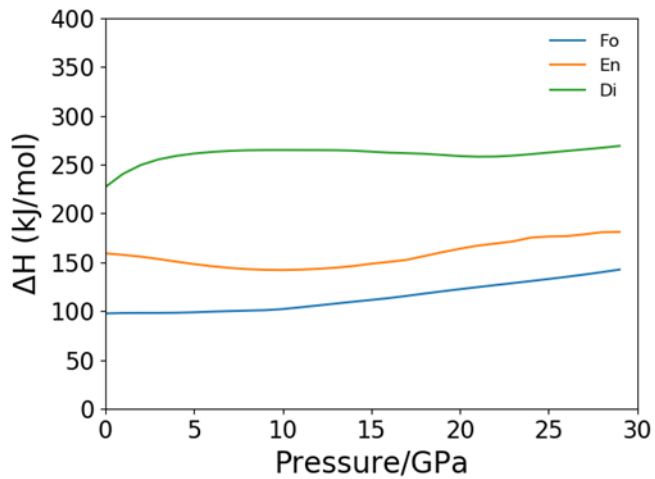


Figure 2.8 Activation enthalpy of silicate melts viscosity as a function of pressure.

Blue, yellow and green lines indicate activation enthalpy of Fo, En and Di melt viscosity, respectively. Fo melt (~100 kJ/mol) has the lowest activation enthalpy of viscosity, which is increasing with pressure. Di melt (~250 kJ/mol) has the highest activation enthalpy of viscosity. It increases with pressure until ~5 GPa, then decrease with pressure until ~22 GPa and increase with pressure again until 30 GPa. The activation enthalpy of En melt is ~150 kJ/mol, which first decreases with pressure and then increases with pressure.

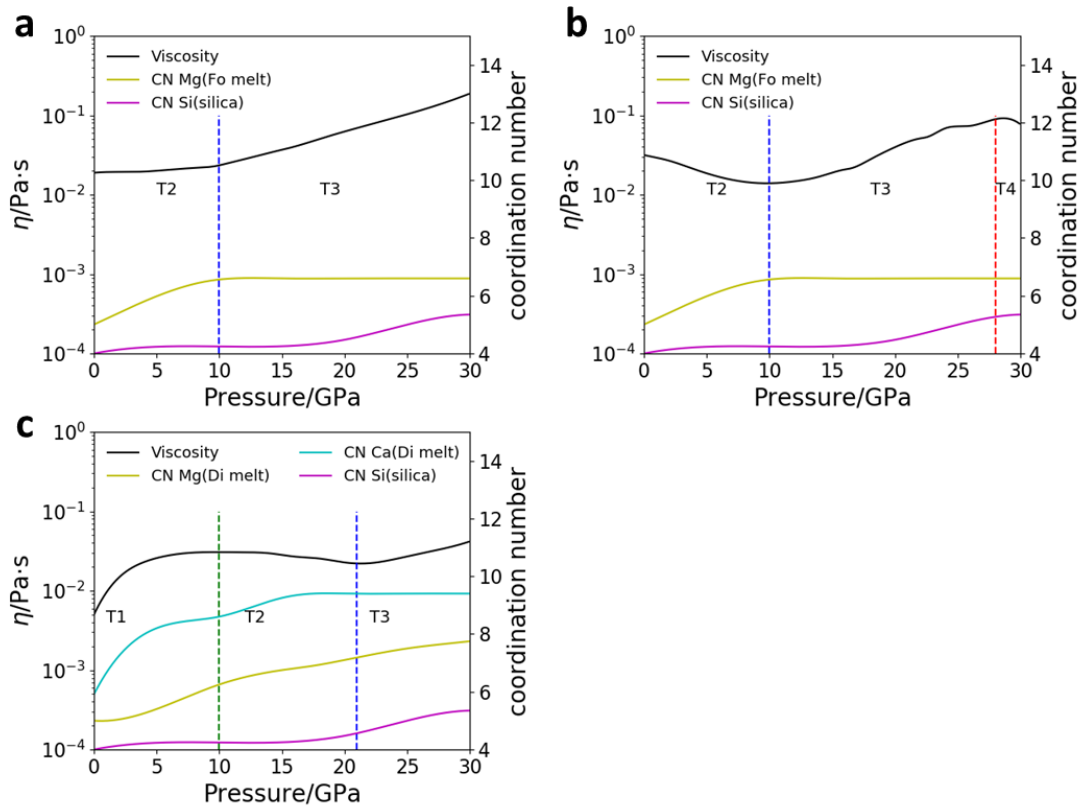


Figure 2.9 Densification mechanisms of Fo (a), En (b) and Di (c) melts under high pressure. Black solid curve: viscosity curve of Fo, En and Di melts at 2500 K. Yellow solid lines: pressure dependence of Mg coordination number (CN) in Fo melt³⁴ (a,b) or Di melt³⁵ (c). Magenta solid lines: pressure dependence of Si CN in silica; average value in ref 36-37. Cyan solid lines: pressure dependence of Ca CN in Di melt³⁵. Green dashed line marks the boundary between T1 and T2. Blue dashed line marks the boundary between T2 and T3. Red dashed line marks the boundary between T3 and T4.

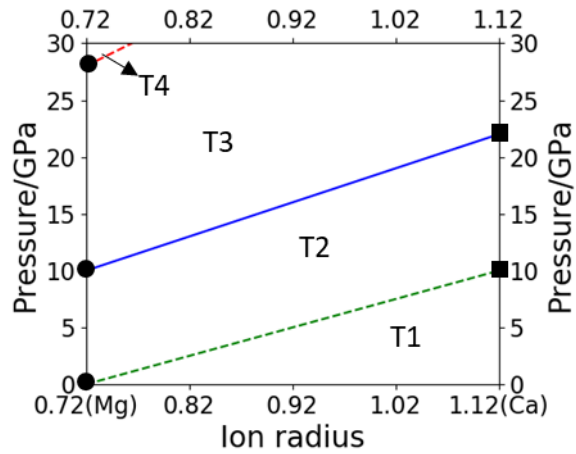


Figure 2.10 Effect of modifier ion radius on densification mechanism of silicate melts under high pressure. Green dashed line: the boundary between T1 and T2. Blue solid line: the boundary between T2 and T3. Red dashed line: the boundary between T3 and T4, assuming the same slope with the boundary between T2 and T3. Black filled circle: pressures of T1, T2, T3 and T4 boundaries for En melt. We assume the pressure (≤ 0) of T1 and T2 boundary for En melt is 0. Black filled square: pressures of T1, T2 and T3 boundary for Di melt.

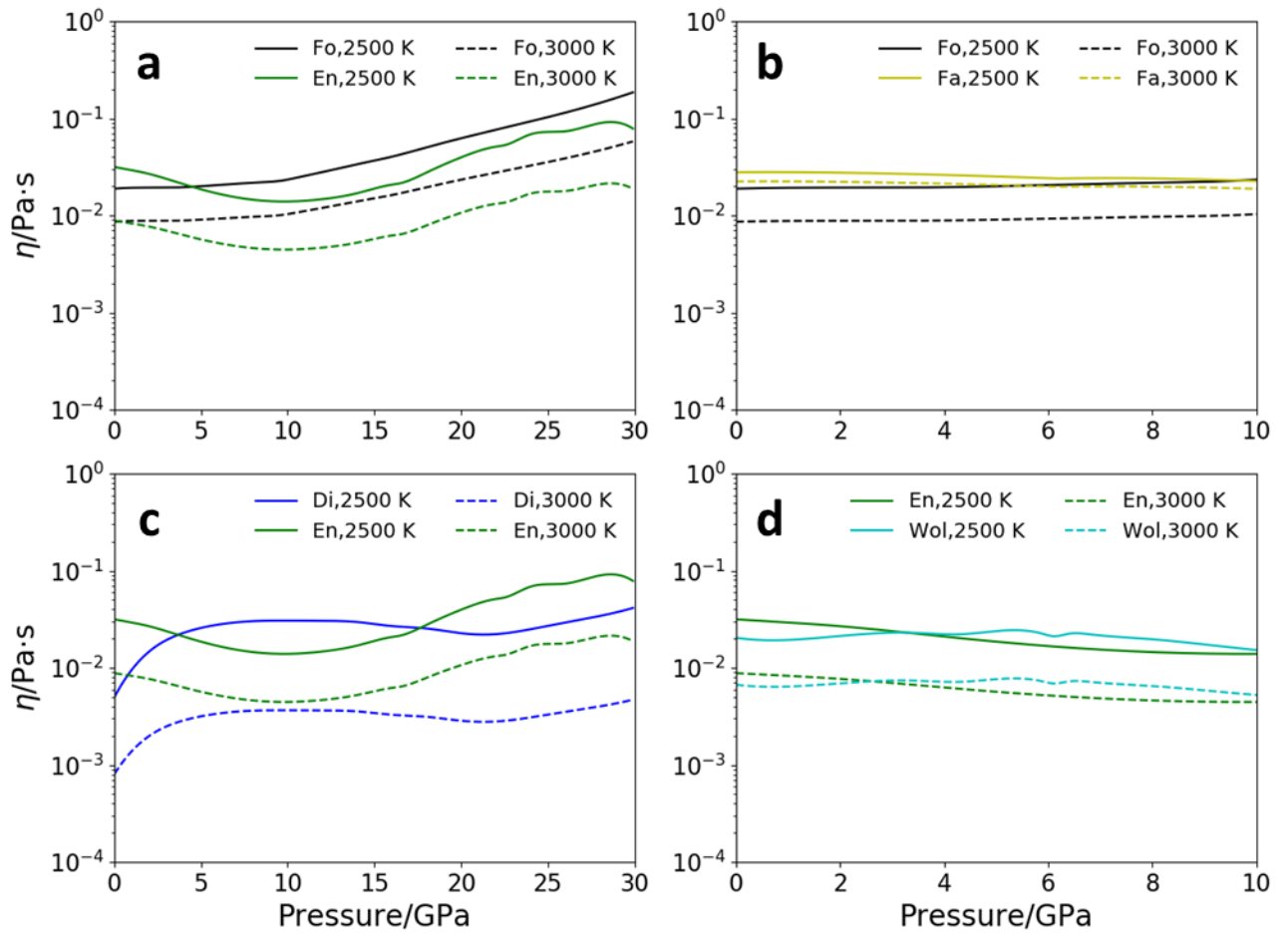


Figure 2.11 Composition effects on viscosity of silicate melts at 2500 and 3000 K.

a: comparison of viscosities between Fo and En melt up to 30 GPa. **b:** comparison of viscosities between Fo and Fa melt up to 10 GPa. **c:** comparison of viscosities between En and Di melt up to 30 GPa. **d:** comparison of viscosities between En and Wol (CaSiO₃) melt up to 10 GPa.

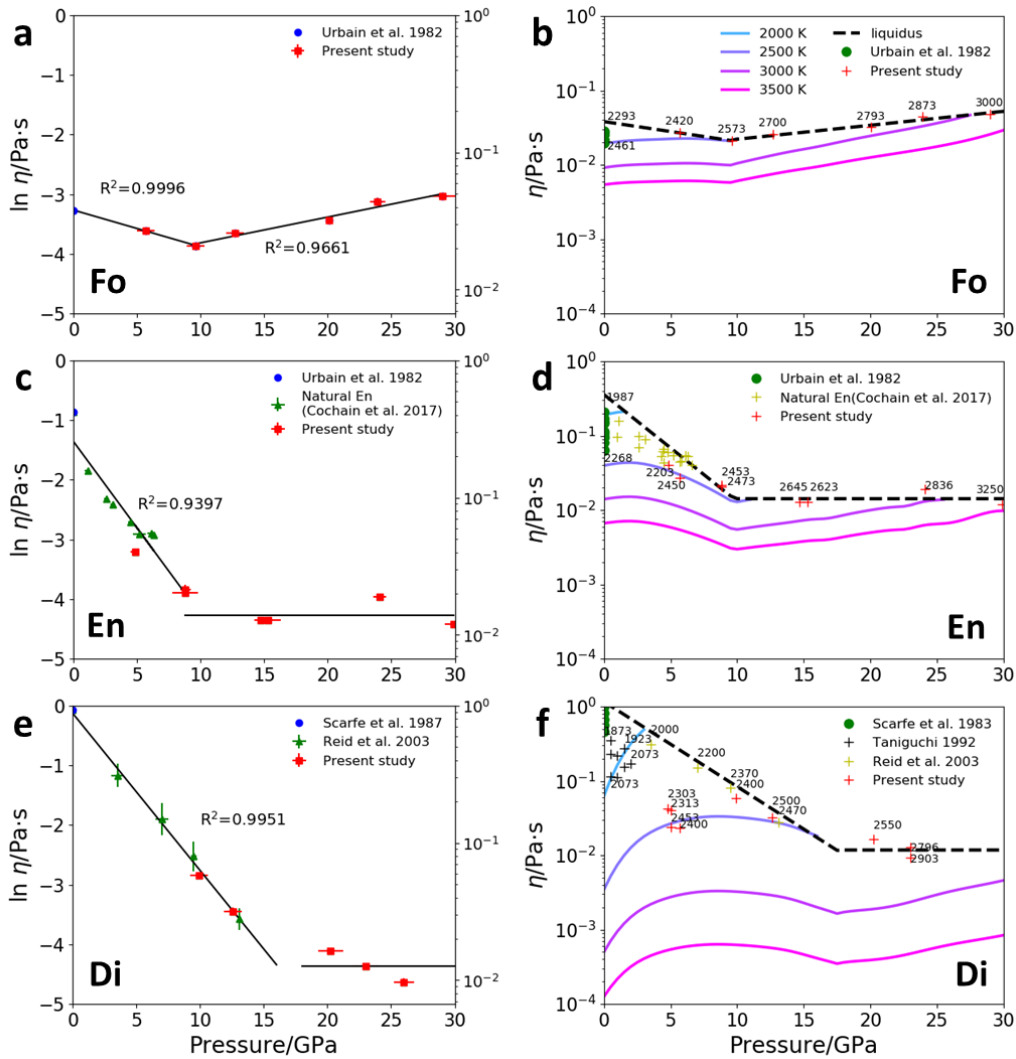


Figure 2.12 viscosities of silicate melts along the liquidus as a function of pressure (left column) and extrapolation to other temperatures (right column). **a,b**, Fo; **c, d**, En; **e,f**, Di. **Left column (a, c, e)**: viscosities of silicate melts along the liquidus. The symbols indicate experimental data. The error bar of viscosity measured in this study is within the symbols. Two linear sections were used to fit the data of Fo, En and Di until 30 GPa. **Right column (b, d, f)**: viscosities of silicate melts as a function of pressure and temperature. The symbols indicate the experimental data. Numbers annotated near symbols refer to corresponding temperature. Solid lines indicate viscosities along isotherms, calculated using equation (1). Dashed line indicates viscosities along liquidus.

**Part 3. Chemical evolution of magma ocean
inferred from silicate melt viscosity**

3.1 Abstract

It is believed that the early Earth experienced several episodes of magma ocean (MO); among them, the MO just after the giant Moon-forming impact is the major one. Solidification of the MO, which formed just after the Giant Impact (GI), obviously set the initial condition of the Earth's heterogeneity over 4.5 Gy to the present. The long-term debate on fractional or equilibrium solidification of MO is mainly due to the poorly constrained physical parameters, in particular viscosity of MO. Here, we estimate the viscosity of MO using linear combination of four endmembers (Fo, En, Di and An composition). The estimated viscosity of MO is 0.01-0.1 Pa.s along the liquidus up to ~900 km. Based on the viscosity, the diffusivity of MO is estimated to be 10^{-9} - 10^{-8} m²/s using the Eyring equation. The viscosity and diffusivity of MO suggest that the crystal size is larger than that can be suspended by the MO convection, thus, implicating a fractional solidification of MO. Based on the mass balance calculation of major elements (of MO, residual MO and fractionated minerals) and trace elements partitioning (between fractional lower mantle minerals and residual MO), the fractionation assemblage of lower mantle minerals is bridgmanite, CaSiO₃ perovskite and ferropericlasite (mass ratio: 93:3:4) in literature. The corresponding total fractionation amount is ~13wt%. Assuming a perfect fractional solidification, the depth of fractionated MO and the thickness of a lower mantle cumulate layer is estimated to be ~880 km and ~220km, respectively. After fully solidification, the cumulate layer is bridgmanite-enriched, neutral (or slightly denser ~2 ‰) and stronger (viscosity contrast ~30), compared with pyrolite mantle. Based on the mantle dynamic simulation⁶³, such bridgmanite enriched ancient mantle material may be transferred to the depth of ~1000 km by later mantle convection and still persists there at present day.

Therefore, the cumulate may contribute to the viscosity peak at 800-1400 km of present solid Earth.

3.2 Introduction

3.2.1 Magma ocean and its classification

Magma ocean (MO) can be formed by the blanketing effect of atmosphere or giant accretionary impacts^{eg.1-3}. The giant accretionary impacts theories suggest that multiple MO may exist before reaching solidity in a planet. The processes of MO formation and solidification, strongly influence the earliest compositional differentiation and volatile content of the terrestrial planets, and they set the initial condition for later cooling and the onset of thermally driven mantle convection and plate tectonics^{4 references there in}.

As shown in Table 3.1, there are several types of MO and different criteria is adopted to classify MOs³. Based on the life time, MOs are classified as ‘sustained MO’ and ‘transient MO’. The life time of MO is related with the formation process of MO. If the growing terrestrial planet has a thick blanketing atmosphere, the surface temperature of the planet is kept above the melting temperature and a MO formed on the planet^{eg. 5}. Such MO is sustained during accretion of the planet and classified as a ‘sustained MO’. On the contrary, a deep MO may form by a single large impact^{eg.2}. Such MO would cool and solidify within a relatively short period, if there is no atmospheric blanketing effect.

To distinguish the high-pressure minerals’ effect on the differentiation of MO, MOs can also be classified as ‘deep MO’ and ‘shallow MO’^{eg. 3}. Depth of a deep MO reaches bridgmanite stable pressure. While that of shallow MO doesn’t reach bridgmanite stable pressure.

The dynamics of MO is highly affected by the viscosity of MO. Based on the rheological transition, MOs can be classified as ‘soft MO’ and ‘hard MO’^{eg. 3}. The viscosity of MO changes from a liquid-like behavior to a solid-like behavior at the crystal fraction of ~60%. The MO contains low crystal fraction (<60 %), thus has low viscosity comparable with that of melt, is regarded as ‘soft MO’. The MO contains high crystal fraction (>60 %), on the contrary, is regarded as ‘hard MO’ with viscosity comparable with that of crystals.

3.2.2 The major MO on Earth and its solidification

It is believed that the early Earth experienced several episodes of magma-ocean, with a major one just after the giant Moon-forming impact. Such a global MO definitely affects the thermal and chemical evolution since then. In this background, we focus on this major MO in the early Earth.

Numerical investigations showed that the largest impactors could have reached the Mars size at the latest stages of Earth accretion^{eg. 6-11}. A giant impact between a Mars size impactor and proto-Earth can explain the origin of the Moon, its composition, and the angular momentum of the Earth-Moon system^{eg. 12-15}. A major MO on Earth was probably formed during the Moon-forming giant impact¹³. The depth of MO reaches lower mantle or even the core-mantle boundary due to the huge kinetic energy of giant impact and the gravitational energy release of the redistribution of thermal heterogeneities in the mantle and core formation^{eg.2,16}. Such a MO should be a transient, deep and soft MO. Chemical differentiation of primordial mantle occurs through gravitational segregation of melt and solid in the MO³. The solidification of MO obviously set the initial condition of the Earth’s heterogeneity over 4.5 Gy to the present⁴ and references there in.

3.2.3 Fractional versus equilibrium solidification of MO

Whether fractional or equilibrium crystallization occur in a MO is fundamental to understand the chemical evolution of MO. In fractional solidification, mineral grains settle from MO and the residual liquid composition evolves with the removal of each package of solidified material. In equilibrium solidification, mineral grains suspended in the flow of MO and thus the equilibrium with liquid component were maintained throughout solidification. Fractional and equilibrium solidification thus lead to entirely different predictions on mineral assemblage, major element and trace-element compositions of residual MO. However, the problem of fractional versus equilibrium solidification has not been yet settled.

There are two complementary methods to help us understanding the solidification process of MO. One is to combine the measured geochemical data of present mantle and partition coefficient of elements between minerals and silicate melts^{eg.17-22}. This method is based on the idea that the fractionation of MO would undoubtedly have left some record in geochemical data. The other is to simulate the physical process of MO solidification by fluid dynamic simulations^{eg.16,23-29}. This method can physically constrain what kind of solidification processes can occur in MO.

3.2.4 Geochemical constrains and Ca-silicate perovskite paradox

The primary upper mantle (PUM) is assumed to be evolved from a MO with bulk silicate earth (BSE) composition by fractionation of lower mantle minerals. The major and trace elements in the primitive upper mantle have been well documented^{eg.30}. The mass balance calculation of major elements and elements partitioning calculation of trace elements can be used to constrain whether fractional or equilibrium solidification

occurs in MO^{eg. 17-22,31-37}.

The mass balance among BSE, PUM and lower mantle minerals (Mg-silicate perovskite (Mg-Pv), ferripericlasite (Fp) and Ca-silicate perovskite (Ca-Pv)), can be expressed:

$$\text{BSE} = a_1 * \text{PUM} + a_2 * \text{Mg-Pv} + a_3 * \text{Ca-Pv} + a_4 * \text{Fp} \dots \dots \dots 4.1$$

$$a_1 + a_2 + a_3 + a_4 = 1 \dots \dots \dots 4.2$$

where a_1 , a_2 , a_3 and a_4 are fitted parameters by least square regression. Several solutions were obtained (Table 3.2).

Further constraint on the solutions can be conducted by the elements partition calculation of trace elements between lower mantle minerals and residual MO (PUM). The elements concentration in residual MO can be calculated using equation:

$$C_i^l = C_i^{0,l} f^{\bar{D}_i - 1} \dots \dots \dots 4.3$$

where C_i^l is the concentration of element i in residual liquid, $C_i^{0,l}$ the concentration of element i in parent liquid, f the weight proportion of residual liquid, \bar{D}_i is the bulk partition coefficient. The initial value of refractory lithophile element (RLE) ratios in MO is assumed to be chondritic. If an element ratio is chondritic in primitive upper mantle, the maximum amount of lower mantle mineral fractionation must not drive RLE ratios outside of the uncertainty of the chondritic value. Combined constraints from major and trace elements, the best solution is (0.8697, 0.121, 0.0044, 0.0049) for (a_1 , a_2 , a_3 , a_4). Thus, the fractionation amount of lower mantle minerals is ~13wt%.

The majority of elements (e.g. REEs) that are incompatible in bridgmanite are actually compatible in Ca-Pv¹⁸. Thus, a fractionation of small amounts of Ca-Pv is critical to maintain the near chondritic RLE ratios in the geochemical model of fractional solidification. However, experimental results showed that Ca-Pv is solidus phase instead of liquidus phase^{e.g. 34-37}. It is difficult to crystallize Ca-Pv in a MO with

BSE composition before the solidification fraction reaches 13 wt%. Because Ca-Pv is the first liquidus phase for peridotite with enriched bulk CaO^{e.g. 18, 36,37}. There is no substantial fractionation of bridgmanite in MO or there is an omitted process which can produce CaO-enriched melt. Therefore, the solidification type is still under debate due to the unclear solidification processes in MO.

3.2.5 Physical simulation model and unconstrained parameters

Physical simulation method requires the understanding of physical processes during MO solidification and well determination of related physical properties such as viscosity and heat flux of MO. Vigorous convection, crystallization, crystal settling and entrainment are the basic processes occurred during MO solidification. The solidification type of MO depends on the competition between crystal settling and entrainment^{16,23,27-29}. The maximum size of crystal that the MO convection can suspend is defined as critical diameter. If the crystal size in MO is larger than the critical diameter, fractional solidification will occur. On the contrary, equilibrium solidification will occur if the crystal size in MO is smaller than the critical diameter. The boundary between fractional and equilibrium solidification is where crystal size equals critical diameter.

The critical diameter can be described using the following equation²⁷⁻²⁹:

$$d_c = \left(\frac{18\alpha\eta_l FAL}{f_\phi g c_p \Delta\rho^2 \Phi V} \right)^{1/2} \dots\dots\dots 4.4$$

Where L , A , V is the depth, surface and volume of MO, respectively; α is thermal expansion coefficient; F is heat flux of MO; η_l is melt viscosity; $\Delta\rho$ is the density contrast between melt and crystal in MO; Φ is crystal fraction; f_ϕ is a hindered settling function, which describes the phenomenon that the average settling velocity of particles are less than their Stokes velocity. The hindered settling function can be described as³⁸:

$$f_{\Phi} = \frac{(1-\Phi)^2}{(1+\Phi^3)\exp(\frac{5\Phi}{3(1-\Phi)})} \dots\dots\dots 4.5$$

If the crystal fraction in the magma ocean varies from 0 to the maximum packing fraction $\Phi = 0.6$ then the average crystal fraction is about 30%. Using the values of parameters in Table 3.3, we can obtain^{24,28 29}:

$$d_c \approx 0.001 \left(\frac{\eta_l}{0.1 \text{ Pa s}}\right)^{1/2} \left(\frac{F}{10^6 \text{ W m}^{-2}}\right)^{1/2} \dots\dots\dots 4.6$$

The crystal size in MO affects by two processes: nucleation and Ostwald ripening. The crystal size in MO is mainly controlled by nucleation and Ostwald ripening does not increase the crystal size substantially^{24,28 29}. The nucleation size can be estimated using the following equation^{24,28 29}:

$$d_{nucl} = 0.001 \left(\frac{\sigma_{app}}{0.02 \text{ J m}^{-2}}\right) \left(\frac{D}{10^{-9} \text{ m}^2 \text{ s}^{-1}}\right)^{1/2} \left(\frac{\mu_0}{10 \text{ m s}^{-1}}\right)^{-1/2} \dots\dots\dots 4.7$$

where σ_{app} is the apparent surface energy; D is the diffusion coefficient. μ_0 is the convection velocity. μ_0 can be calculated from the heat flux using following equation^{24,28 29}:

$$\mu_0 = 14 \left(\frac{\alpha g F}{\rho c_p \Omega}\right)^{1/2} \dots\dots\dots 4.8$$

Where ρ is density of melt, Ω is the angular velocity. Replacing equation 4.8 and related parameters in table 3.3 in equation 4.7, we can obtain:

$$d_{nucl} = 0.001 \left(\frac{D}{10^{-9} \text{ m}^2 \text{ s}^{-1}}\right)^{1/2} \left(\frac{F}{10^6 \text{ W m}^{-2}}\right)^{-1/4} \dots\dots\dots 4.9$$

D is related with melt viscosity through the Eyring equation³⁹:

$$D = \frac{kT}{\lambda \eta} \dots\dots\dots 4.10$$

T the absolute temperature, k the Boltzmann constant, λ the ionic translation distance, for which the diameter of oxygen ion (2.8Å) was used. Thus, the viscosity of MO is one of main parameters, which controls the solidification of MO.

Based on equation 4.6 and 4.9, we can derive the expression for the boundary

between equilibrium and fractional solidification:

$$\eta_b = 0.1 \left(\frac{D}{10^{-9} \text{ m}^2 \text{ s}^{-1}} \right) \left(\frac{F_b}{10^6 \text{ W m}^{-2}} \right)^{-3/2} \dots\dots\dots 4.11$$

Where η_b and F_b is viscosity and heat flux on the boundary, respectively. MO with smaller viscosity and smaller heat flux than those at the boundary, is fractional solidification. On the contrary, MO with larger viscosity and larger heat flux than those at the boundary, is equilibrium solidification.

3.2.6 Life time of MO

The life time of MO is defined as the melt fraction drops below 50% at all mantle depths in mantle. The numerical simulation of MO convection suggests that the life time of MO is mainly controlled by viscosity of MO and can be described as^{29, 40}:

$$t(\text{Myr}) = 0.018\eta^{3/7} \dots\dots\dots 4.12$$

MO with higher viscosity has longer life time.

3.2.7 Aim of this study

As discussed above, the MO, which formed just after the Giant Impact (GP), has great influence on the thermal and chemical evolution of Earth. The solidification of MO obviously set the initial condition of the Earth's heterogeneity over 4.5 Gy to the present. The viscosity of MO is one of the main parameters that control the convection dynamics and solidification of MO. The purpose of this study is to constrain the solidification type of MO by estimating the viscosity and diffusivity of MO and rebuilt the model on chemical evolution of MO by integrating the geochemical and high pressure experimental data.

3.3 Method

Bottinga and Weill (1972)⁴¹ proposed that logarithm viscosity can be satisfactory expressed as a linear function of composition over a restricted composition interval (for example SiO₂ mole content from 30-50 %) at superliquidus conditions. This model was experimentally confirmed for the Ca-Mg exchange in molten garnets and pyroxenes⁴² and for Na-K exchange in alkali-silicates⁴³. This model can be demonstrated within the framework of the Adam-Gibbs theory as shown in equation (10)-(12)⁴⁴.

$$\eta = A_e \exp\left(\frac{B_e}{T S^{conf}}\right) \dots \dots \dots 4.13$$

$$S^{conf}(T) = \sum x_i S_i^{conf}(T) + S_{mix} \dots \dots \dots 4.14$$

$$S_{mix} = -nR \sum x_i \ln x_i \dots \dots \dots 4.15$$

n the number of entities exchanged per formula unit. A very strong nonlinear variation of the viscosity occurs just above the glass transition due to the mixing entropy, with a minimum of orders of magnitude. When the temperature increases, the depth of this minimum decreases and logarithmic viscosity is eventually a linear function of composition at temperatures near or higher than liquidus. We can conclude that arithmetic average of logarithmic endmember viscosity is the upper limit of complex system at temperatures near or higher than liquidus.

Composition of KLB-1 is a natural analog to represent the bulk mantle composition. The upper limit of melt viscosity with KLB-1 composition was calculated using four endmembers (Fo, En, Di and An composition), with following equation:

$$\ln(\eta_{KLB-1}) = f_{Fo} * \eta_{Fo} + f_{En} * \eta_{En} + f_{Di} * \eta_{Di} + f_{An} * \eta_{An} \dots \dots \dots 4.16$$

where *f* is molar content ratio of endmember (shown in Table 3.4). To reflect the composition effect, we also calculate the bulk viscosity with different combination of endmembers. The diffusivity of MO was calculated based on the viscosity of MO using

Eyring equation.

3.4 Results and discussions

3.4.1 Viscosity and diffusivity of MO along adiabats

Figure 3.1a shows the liquidus and adiabats in MO. We calculated melt viscosity of MO along adiabats and liquidus using a linear combination of logarithm viscosity of Fo, En, Di and anorthite (An, $\text{CaAl}_2\text{Si}_2\text{O}_8$) melt. The viscosity of Fo, En, Di composition are based on the present result. Viscosity of An composition is from first principle calculation results⁴⁶. Since the combination of linear functions ignores the effect of mixing entropy, the calculated results shown in Figure 3.1b give the upper limit of viscosity of MO. The estimated viscosity of MO is between 0.01 and 0.1 Pa.s up to ~900 km depth. The viscosity of MO first decreases and then increases downward with a minimum at ~300 km depth. The corresponding diffusivity of MO is estimated to be 10^{-9} to 10^{-8} m^2/s based on viscosity of MO using equation 4.10 (Figure 3.1c). The diffusivity of MO first increases and then decreases downward with a maximum at ~300 km depth.

Figure 3.2 compares viscosity of different melt compositions along isotherms. Because KLB-1 is composed of ~90 mol.% of Fo and En, the melt viscosity is mainly controlled by Fo and En. Melt, with higher content of En endmember, has lower viscosity at high pressures (>5 GPa) and temperatures (> liquidus of KLB-1). But the variation of viscosity is small. The viscosity range of MO is between 0.01 and 0.1 Pa.s up to ~900 km depth, no matter the MO composition is peridotite or bridgmanite.

3.4.2 Fractional solidification of MO and its life time

Heat flux of MO and melt viscosity (or diffusivity) control the critical diameter and crystal size in MO, thus controlling the solidification type of MO. The controversy on fractional or equilibrium crystallization in MO is definitely caused by uncertainty of these parameters²⁹.

According to equations 4.6 and 4.9, we recalculated crystal and critical diameter for MO with our newly estimated viscosity and diffusivity of MO (shown in Figure 3.3a). The heat flux of MO is estimated to be as high as 10^6 Wm^{-2} before a thick atmosphere develops, and 10^2 Wm^{-2} after a significant atmosphere develops⁴⁸⁻⁵⁰. Because the viscosity and diffusivity of MO is in the range of 0.01-0.1 Pa.s and 10^{-9} to $10^{-8} \text{ m}^2/\text{s}$, respectively. The crystal size in MO is concluded to be larger than the critical diameter regardless the thickness of blanket atmosphere. Thus, it clearly suggests the fractional solidification of MO.

As Figure 3.3b shows the boundary between fractional and equilibrium solidification as a function of viscosity and heat flux. The viscosity and heat flux range of MO obviously belongs to the fractional solidification range. In the heat flux region of MO, roughly we can say fractional solidification occurs if viscosity of MO is smaller than 0.1 Pa.s; equilibrium solidification occurs if viscosity of MO is larger than 0.1 Pa.s. Both classic and first-principle molecular dynamic simulation shows that viscosity of silicate melts along adiabats increase with depth at deep lower mantle depth^{e.g.46,51-56}. The viscosity of MO at depth higher than ~1000 km is likely to be larger than 0.1 Pa.s. Thus, equilibrium solidification should occur at depth beneath 1000 km. If the depth of MO reaches core-mantle boundary and solidification of MO starts from bottom, equilibrium solidification will first occur and continues until the solidification front reach ~1000 km depth. Then, fractional solidification will occur. If the depth of MO is

smaller than 1000 km, fractional solidification will occur from the beginning.

As discussed in the introduction part, the numerical simulation of MO convection suggests that the life time of MO can be scale as $\eta^{3/7}$ ^{29, 40}. Using equation 4.12, the life time of MO is calculated to be ~1-6 thousand years for a viscosity range of 0.01 to 0.1 Pa.s. Thus, the life time of MO is very short, if ignoring the atmosphere blanket effect.

3.4.3 Process of fractional solidification in MO

Our viscosity data suggests a fractional solidification of MO. However, the fractional solidification model is doubted by the Ca-Pv paradox, which is caused by the unclear processes occurred in MO. Here, we propose a likely process, which can form a Ca-enriched peridotite melt at the bottom of MO and solve the Ca-Pv paradox (Figure 3.4). We divide the solidification process into two-stage. In the first stage, the solidification front (the intersection between adiabatic curve and liquidus) was in lower mantle (depth >660 km) (Figure 3.4a); bridgmanite, the first liquidus phase, sunk to the bottom of MO (Figure 3.4c). In the second stage, the crystallization front reached depth shallower than 660 km (Figure 3.4b); the solidification end, defined as the rheology transition depth (60% crystal), is still in the lower mantle. At depth shallower than 660 km, majorite became the first liquidus phase and started crystallization. Assisted by the downward flow, majorite fast sunk across the 660 km depth, transform to bridgmanite, accumulate and dissolve at the bottom of MO, forming a Ca-enriched layer (Figure 3.4d). In the Ca-enriched layer, Ca-Pv started settling together with bridgmanite. The allowed amount of Ca-Pv fractionation is related with the fractionation interval (the depth between solidification front and end). If the fractionation interval is larger, the process of majorite settling across the 660 km could continue longer period, thus larger

amount of Ca-Pv could be fractionated. Since the adiabat flattens at the region between liquidus and solidus due to latent heating, the fractionation interval can spread over 180 km³. It is likely to provide enough fraction of Ca-Pv in this scenario.

3.4.4 Thickness, composition and fate of cumulate

As discussed in the introduction, the fractionation amount of lower mantle minerals is ~13wt%. Assuming a perfect fractional solidification, the composition of the cumulate layer was composed of 60% fractionated crystals (bridgmanite and Ca-Pv) and 40% residual melt (pyrolite composition). Thus, we can build up equation 4.17 through the amount of cumulate.

$$\frac{4}{3}\pi(R_e^3 - (R_e - L)^3) * 0.13 = \frac{4}{3}\pi((R_e - 660)^3 - (R_e - L)^3)/0.6 \dots \dots 4.17$$

Where R_e is the Earth diameter, L is the initial depth of MO. The initial depth of MO is calculated to be ~880 km. The final thickness of corresponding accumulate layer ($L - 660$ km), thus, is ~220 km.

After its fully solidified, the accumulate layer is composed of ~85.6% Mg-Pv, 4.4 % Ca-Pv, and 10% Fp. The cumulate has similar mineral composition with CI chondrite lower mantle, but it is more bridgmanite-enriched compared with pyrolite upper mantle (Table 3.5). It is slightly denser (<2 ‰) than the pyrolite mantle. Since the viscosity contrast between bridgmanite and Fp is large (~1000 times)⁶², the rheology of the lower mantle materials depends strongly on the geometry of a weaker phase, Fp. The geometry of Fp is highly related with its volume content. Because the cumulate layer has ~9 vol. % less Fp than pyrolite mantle, it can be much stronger (~30 times) than the pyrolite mantle. Such bridgmanite-enriched ancient layer may be strong enough to prevent efficient mantle mixing, transfer to the depth of about 1000-2200 km, become diffused and persist there to the present day (Figure 3.5 b)⁶³. The bridgmanite-

enriched cumulate layer may be the origin of the viscosity peak at ~1400 km of present solid Earth (Figure 3.5 c)⁶⁴. Another possible fate of cumulate layer is that it finally homogenized with the surrounding mantle during the later mantle convection.

3.5 Conclusions

The viscosity and diffusivity of MO were estimated to be 0.01-0.1 Pa.s and 10^{-9} - 10^{-8} m²/s up to ~900 km. The estimated viscosity and diffusivity suggests a fractional solidification of MO up to ~900 km.

Constrained by the RLE ratios, a combined fractionation of Ca-Pv and bridgmanite allows a maximum amount of lower mantle mineral fractionation (~13 wt.%). Crystallized majorite possibly sunk across the 660km depth, transformed to bridgmanite, dissolved at the bottom of MO and forms a Ca-enriched layer. The Ca-Pv can crystallize in this Ca-enriched layer. The depth where MO started fractional solidification is ~880km. The thickness of cumulate is ~220km. After fully solidification, the cumulate layer, enriched with bridgmanite, is slightly denser and can be much stronger than pyrolite mantle. Due to its strength, the cumulate layer may overcome the later mantle convection mixing and transferred to the depth of about 1000-2200 km of present Earth.

References in Part III

1. Abe, Y., & Matsui, T. (1985). The formation of an impact-generated H₂O atmosphere and its implications for the early thermal history of the Earth. *Journal of Geophysical Research: Solid Earth*, 90(S02), C545-C559.
2. Tonks, W. B., & Melosh, H. J. (1993). Magma ocean formation due to giant impacts. *Journal of Geophysical Research: Planets*, 98(E3), 5319-5333.
3. Abe, Y. (1997). Thermal and chemical evolution of the terrestrial magma ocean. *Physics of the Earth and Planetary Interiors*, 100(1-4), 27-39.
4. Elkins-Tanton, L. T. (2012). Magma oceans in the inner solar system. *Annual Review of Earth and Planetary Sciences*, 40, 113-139.
5. Matsui, T., & Abe, Y. (1986). Evolution of an impact-induced atmosphere and magma ocean on the accreting Earth. *Nature*, 319(6051), 303.
6. Safronov, V. S. (1964). The primary inhomogeneities of the earth's mantle. *Tectonophysics*, 1(3), 217-221.
7. Safronov, V. S. (1978). The heating of the Earth during its formation. *Icarus*, 33(1), 3-12.
8. Wetherill, G. W. (1975). Radiometric chronology of the early solar system. *Annual Review of Nuclear Science*, 25(1), 283-328.
9. Wetherill, G. W. (1985). Occurrence of giant impacts during the growth of the terrestrial planets. *Science*, 228(4701), 877-879.
10. Wetherill, G. W. (1990). Formation of the Earth. *Annual Review of Earth and Planetary Sciences*, 18(1), 205-256.
11. Weidenschilling, S. J., Spaute, D., Davis, D. R., Marzari, F., & Ohtsuki, K.

- (1997). Accretional evolution of a planetesimal swarm. *Icarus*, 128(2), 429-455.
12. Benz, W., Slattery, W. L., & Cameron, A. G. W. (1986). The origin of the Moon and the single-impact hypothesis I. *Icarus*, 66(3), 515-535.
 13. Canup, R. M. (2004). Simulations of a late lunar-forming impact. *Icarus*, 168(2), 433-456.
 14. Newsom, H. E., & Taylor, S. R. (1989). Geochemical implications of the formation of the Moon by a single giant impact. *Nature*, 338(6210), 29.
 15. Stevenson, D. J. (1987). Origin of the moon-The collision hypothesis. *Annual review of earth and planetary sciences*, 15(1), 271-315.
 16. Tonks, W. B., & Melosh, H. J. (1990). The physics of crystal settling and suspension in a turbulent magma ocean. *Origin of the Earth*, 151-174.
 17. Kato, T., Ringwood, A. E., & Irifune, T. (1988). Experimental determination of element partitioning between silicate perovskites, garnets and liquids: constraints on early differentiation of the mantle. *Earth and Planetary Science Letters*, 89(1), 123-145.
 18. Corgne, A., & Wood, B. J. (2002). CaSiO_3 and CaTiO_3 perovskite-melt partitioning of trace elements: Implications for gross mantle differentiation. *Geophysical Research Letters*, 29(19), 39-1.
 19. Corgne, A., Liebske, C., Wood, B. J., Rubie, D. C., & Frost, D. J. (2005). Silicate perovskite-melt partitioning of trace elements and geochemical signature of a deep perovskitic reservoir. *Geochimica et Cosmochimica Acta*, 69(2), 485-496.
 20. Liebske, C., Corgne, A., Frost, D. J., Rubie, D. C., & Wood, B. J. (2005). Compositional effects on element partitioning between Mg-silicate perovskite and silicate melts. *Contributions to Mineralogy and Petrology*, 149(1), 113-128.

21. Walter, M. J., Nakamura, E., Trønnes, R. G., & Frost, D. J. (2004). Experimental constraints on crystallization differentiation in a deep magma ocean. *Geochimica et Cosmochimica Acta*, 68(20), 4267-4284.
22. Walter, M. J., & Trønnes, R. G. (2004). Early earth differentiation. *Earth and Planetary Science Letters*, 225(3-4), 253-269.
23. MARTIN, D., & NOKES, R. (1989). A fluid-dynamical study of crystal settling in convecting magmas. *Journal of Petrology*, 30(6), 1471-1500.
24. Solomatov, V. S., & Stevenson, D. J. (1993). Kinetics of crystal growth in a terrestrial magma ocean. *Journal of Geophysical Research: Planets*, 98(E3), 5407–18.
25. Solomatov, V. S., & Stevenson, D. J. (1993). Nonfractional crystallization of a terrestrial magma ocean. *Journal of Geophysical Research: Planets*, 98(E3), 5391-5406.
26. Solomatov, V. S., & Stevenson, D. J. (1993). Suspension in convective layers and style of differentiation of a terrestrial magma ocean. *Journal of Geophysical Research: Planets*, 98(E3), 5375-5390.
27. Solomatov, V. S., Olson, P., & Stevenson, D. J. (1993). Entrainment from a bed of particles by thermal convection. *Earth and planetary science letters*, 120(3-4), 387-393.
28. Solomatov VS. 2000. Fluid dynamics of a terrestrial magma ocean. In *Origin of the Earth and Moon*, ed. RM Canup, K Righter, pp. 323–38. Tucson: Univ. Ariz. Press.
29. Solomatov VS. 2007. Magma oceans and primordial mantle differentiation. In *Treatise on Geophysics, Vol. 9: Evolution of the Earth*, ed. DJ Stevenson, pp. 91–119. Amsterdam: Elsevier.

30. McDonough, W. F., & Sun, S. S. (1995). The composition of the Earth. *Chemical geology*, 120(3-4), 223-253.
31. Ringwood A. E. (1990). Earliest history of the Earth-Moon system. In: Newsom N E, Jones J H (eds.) *Origin of the Earth*. Oxford University Press, New York, pp. 101-134.
32. McFarlane E. A., & Drake M J (1990) Element partitioning and the early thermal history of the Earth. In: Newsom N E, Jones J H (eds.) *Origin of the Earth*. Oxford University Press, New York, pp. 135-150.
33. McFarlane, E. A., Drake, M. J., & Rubie, D. C. (1994). Element partitioning between Mg-perovskite, magnesiowuestite, and silicate melt at conditions of the Earth's mantle. *Geochimica et Cosmochimica Acta*, 58(23), 5161-5172.
34. Ito, E., & Takahashi, E. (1987). Melting of peridotite at uppermost lower-mantle conditions. *Nature*, 328(6130), 514.
35. Ito, E., Kubo, A., Katsura, T., & Walter, M. J. (2004). Melting experiments of mantle materials under lower mantle conditions with implications for magma ocean differentiation. *Physics of the Earth and Planetary Interiors*, 143, 397-406.
36. Hirose, K., Shimizu, N., van Westrenen, W., & Fei, Y. (2004). Trace element partitioning in Earth's lower mantle and implications for geochemical consequences of partial melting at the core-mantle boundary. *Physics of the Earth and Planetary Interiors*, 146(1-2), 249-260.
37. Trønnes, R. G., & Frost, D. J. (2002). Peridotite melting and mineral-melt partitioning of major and minor elements at 22-24.5 GPa. *Earth and Planetary Science Letters*, 197(1-2), 117-131.
38. Davis, R. H., & Acrivos, A. (1985). Sedimentation of noncolloidal particles at low Reynolds numbers. *Annual Review of Fluid Mechanics*, 17(1), 91-118.

39. Eyring, H. (1936). Viscosity, plasticity, and diffusion as examples of absolute reaction rates. *The Journal of chemical physics*, 4(4), 283-291.
40. Monteux, J., Andraut, D., & Samuel, H. (2016). On the cooling of a deep terrestrial magma ocean. *Earth and Planetary Science Letters*, 448, 140-149.
41. Bottinga, Y., & Weill, D. F. (1972). The viscosity of magmatic silicate liquids; a model calculation. *American Journal of Science*, 272(5), 438-475.
42. Neuville, D. R., & Richet, P. (1991). Viscosity and mixing in molten (Ca, Mg) pyroxenes and garnets. *Geochimica et Cosmochimica Acta*, 55(4), 1011-1019.
43. Richet, P. (1984). Viscosity and configurational entropy of silicate melts. *Geochimica et Cosmochimica Acta*, 48(3), 471-483.
44. Richet, P., & Bottinga, Y. (1995). Composition dependence of the viscosity. In: *Rheology and configurational entropy of silicate melts. Reviews in Mineralogy and Geochemistry*, 32(1), 81-82.
45. Zhang, J., & Herzberg, C. (1994). Melting experiments on anhydrous peridotite KLB-1 from 5.0 to 22.5 GPa. *Journal of Geophysical Research: Solid Earth*, 99(B9), 17729-17742.
46. Karki, B. B., Bohara, B., & Stixrude, L. (2011). First-principles study of diffusion and viscosity of anorthite ($\text{CaAl}_2\text{Si}_2\text{O}_8$) liquid at high pressure. *American Mineralogist*, 96(5-6), 744-751.
47. Liebske, C., Schmickler, B., Terasaki, H., Poe, B. T., Suzuki, A., Funakoshi, K. I., ... & Rubie, D. C. (2005). Viscosity of peridotite liquid up to 13 GPa: Implications for magma ocean viscosities. *Earth and Planetary Science Letters*, 240(3-4), 589-604.

48. Abe, Y., & Matsui, T. (1986). Early evolution of the Earth: Accretion, atmosphere formation, and thermal history. *Journal of Geophysical Research: Solid Earth*, 91(B13), E291-E302.
49. Zahnle, K. J., Kasting, J. F., & Pollack, J. B. (1988). Evolution of a steam atmosphere during Earth's accretion. *Icarus*, 74(1), 62-97.
50. Elkins-Tanton, L. T. (2008). Linked magma ocean solidification and atmospheric growth for Earth and Mars. *Earth and Planetary Science Letters*, 271(1-4), 181-191.
51. Wasserman, E. A., Yuen, D. A., & Rustad, J. R. (1993). Molecular dynamics study of the transport properties of perovskite melts under high temperature and pressure conditions. *Earth and planetary science letters*, 114(2-3), 373-384.
52. Lacks, D. J., Rear, D. B., & Van Orman, J. A. (2007). Molecular dynamics investigation of viscosity, chemical diffusivities and partial molar volumes of liquids along the MgO–SiO₂ join as functions of pressure. *Geochimica et Cosmochimica Acta*, 71(5), 1312-1323.
53. Nevins, D., Spera, F. J., & Ghiorso, M. S. (2009). Shear viscosity and diffusion in liquid MgSiO₃: Transport properties and implications for terrestrial planet magma oceans. *American Mineralogist*, 94(7), 975-980.
54. Karki, B. B., & Stixrude, L. P. (2010). Viscosity of MgSiO₃ liquid at Earth's mantle conditions: Implications for an early magma ocean. *Science*, 328(5979), 740-742.
55. de Koker, N. P., Stixrude, L., & Karki, B. B. (2008). Thermodynamics, structure, dynamics, and freezing of Mg₂SiO₄ liquid at high pressure. *Geochimica et Cosmochimica Acta*, 72(5), 1427-1441.

56. Ghosh, D. B., & Karki, B. B. (2011). Diffusion and viscosity of Mg_2SiO_4 liquid at high pressure from first-principles simulations. *Geochimica et Cosmochimica Acta*, 75(16), 4591-4600.
57. Verma, A. K., & Karki, B. B. (2012). First-principles study of self-diffusion and viscous flow in diopside ($\text{CaMgSi}_2\text{O}_6$) liquid. *American Mineralogist*, 97(11-12), 2049-2055.
58. Yamazaki, D., & Karato, S. I. (2001). Some mineral physics constraints on the rheology and geothermal structure of Earth's lower mantle. *American Mineralogist*, 86(4), 385-391.
59. Ballmer, M. D., Houser, C., Hernlund, J. W., Wentzcovitch, R. M., & Hirose, K. (2017). Persistence of strong silica-enriched domains in the Earth's lower mantle. *Nature Geoscience*, 10(3), 236.
60. Rudolph, M. L., Lekić, V., & Lithgow-Bertelloni, C. (2015). Viscosity jump in Earth's mid-mantle. *Science*, 350(6266), 1349-1352.

Tables

Table 3.1 Classification of MO.

Criteria	Classification	Characteristics
Life time	Sustained MO	long life time, usually formed by blanketing effect of atmosphere
	Transient MO	short life time, usually formed by giant impact
Depth of MO	Deep MO	Depth of MO reaches bridgmanite stable pressure
	Shallow MO	Depth of MO doesn't reach bridgmanite stable pressure
Viscosity of MO	Soft MO	Crystal fraction less than 60%, liquid-like viscosity
	Hard MO	Crystal fraction higher than 60%, solid-like viscosity

Table 3.2 Fitted parameters of mass balance calculation.

Solutions	a₁	a₂	a₃	a₄	SSD*	Ref.
S1	0.894	0.102	0.002	0	0.33	Ref.35
S2	0.9194	0.069	0.0116	0	0.46	Ref. 22
S3	0.8648	0.1218	0.0077	0.0057	0.21	Ref. 22
S4	0.8697	0.121	0.0044	0.0049	0.08	Ref. 22

* SSD: sum of squared deviation

Table 3.3. Values of physical parameters for a magma ocean in the early stages of crystallization according to ref. 29.

Density, ρ (kg m⁻³)	4000
Crystal/melt density contrast, $\Delta\rho$ (kg m⁻³)	550
Thermal expansion, α (K⁻¹)	5×10^{-5}
Thermal capacity, c_p (J kg⁻¹ K⁻¹)	10^3
Gravity, g (m s⁻²)	10
Depth of MO, L (m)	0.9×10^6
Earth radius, R_{Earth} (m)	6.37×10^6
Apparent surface energy, σ_{app} (J m⁻²)	0.02
Angular velocity, Ω (s⁻¹)	10^{-4}

Table 3.4. Endmember contents of various melts (Molar ratio in percent).

Endmembers	Fo	En	Di	An
KLB-1	63.26	32.7	0.7	3.32
Case1*	65.9	34.1	0	0
Case2	50	50	0	0

* The composition of Case1 has the same Fo/En ratio with KLB-1.

Table 3.5 Mineral proportions (vol.%) and density of pyrolite, BSE, CI chondrite and accumulate layer.

Composition (vol.%)	Ca-perovskite	Bridgmanite (Mg: 0.9, Fe:0.1)	Fp (Mg:0.8, Fe: 0.2)	ρ, kg/m³ * (23 GPa, 1990K)
Pyrolite	6.4	74.6	19	4263
BSE	7	76	17	4266
CI chondrite	6	83	11	4271
Accumulate layer	4.4	85.6	10	4268

*Density of systems were calculated using EOSes of Ca-perovskite⁵⁸, bridgmanite⁵⁹, MgO⁶⁰ and FeO

⁶¹. The Fe effect on density of bridgmanite was ignored.

Figures

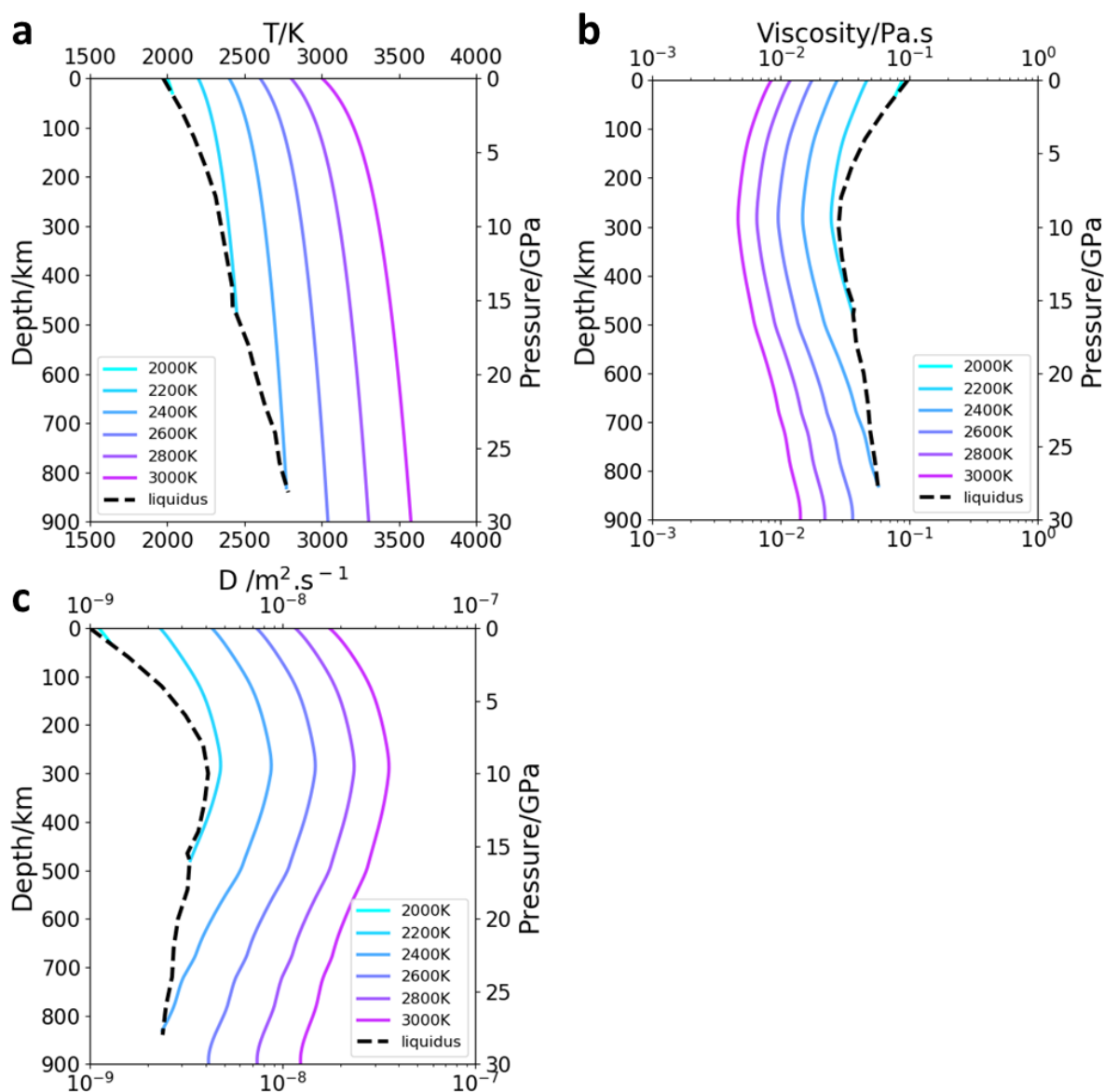


Figure 3.1 Viscosities and diffusivity of MO along adiabats. Numbers in the legend refer to the potential temperature. **a**, adiabats in MO. The adiabatic temperature profiles⁴⁰ are calculated by numerical integration of adiabatic temperature gradient. **b**, viscosities in MO along adiabats. **c**, diffusivities in MO along adiabats. The liquidus temperature refers to Ref. 45.

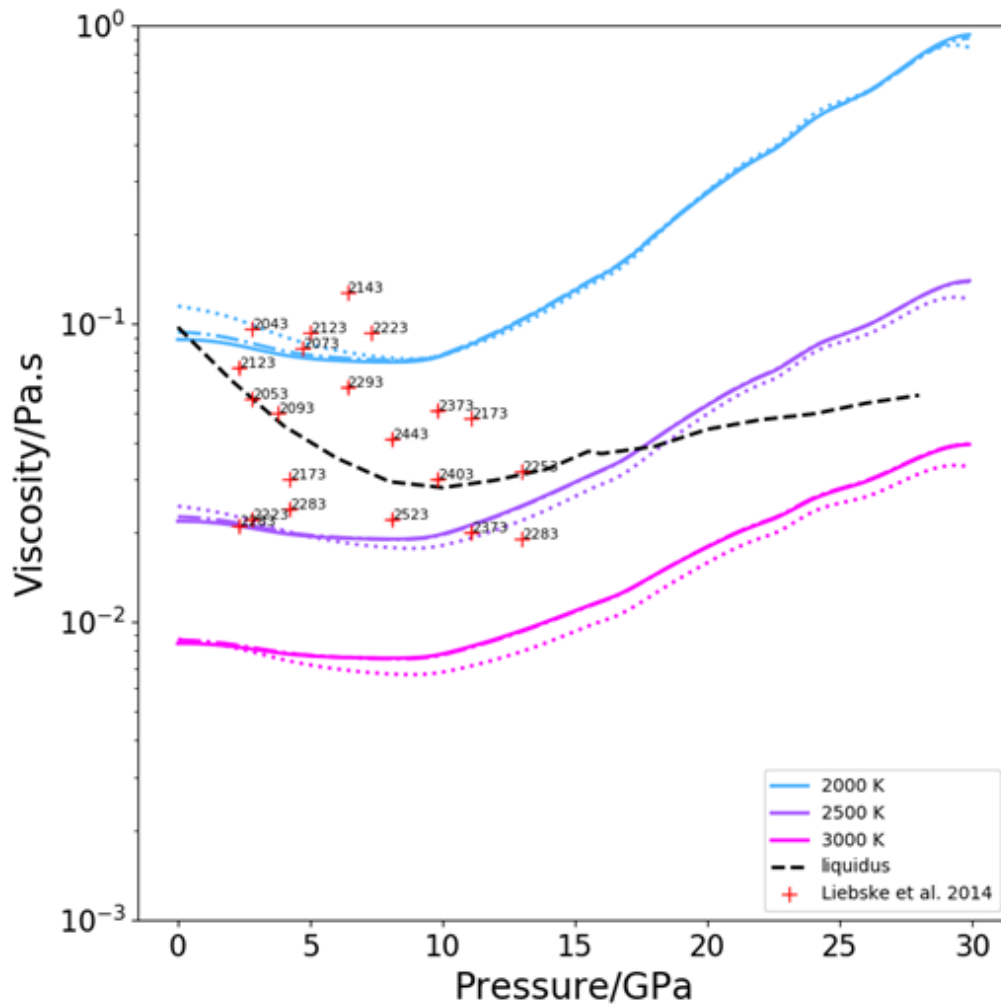


Figure 3.2 Viscosities of different melt compositions along isotherms. Solid line: viscosity of KLB-1. Dashed dotted line: case 1 in Table 3.4. Dotted line: case 2 in Table 3.4. The solid line and dash dotted line almost overlap because the viscosities of KLB-1 and case 1 are similar. Black dashed line indicates viscosity of KLB-1 composition along liquidus⁴⁵. Red cross symbol indicates experimental data of BSE⁴⁷. Although the experimental data in ref. 47 looks scattering with a few factors, the average seems to be consistent with the estimated result along liquidus.

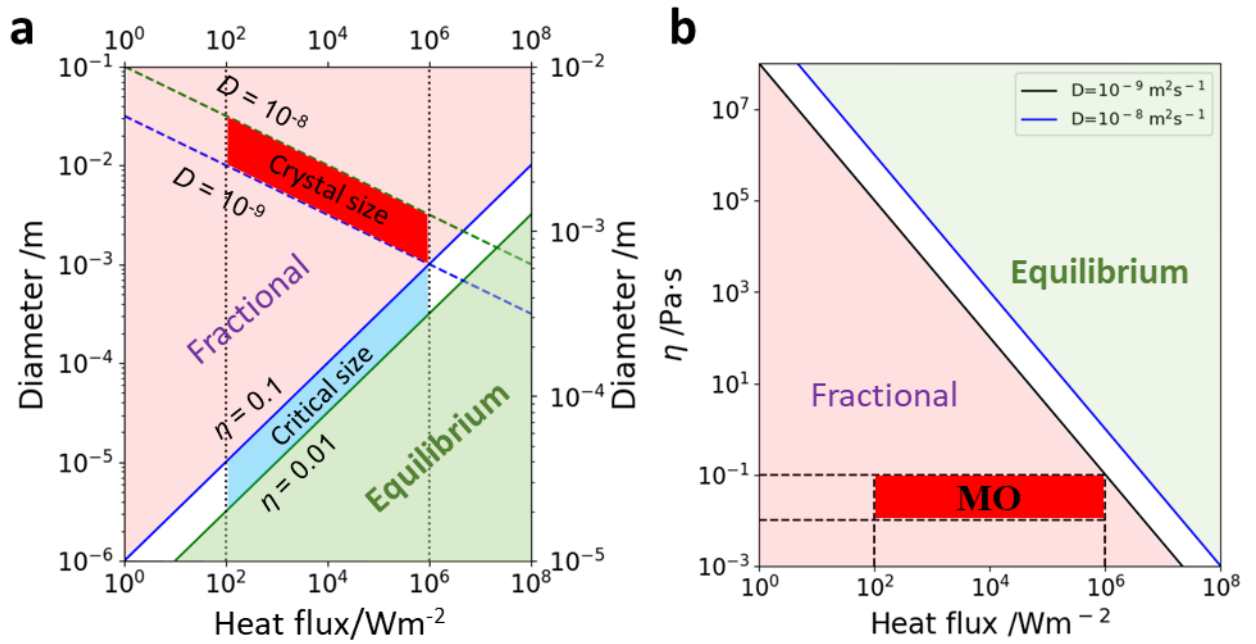


Figure 3.3 Diagrams for fractional and equilibrium solidification boundary. a, Diagram for comparing critical diameter and precipitated crystal size in MO. Solid lines: estimated critical diameter using equation 4.6. Dashed lines: estimated crystal size using equation 4.9. Dotted lines: maximum and minimum of heat flux in MO. Light red color region: the area where crystal size is larger than critical size, or, fractional solidification is expected. Light green region: the area where crystal size is smaller than critical size, or, equilibrium solidification is expected. Red color region: the range of crystal size in MO. Blue region: the range of critical diameter in MO. **b,** Boundary between fractional and equilibrium solidification as a function of heat flux and viscosity. Solid lines: boundary between fractional and equilibrium solidification using equation 4.11. Light red region: fractional solidification region. Light green region: equilibrium solidification region. Dark red region: viscosity and heat flux range of MO.

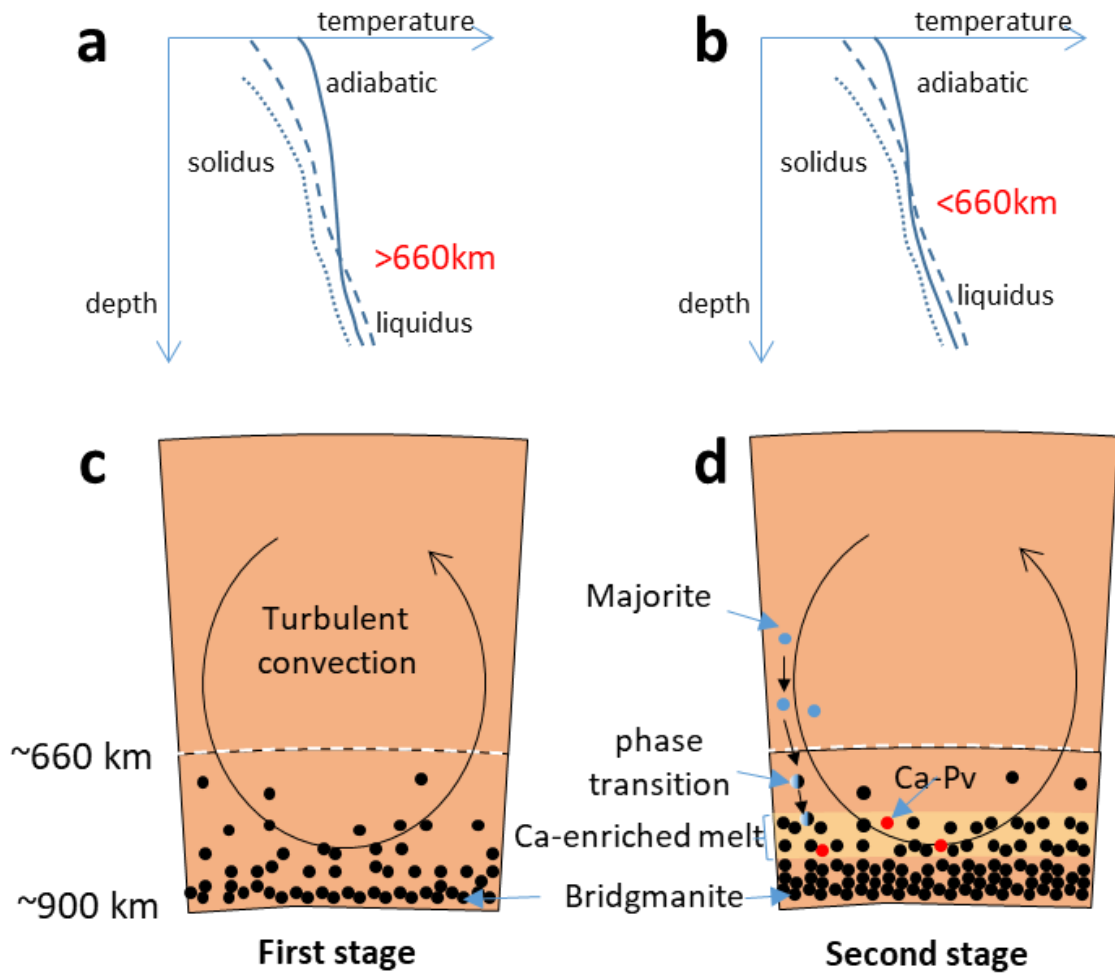


Figure 3.4 Crystal fractionation model of MO. **a, b:** Schematic drawings of solidus, liquidus and adiabats at the first and second stage of MO solidification, respectively. **c, d:** Schematic drawings of fractional crystal species at the first and second stage of MO solidification, respectively. **First stage:** Only bridgmanite accumulated on the bottom of MO. **Second stage:** Ca-Pv and bridgmanite accumulated simultaneously in the Ca-enrich melt layer just above the bottom of MO.

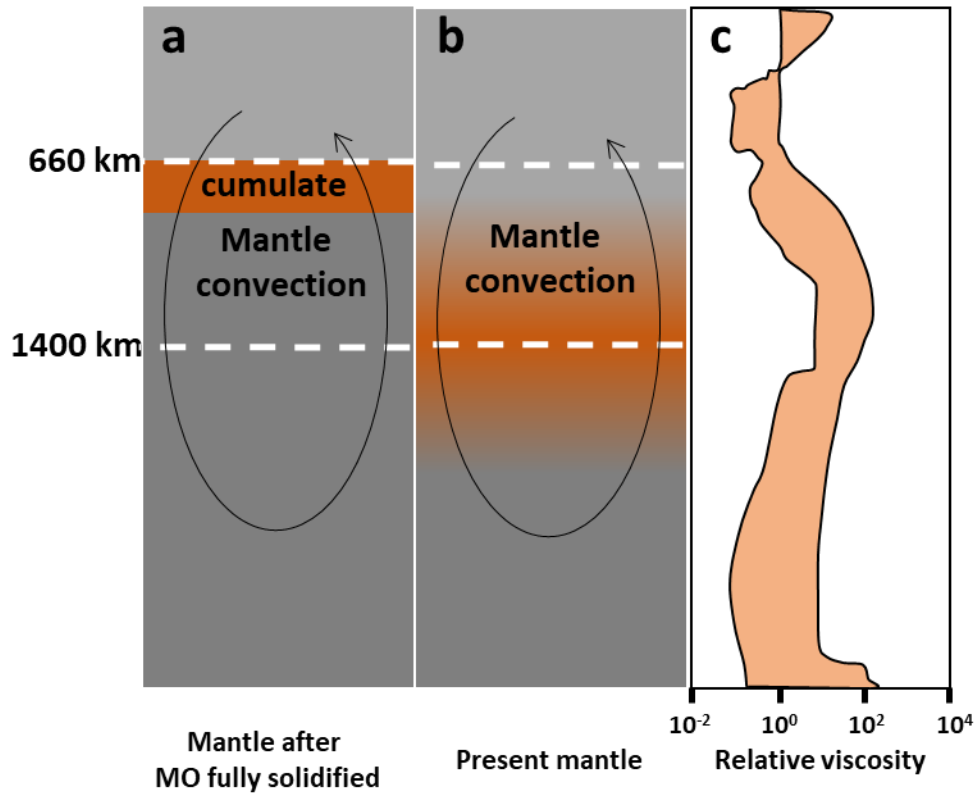
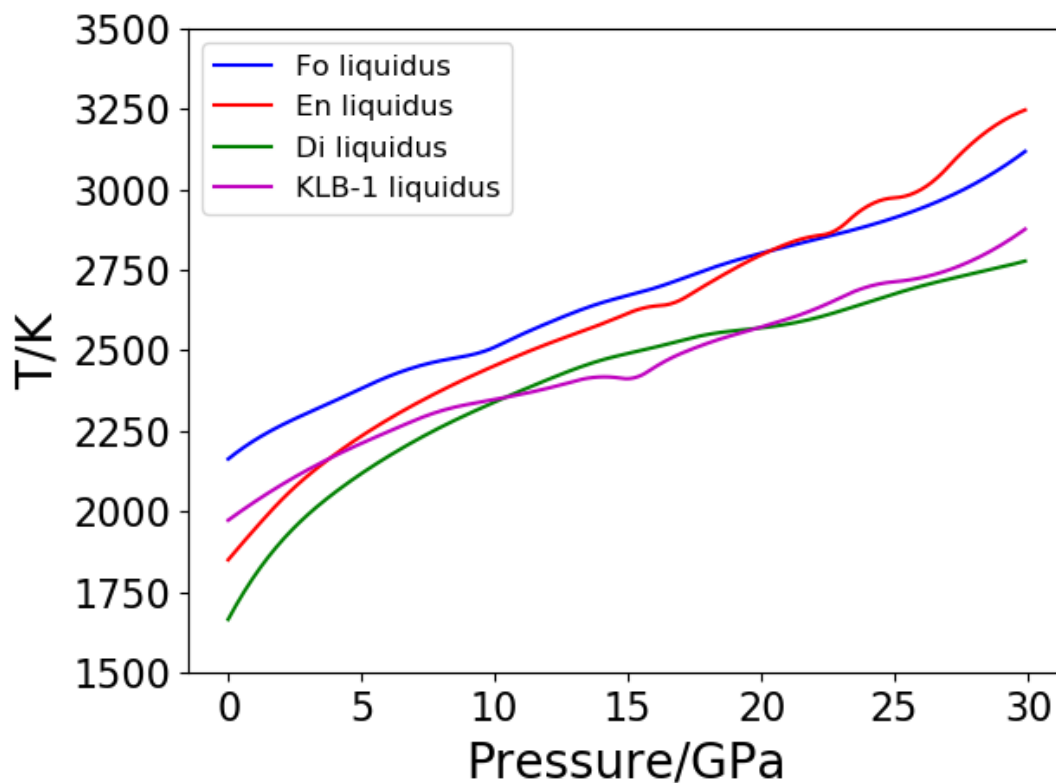


Figure 3.5 Possible fate of cumulate fate. a, Cumulate after MO fully solidified. **b,** Cumulate in present mantle. **d,** Viscosity structure of present mantle, modified from ref. 64.

Appendix 3.1 Liquidus of related mantle materials



Appendix figure 1. Liquidus of Fo, En, Di and KLB-1 compositions up to 30 GPa.

Liquidus temperatures of Fo and En composition are referred to Ref. 38 and reference therein (in part 2); that of Di to Ref. 39 and Ref. 40 (in part 2) below and above 17 GPa, respectively; that of KLB-1 to Ref. 45 (in part 3).

Acknowledgements

First of all, I would like to express my grateful appreciation to my supervisor A. Yoneda for his supervision, guidance, patience and continuous support during my Ph.D. course. I also would like to express my deep gratitude to E. Ito for his guidance, patience and support.

I highly appreciate D. Andrault, D. Yamazaki, and T. Yoshino for their helpful comments and guidance for research. I am also grateful to C. Wang and his wife S. Yan for their support, valuable comments and guidance during my study. I would like to express my thanks to W. Sun, H. Fei, B. Zhang, X. Guo, S. Zhai, N. Tsujino and C. Oka for their tutoring of experiments and apparatus; to G. Manthilake, H. Gomi, E. Boulard, C. Zhao, Y. Zhang, C. Liu, M. Sakurai, V. Jaseem, R. Guan and R. Wang for their assistance in high pressure high temperature experiments. I appreciate F. Noritake, S. Ohmura, T. Tsuchiya, M. Kanzaki, A. Suzuki, X. Xue, S. Yamashita, Y. Wang, D. Dobson for the discussions on the viscosity of silicate melt; and S. Tateno, H. Ozawa, H. Taniguchi (NIMS), Y. Takano (NIMS), R. Matsumoto (NIMS) on BDD.

Then, I would like to express my thanks to T. Irifune, and T. Sinmei for using the NPD mortar to grind BDD powder at the Geodynamic Research Center, Ehime University under the PRIUS program (Project Nos. A48, 2016-A02, 2017-A01, 2017-A21 and 2018-B30). Thank Y. Higo, Y. Tange, N. Guinot, A. King, M. Sheel for the technical support at synchrotron facilities (SPring-8, Japan and SOLEIL, France).

I would like to express my thanks to my friends N. Tai and P. Nara for their support and kindness. My special thanks to M. Uyama, M. Tani, M. Muraoka, R. Makihara, M. Kanemoto, all the other colleagues and staffs of IPM for their assistance and support to provide me with a suitable and comfortable environment for research.

Finally, I want to thank my family for their continuous encouragement and supports

throughout my studies and my girlfriend, F. Xu, not only for her assistance in my research but also for her love, support and encouragement during my study.

This work was supported by JSPS Research Fellowship for Young Scientists (DC2-JP17J10966 to L. Xie) and Grants-in-Aid for Scientific Research (Nos. 22224008 and 15H02128 to A.Yoneda). The in-situ X-ray experiments were performed under SPring-8 Budding Researcher Support Program (Nos. 2015A1771, 2016A1651, 2016B1686, 2017B1686 and 2018A1637) and SOLEIL research proposals (20160333, 20170194).